Title
Quantitative Analysis of Graphite Interphasial Species and Implications for Fast Charging

Author
McShane, Eric Joseph

Publication Date
2021

Peer reviewed|Thesis/dissertation

Quantitative Analysis of Graphite Interphasial Species and Implications for Fast Charging

by

Eric J. McShane

A dissertation submitted in partial satisfaction of the

requirements for the degree of

Doctor of Philosophy

in

Chemical Engineering

in the

Graduate Division

of the

University of California, Berkeley

Committee in charge:

Professor Bryan D. McCloskey, Chair
Professor Nitash Balsara
Professor Kristin Persson

Fall 2021

. Quantitative Analysis of Graphite Interphasial Species
and Implications for Fast Charging
Eric J. McShane

Abstract

Quantitative Analysis of Graphite Interphasial Species
and Implications for Fast Charging

by

Eric J. McShane

Doctor of Philosophy in Chemical Engineering

University of California, Berkeley

Professor Bryan D. McCloskey, Chair

Fast charging of lithium-ion batteries (LIBs) is affected by the electrolyte in many ways. The rate at which Li^+ can shuttle between the electrodes is determined by bulk electrolyte transport properties, such as the ionic conductivity and cation transference number (t_+), which influence the Li^+ concentration gradients that form in the cell and determine the attainable energy density at a given charge rate. The electrolyte also must form a stable electron-insulating, Li^+-conducting interface on both the anode and cathode in order to prevent continual degradation of the salt and solvent. The interfacial layer on the anode, the so-called 'SEI,' also fundamentally affects fast charging, as Li^+ must transport through the SEI layer, strip from its solvation shell, and ultimately insert into graphite. The influence of both of these aspects - bulk electrolyte transport properties and SEI formation - on fast charge capability are the focus of my dissertation.

The standard 'Gen 2' electrolyte employed in conventional batteries (1.2 M $LiPF_6$ in 3:7w ethylene carbonate:ethyl methyl carbonate (EC:EMC)) has an ionic conductivity of 10 mS/cm and a cation transference number (t_+, defined as the cation diffusivity divided by the sum of the cation and anion diffusivity) of ~0.4, meaning the strongly solvated Li^+ actually diffuses slower in solution than the bulky PF_6^- anion. This relatively low t_+ results in large concentration gradients during fast charge, which can lead to high required overpotentials and can result in Li plating on the graphite. As will be discussed in Chapter 2, if t_+ of the electrolyte can be engineered to be modestly higher, even with a substantial reduction in conductivity, charge performance can be improved. Chapter 2 also presents useful targets for electrolyte transport properties and outlines the benefit of high t_+ electrolytes in preventing Li plating, a hazardous side reaction that is exacerbated by fast charging.

The reason Gen 2 electrolyte is so commonly used, though, is not necessarily due to its transport properties, but rather due to the EC solvent's ability to form a stable SEI on graphite and allow Li^+ to strip its solvation shell before inserting into graphite. This dissertation outlines a titration procedure (called mass spectrometry titration, or MST) with which we quantify the amount of the solid carbonates that deposit on graphite as a result of EC reduction during SEI formation. The titration is also extended to quantify plated

Li that deposits on the graphite as well as other SEI components, such as Li_2C_2, and the contributions of the various irreversibly formed species to the observed capacity fade during fast charge are determined.

Finally, differential electrochemical mass spectrometry (DEMS) is used to measure gases that are evolved during battery cycling, and these gases provide quantitative insights into the amount of SEI species deposited on graphite. The DEMS technique is especially powerful when combined with MST, which provides complementary ex situ information about the extent of conversion of initially deposited SEI to other species. The holistic picture of the SEI provided by DEMS and MST is then used to determine the influence of the SEI on fast charge performance for various electrolyte compositions. In all, this dissertation quantitatively probes submicron-scale phenomena, including Li plating and SEI formation, to better understand the challenge of fast charging.

Acknowledgements

I'd first like to thank my partner Jingyi, who provided unconditional support throughout my time in graduate school, and my parents, who instilled in me a love for science from a young age. I'd next like to thank my housemates during my time in graduate school - Mike, David, Ari, Darwin, and Austin - with whom I shared many great times during the past five years. I'd also like to thank labmates and friends made along the way, including Ever, Kristian, Colin, Sara, Jessica, Kyle, Pete, Joe, Elizabeth, Sarah, David, Elyse, Lori, Kara, Helen, Zach, Matt, Yang, Byungchun, and Donghun. It wouldn't have been possible to do this work alone. I'd next like to thank the members of my qualifying exam committee (Nitash Balsara, Kristin Persson, and Alex Bell) for the enlightening discussions over the years. Nitash has been particularly supportive and engaged in the many meetings we've shared as part of the XCEL program. Finally, I'd like to thank my many mentors: Ben Richards and Tobias Hanrath, my mentor and PI at Cornell, who gave me an opportunity to gain hands-on lab experience as an undergraduate that was invaluable during graduate school, and Bryan, who allowed me to make mistakes and was invested in my growth as a scientist from day one.

This work was supported by the Assistant Secretary for Energy Efficiency and Renewable Energy, Vehicle Technologies Office, of the U.S. Department of Energy under Contract No. DEAC02-05CH11231, under the Advanced Battery Materials Research (BMR) Program. Work included in this dissertation was authored in part by the National Renewable Energy Laboratory, operated by Alliance for Sustainable Energy, LLC, for the U.S. Department of Energy (DOE) under Contract No. DE-AC36-08GO28308. Funding was provided by the U.S. DOE Office of Vehicle Technology Applied Battery Research and Extreme Fast Charge Program (XCEL). David E. Brown, co-author of work contained in this dissertation, and I gratefully acknowledge support from the National Science Foundation Graduate Research Fellowship Program (NSFGRFP) under Grant DGE-1106400. Helen K. Bergstrom, another co-author of work contained herein, acknowledges support from the NSFGRFP under Grant DGE-1752814. I also acknowledge the CAMP facility at Argonne National Laboratory for providing the graphite electrodes used in many of the studies in this dissertation. I finally thank Dr. Hasan Celik, Dr. Alicia Lund, and UC Berkeley's NMR facility in the College of Chemistry (CoC-NMR) for spectroscopic assistance. NMR instruments used for studies in this dissertation are supported in part by NIH-S10OD024998.

Contents

List of Figures

List of Tables

Chapter 1

Introduction to Fast Charging of Lithium-Ion Batteries

1.1 The Lithium-Ion Battery

Since their advent in the 1970s, lithium-ion batteries (LIBs) have become an integral part of our lives, spanning ubiquitous use cases such as phones and laptops to emerging markets such as electric vehicles. The LIB is typically comprised of three main components, a porous graphite anode, a porous polymer separator, and a porous transition metal oxide cathode, all fully wetted with an electrolyte solution (the most standard electrolyte being 1.2 M $LiPF_6$ in 3:7w ethylene carbonate (EC) to ethyl methyl carbonate (EMC), also called 'Gen 2 electrolyte'). Figure 1.1 shows a generalized schematic of a LIB.

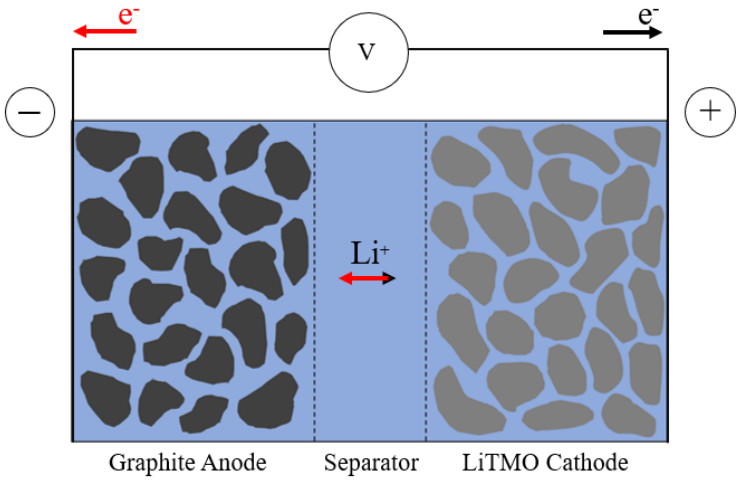

Figure 1.1: Lithium-ion battery schematic. Black arrows show the direction of transport of Li^+ in the electrolyte solution and electrons in the external circuit during discharge, and red arrows show the same during charge. LiTMO stands for lithium transition metal oxide.

The cell is initially assembled in the discharged state, meaning the cathode is fully lithiated and the graphite anode is fully delithiated. During the discharge process, which produces useful energy from the cell, the graphite is delithiated and the transition metal oxide cathode is lithiated, and electrons flow in the external circuit from anode to cathode. During the charging process, which is the primary focus of my dissertation, the opposite occurs, with graphite being lithiated while the transition metal oxide is delithiated. The full set of half cell reactions and the overall reaction are shown in Reactions 1.1.1-1.1.3. However, these lithiation and delithiation processes occur over a vast range of potentials, from ~0 V versus Li/Li^+ to ~4.3 V versus Li/Li^+, and the electrolyte is not completely stable over this entire range of potentials. The reaction of electrolyte salt and solvent components at each electrode results in interfacial film deposition, which will be the subject of the next section.

$$xLi^+ + xe^- + C_6 \longleftrightarrow Li_xC_6 \quad (0 - 0.5 \text{ V vs } Li/Li^+) \tag{1.1.1}$$

$$LiTMO \longleftrightarrow Li_{1-x}TMO + xLi^+ + xe^- \quad (3 - 4.3 \text{ V vs } Li/Li^+) \tag{1.1.2}$$

$$C_6 + LiTMO \longleftrightarrow Li_xC_6 + Li_{1-x}TMO \tag{1.1.3}$$

1.2 The Solid-Electrolyte Interphase

The standard Gen 2 electrolyte employed in LIBs (1.2 M $LiPF_6$ in 3:7w EC:EMC) affords both beneficial electrolyte transport properties (i.e., ionic conductivity, diffusivity, and Li^+ transference number, which will be the subject of Chapter 2) as well as interfacial stability at both the anode and cathode. The interfacial film formed on the anode as a result of the reduction of electrolyte salt and solvent species is termed the solid-electrolyte interphase (SEI), and the corresponding film on the cathode is termed the cathode-electrolyte interphase (CEI). The focus of my dissertation is the SEI rather than the CEI, as the SEI enables the remarkable capacity retention of LIBs over the course of many cycles, and the SEI composition and thickness are crucial considerations for fast charge capability.[1;2] Importantly, well-engineered SEIs serve as protective barriers for the liquid electrolyte against the highly reductive operating potentials of a graphite anode, yet still exhibit sufficient Li^+ transport to allow reasonable discharge and charge rates.

Despite its importance, the SEI remains poorly understood. The SEI composition has been primarily characterized qualitatively (e.g., with X-ray photoelectron spectroscopy),[3] and ex situ imaging studies have been completed, but can be significantly impacted by sample preparation (e.g., ensuring the SEI remains intact will removing remnant electrolyte and completely avoiding air exposure).[4] In my dissertation, I aim to provide a quantitative rigor to the study of the graphite SEI through the development and use of operando differential

electrochemical mass spectrometry (DEMS) and ex situ mass spectrometry titration (MST) measurements, which will be discussed in Chapters 3 and 4.

The SEI is generally considered to have two main layers: an inner-SEI which is rich in LiF (see Reaction 1.2.3) and is derived from $LiPF_6$ degradation products (such as HF, a product of $LiPF_6$ hydrolysis as shown in Reactions 1.2.1 and 1.2.2) and an outer-SEI, which is rich in alkyl carbonates (specifically lithium ethylene dicarbonate, or LiEDC) and is derived primarily from EC reduction products (see Reaction 1.2.4).[5] The formation of the SEI upon formation cycling, or the initial cycling of the LIB after its assembly, is shown in Figure 1.2.

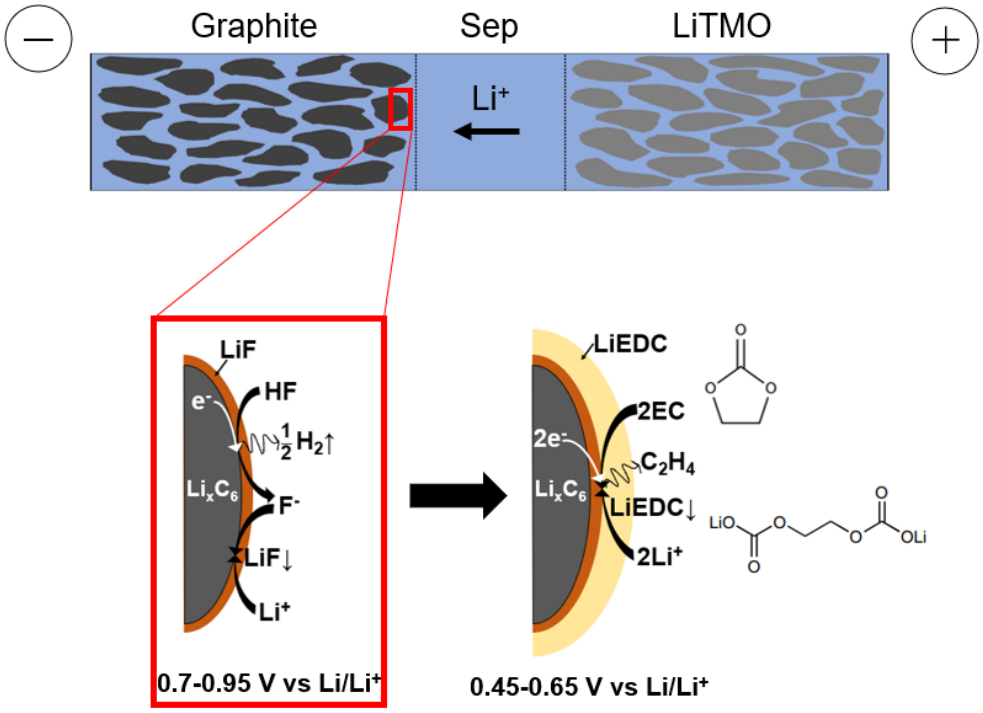

Figure 1.2: SEI formation schematic. LiF is deposited first via Reaction 1.2.3, which occurs in the range of ~0.70-0.95 V versus Li/Li^+. LiEDC is then deposited via Reaction 1.2.4, which occurs in the range of ~0.45-0.65 V versus Li/Li^+.

The inevitable presence of water in LIB electrolytes slowly converts $LiPF_6$ to HF as shown in Reactions 1.2.1 and 1.2.2, allowing the LiF-forming Reaction 1.2.3 to occur. However, some other reactions can form additional inner-SEI components. For example, H_2O can be directly reduced to form LiOH, which can be reduced again to form Li_2O, as will be discussed in Chapter 4. The outer-SEI is also a bit more complicated than shown in Figure 1.2. Once LiEDC is deposited, it can undergo a number of side reactions that result in a vast array of species that ultimately comprise the graphite SEI.[1] This will also be discussed in depth in Chapter 4.

$$LiPF_6 \longrightarrow LiF + PF_5 \tag{1.2.1}$$

$$PF_5 + H_2O \longrightarrow POF_3 + 2\,HF \tag{1.2.2}$$

$$2\,Li^+ + 2\,HF + 2\,e^- \longrightarrow 2\,LiF + H_2 \tag{1.2.3}$$

$$2\,Li^+ + 2\,(CH_2O)_2CO\ (EC) + 2\,e^- \longrightarrow (CH_2OCO_2Li)_2\ (LiEDC) + C_2H_4 \tag{1.2.4}$$

The SEI layer fundamentally affects battery operation, as an SEI layer that does not fully passivate against solvent reduction will result in continual capacity fade and consumption of electrolyte. In addition, the SEI layer porosity, thickness, and composition determine the rate at which Li^+ can transport through the layer to ultimately lithiate the graphite material. Thus, quantifying SEI components is a key step toward understanding the limitations of fast charge and developing ways to mitigate the associated challenges.

1.3 Challenges Associated with Fast Charging

1.3.1 Li^+ Concentration Gradients

In addition to the SEI, electrolyte transport properties also play a crucial role in enabling fast charging of LIBs. The high currents required during fast charge result in large Li^+ concentration gradients within the electrolyte phase (as shown in Figure 1.3), and these Li^+ concentration gradients result in regions of overutilization of graphite active material near the graphite-separator interface (due to the consistently high electrolyte Li^+ concentration in this region), coupled with underutilization of graphite active material near the graphite-current collector interface (due to the low electrolyte Li^+ concentration in this region during fast charge).[6] This heterogeneous distribution of graphite lithiation states (or states of charge, abbreviated SOCs) throughout the depth of the graphite electrode in turn has a deleterious effect on attainable cell gravimetric energy density.

Two of the main electrolyte transport properties which determine the extent of Li^+ gradients that arise during fast charge are the ionic conductivity (σ) and the Li^+ transference number (t_+), which once again is defined as the cation diffusivity divided by the sum of the cation and anion diffusivity. For a standard binary salt electrolyte, such as Gen 2 electrolyte, $t_+ \approx 0.4$ and $\sigma \approx 10$ mS/cm. As will be shown in Chapter 2, an electrolyte with a modest increase in t_+ (to ~0.7) can improve the attainable energy density of LIBS even at significantly reduced conductivity compared to the standard electrolyte. However, there is an inherent tradeoff between σ and t_+ among most electrolyte compositions, as efforts to immobilize the anion to improve t_+ often come at the cost of reduced σ. We therefore use continuum-scale modeling

in Chapter 2 to uncover the required σ and t_+ to break even with and even surpass the charge performance offered by a standard electrolyte. We additionally find that, beyond improved attainable energy density, high transference number electrolytes (HTNEs) also impart more uniform lithiation of the graphite electrode during fast charge and delay the onset of Li plating, a detrimental side reaction which will be discussed in the next section.

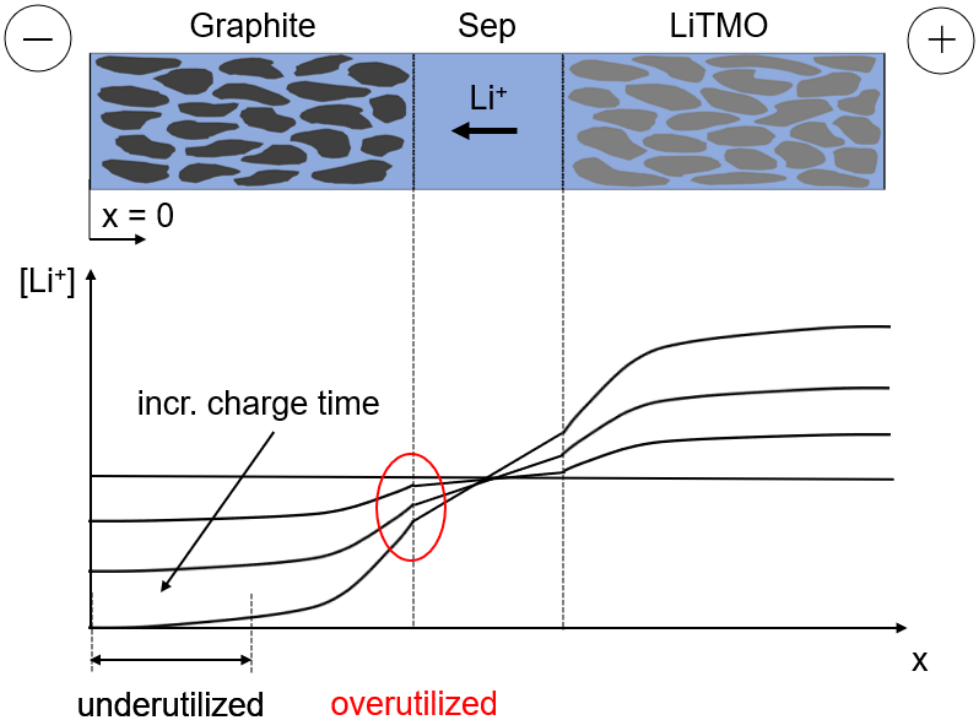

Figure 1.3: Electrolyte Li^+ concentration gradients during fast charge. Large electrolyte Li^+ gradients form during fast charge in order to supply the high necessary current. These Li^+ gradients result in overutilization of the graphite active material near the graphite-separator interface (marked in red) and underutilization of the graphite active material near the current collector.

1.3.2 Lithium Plating

Lithium plating is a side reaction that occurs in LIBs whereby Li^+ is reduced directly on the surface of graphite instead of inserting between graphitic layers. Graphite particles near the separator which are at high SOC are especially susceptible to Li plating, as the standard potential of graphite at high SOCs is only about ~50 mV versus Li/Li^+, meaning an overpotential of 50 mV or more in magnitude can drive the electrode into a regime where Li plating becomes thermodynamically favorable. Once plated, Li can undergo a number of processes (as outlined in Figure 1.4):

1. It can be reversibly stripped from the graphite surface upon deintercalation.
2. It can chemically insert into graphite.[7;8]

3. It can become electronically isolated from the graphite, resulting in 'dead Li,' or plated Li metal which is no longer electrochemicly active.[2]

4. It can react with other SEI components or with electrolyte to form additional SEI species, which are referred to as 'inactive Li.'[2]

While processes 1 and 2 are reversible, processes 3 and 4 are irreversible and directly lead to capacity fade during fast charge cycling. However, the extent to which each genre of species (both dead and inactive Li) contributes to capacity fade is unclear, as plated Li and SEI species are notoriously difficult to quantify. The presence of plated Li is often detected binarily using in situ electrochemical or spectroscopic methods,[9] and the SEI is typically characterized qualitatively using ex situ methods such as X-ray photoelectron spectroscopy.[3] To provide a more quantitative approach to study degradation during fast charge, we developed a mass spectrometry titration (MST) technique with which we quantified both dead Li and specific SEI species. Using MST, we found that dead Li metal accounts for the majority of the capacity loss during initial fast charge cycling, but inactive Li (specifically additional deposited solid carbonates) resulting from the reaction of plated Li with electrolyte and other SEI species also contributes substantially to capacity loss after prolonged cycling (see Chapter 3).[2] We also used differential electrochemical mass spectrometry (DEMS) in combination with MST to quantitatively probe initial SEI formation, and we correlated the initially-formed SEI composition under electrolytes of 0.35 M, 0.70 M, 1.2 M, and 2.0 M $LiPF_6$ concentration to subsequent fast charge performance, revealing that the SEI composition plays a critical role in enabling rapid charging (as discussed in Chapter 4).

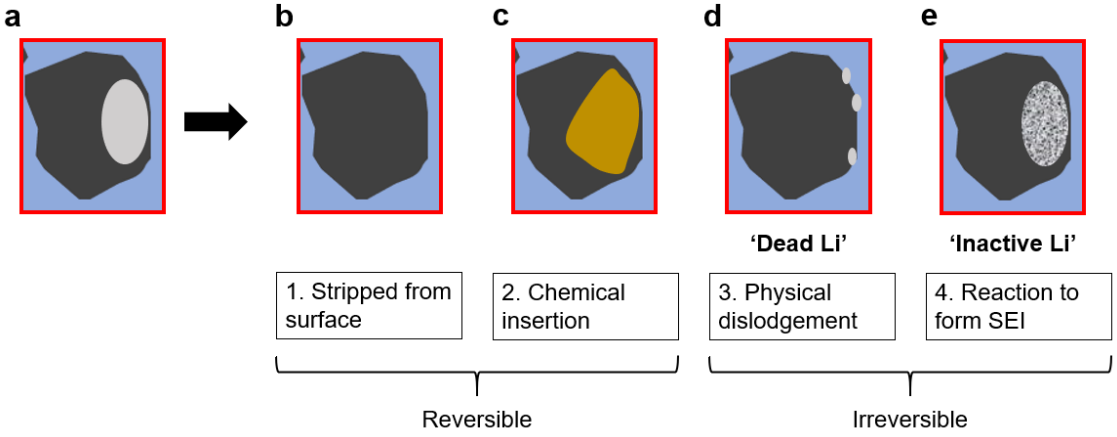

Figure 1.4: The four fates of plated Li. **a.** Illustration of a graphite particle with an oval of plated Li on its surface. Once plated, Li can **b.** be reversibly stripped from the graphite surface, **c.** chemically insert into graphite (lithiated graphite is shown as an off-gold color, which is the true color of fully lithiated graphite), **d.** form dead Li, or **e** react to form additional SEI species, known as inactive Li.

Chapter 2

Continuum Scale Modeling to Understand the Influence of Electrolyte Transport Properties on Li-ion Battery Fast Charging

2.1 Abstract

In this chapter, we highlight an often less noted route to improving the energy density and fast charge capability of full cell Li-ion batteries (LIBs): increasing the Li^+ transference number (t_+) of the electrolyte, which is defined for binary salt electrolytes as the diffusivity of the cation divided by the sum of the diffusivity of the cation and anion. The standard Gen 2 electrolyte has a conductivity of ~10 mS/cm and a t_+ of ~0.4, meaning the anion diffusivity is actually larger than that of the Li^+, owing to the large solvation shell of Li^+ in solution. Turning to Newman's original LIB models, we demonstrate that electrolytes with modestly higher Li^+ transference numbers compared to traditional carbonate-based liquid electrolytes would enable faster charging (e.g., >2C), even if their conductivity was substantially lower than that of conventional electrolytes. The model also reveals that high transference number electrolytes (HTNEs) significantly delay the expected onset of Li plating due to the elimination of the steep Li^+ concentration gradients which typically plague standard electrolyte formulations.[i]

2.2 Promising Routes to a Higher Transference Number

Designing an electrolyte in which the Li^+ transference number (t_+) approaches 1 has been the subject of much interest since at least 1985, with a few main research thrusts.[10] Figure 2.1 presents several representative sketches of different classes of HTNEs. Lithium-conducting

[i]This chapter is largely adapted from previously published work in: K.M. Diederichsen, E.J. McShane, and B.D. McCloskey. *ACS Energy Letters.* **2017**, *2*, 2563-2575.

ceramics may be formulated that effectively create a single-ion conductor (SIC, see Figure 2.1a).[11] Dry, nonswollen polymer electrolytes, long studied as a potential solid-state electrolyte material for use with the lithium metal anode, have been synthesized with anions appended to the polymer backbone (Figure 2.1b).[12] As a means to improve the performance of neat polymer systems, polymer electrolyte membranes with additives ranging from small-molecule solvents to nanoparticles have been studied extensively (Figure 2.1c).[13] In addition, nonaqueous solvent-filled ionomers (hard polymer membranes affixed with ions) have been studied for battery applications (Figure 2.1d).[14] Alternative methods to raise the transference number of a liquid electrolyte through the use of polymeric anions (nonaqueous polyelectrolyte solutions, shown in Figure 2.1e)[14] and highly concentrated electrolytes (so-called "solvent-in-salt" electrolytes)[15] have also been suggested.

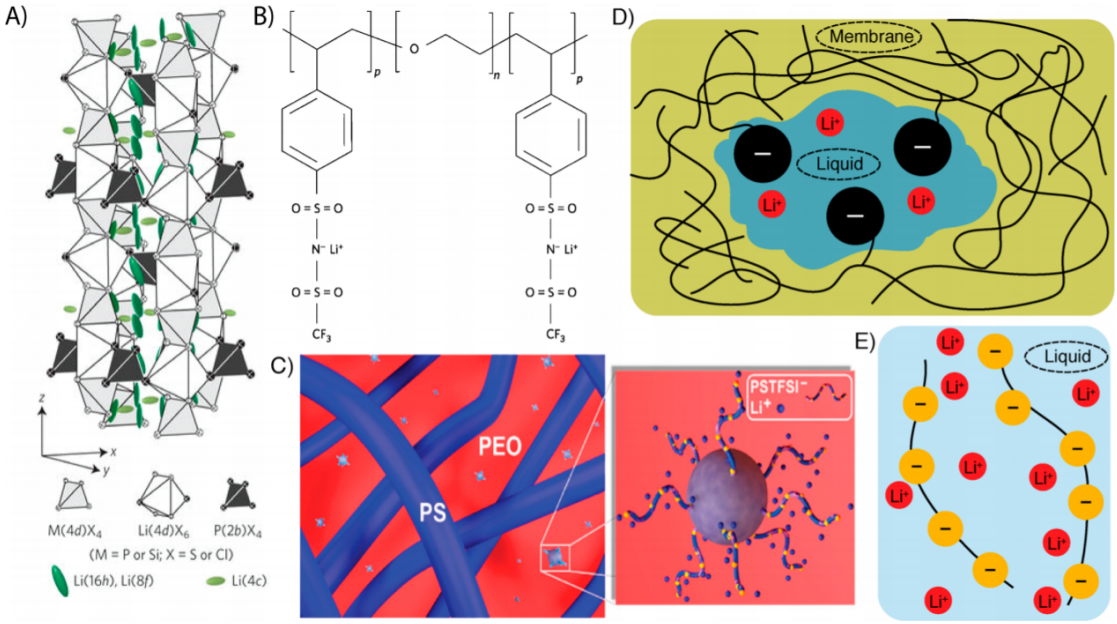

Figure 2.1: Several classes of HTNEs. **a.** Ceramic SIC based on doped lithium thiophosphate glass, reproduced from ref [11]. **b.** Neat polymer electrolyte poly(styrene trifluoromethanesulphonylimide-co-poly(ethylene oxide)), reproduced from ref [12]. **c.** Mixed polymer electrolyte system based on a nanoparticle/copolymer blend, reproduced from ref [13]. **d.** Sketch of a solvent-filled ionomer membrane, reproduced from ref [6]. **e.** Sketch of a polyelectrolyte HTNE solution, reproduced from ref [6].

However, all of these electrolyte compositions come with associated challenges. Ceramic materials, for example, suffer from high interfacial impedance between the ceramic electrolyte and the electrode material with which it is in contact.[16] Polymer and high concentration electrolytes typically have at least an order of magnitude reduced conductivity compared to the standard carbonate-based liquid electrolyte.[12;13;15] Polyelectrolyte solutions may offer a reasonable middle ground, with slightly reduced conductivity (~1 mS/cm) and slightly improved t_+ (~0.7) compared to the standard liquid electrolyte.[14] It is thus important to understand the tradeoff between conductivity and transference number in modeled LIB systems as next-generation HTNE formulations are developed. Doyle, Fuller, and Newman in

1994 demonstrated the importance of the lithium ion transference number (t_+), showing that a t_+ of 1 offers significant enhancement in terms of materials utilization, power, and energy density over a $t_+ \approx 0.2$, particularly at high rates of discharge and even with an order of magnitude decrease in conductivity.[17] It is shown in Section 2.2 that even modest improvements in t_+, e.g., to $t_+ \approx 0.7$, would be beneficial, particularly allowing a higher attainable state of charge (SOC) at high charge rates, where a large, constant current would be necessary to quickly charge the battery.

2.3 Model Formulation

To understand useful targets for t_+ and σ to enable fast charging, we turn to finite element methods based on Newman's 1D isothermal battery model. Using the Batteries and Fuel Cells Module in COMSOL Multiphysics 5.2a, we model charging of a dual lithium ion insertion cell consisting of a porous graphite anode, a porous $LiCoO_2$ cathode, and an electrolyte of varying transport properties, with a simple schematic of the cell shown in Figure 2.2. We study charge instead of discharge because electric vehicle (EV) batteries are discharged at high rates only intermittently (during acceleration), such that the salt concentration gradients that ultimately limit cell performance do not evolve to the extremes that would be expected during high rate charging. The goal of modeling this cell configuration is to compare high t_+ electrolytes (where both t_+ and σ are varied) to a standard binary salt liquid electrolyte, for which t_+ is 0.4 and σ is 10 mS/cm, where all other battery properties (including SEI stability and impedance) are similar. Relevant governing equations and base case parameters are given in subsequent sections.

2.3.1 Geometry

We implemented a 1-D model to simulate the galvanostatic charge of the Li_xC_6/Li_yCoO_2 cell shown in Figure 2.2 using COMSOL Multiphysics 5.2a. We defined the $LiCoO_2$ cathode length to be 100 µm and determined the graphite anode length according to the expression below,

$$\frac{C_{s,neg}^{max}\epsilon_{\mathrm{s,neg}}L_{\mathrm{neg}}\Delta x}{C_{s,pos}^{max}\epsilon_{\mathrm{s,pos}}L_{\mathrm{pos}}\Delta y} = 1.2 \tag{2.3.1}$$

where $C_{s,j}^{max}$ is the maximum theoretical solid phase lithium concentration in electrode material j, $\epsilon_{s,j}$ is the active material volume fraction of electrode j, and L_j is the length of electrode j. We assumed the anode, Li_xC_6, operates with a lithium stoichiometric coefficient between 0 and 0.99 (Δx=0.99), and the cathode, Li_yCoO_2, operates with a lithium stoichiometric coefficient between 0.50 and 1.00 (Δy=0.50). By implementing 20% excess anode material and setting a cutoff potential of 4.2 V, we avoided the onset of lithium deposition due to overcharging.

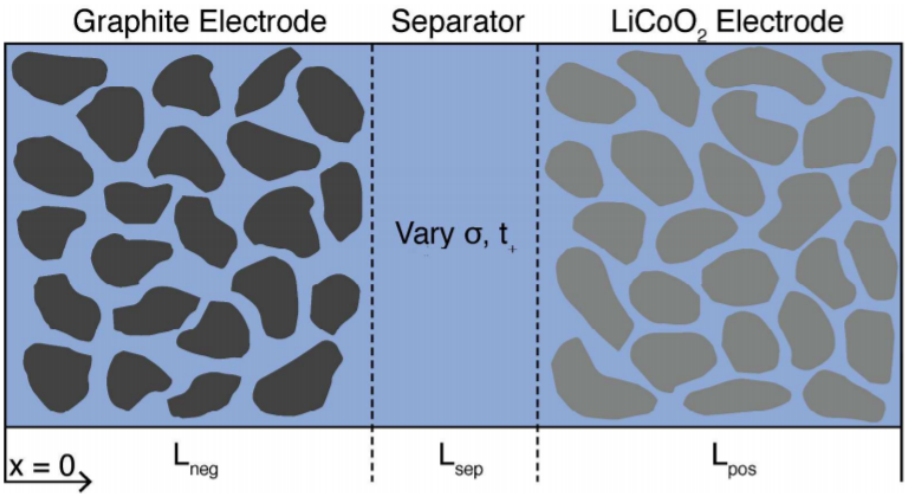

Figure 2.2: Lithium-ion battery schematic, with some relevant parameters for the Newman-type model shown.

2.3.2 Separator Region

As is typically done when modeling transport through porous media, we adjusted the electrolyte diffusivity (D_l) and conductivity (σ_l) to an effective electrolyte diffusivity ($D_{l,eff}$) and conductivity ($\sigma_{l,eff}$) according to the Bruggeman correction,

$$D_{l,eff} = \epsilon_l^{1.5} D_l \tag{2.3.2}$$

$$\sigma_{l,eff} = \epsilon_l^{1.5} \sigma_l \tag{2.3.3}$$

where ϵ_l is liquid phase volume fraction.

Ion transport in the separator was modeled using transport equations derived from Newman's work[18] contained in the Batteries and Fuel Cells Module of COMSOL. Beginning with concentrated solution theory, we can express the velocity of each component (v_i) in terms of the electrochemical potential gradient ($\nabla \mu_i$) and concentration (c_i) of each component,

$$c_i \nabla \mu_i = \sum_{i \neq j} K_{ij}(v_j - v_i) \tag{2.3.4}$$

where K_{ij} is the frictional coefficient describing interactions between components i and j. Assuming a binary electrolyte and a solvent species with no net velocity, we can invert the

above equation to arrive at an expression for the molar flux of the salt species in the liquid phase (N_l),

$$N_l = -D_{l,eff}\nabla c_l + \frac{i_l t_+}{F} \tag{2.3.5}$$

where $D_{l,eff}$ is the effective diffusion coefficient of the salt, c_l is the concentration of the salt in the liquid phase, i_l is the liquid phase current density, F is Faraday's constant, and t_+ is the cation transference number. We note that c_l is defined such that the cation and anion concentrations are equal due to electroneutrality. If we let ν_+ and ν_- be the number of cations and anions, respectively, produced by the dissociation of one mole of the electrolyte salt, we can define c_l as such:

$$c_l = \frac{c_+}{\nu_+} = \frac{c_-}{\nu_-} \tag{2.3.6}$$

With an expression for the molar flux of the salt, the mass balance becomes

$$\epsilon_l \frac{\partial c_l}{\partial t} + \nabla \cdot N_l = R_l \tag{2.3.7}$$

where R_l is the cation source term, which only contributes in the porous electrode region. Finally, we employ an expression for the current density,[18] which may be used to solve for the electrical potential (ϕ_l),

$$i_l = -\sigma_l \nabla \phi_l + \frac{2\sigma_l RT}{F}(1 + \frac{\partial ln f}{\partial ln c_l})(1 - t_+)\nabla ln c_l \tag{2.3.8}$$

where σ_l is the electrolyte conductivity, R is the ideal gas constant, T is the temperature in Kelvin, and f is the mean salt activity coefficient.

2.3.3 Porous Electrodes

The salt flux and conservation equations for the porous electrode regions are analogous to those shown in the previous section. However, we must now additionally account for reactions which produce or consume lithium ions and the solid phase diffusion of lithium. We apply Butler-Volmer kinetics, manifested in the expression below for the local current density at the electrode-electrolyte interface (i_{loc}),

$$i_{loc} = i_0(exp(\frac{\alpha_a F\eta}{RT}) - exp(\frac{-\alpha_c F\eta}{RT})) \tag{2.3.9}$$

where i_0 is the exchange current density, α_i is the anodic or cathodic transfer coefficient, and η is the local overpotential. The exchange current density is defined generally for electrode j below,

$$i_0 = Fk_j(c_{s,j}^{max} - c_{s,j})^{\alpha_a}(c_{s,j})^{\alpha_c}(c_l)^{\alpha_a} \tag{2.3.10}$$

where k_j is the reaction rate constant and $c_{s,j}$ is the solid phase lithium concentration. Further, the local overpotential is defined as

$$\eta = \phi_s - \phi_l - E_{eq} \tag{2.3.11}$$

where ϕ_s and ϕ_l are the solid and liquid phase electrical potentials, respectively, and E_{eq} is the equilibrium potential for the electrode material at a given state of charge. Empirical data is used to define $\mathrm{E_{eq}}$ as a function of state of charge for both electrodes.[19;20]

We assume the electrode particles are spherical, and thus we are able to define the reaction source term (R_l),

$$R_l = \frac{3\nu_{Li_+} i_{loc}}{r_p F} \tag{2.3.12}$$

where r_p is the average electrode particle radius. The factor of $3/r_p$ is the specific area of the spherical particles, used to correct the units on the source term. Upon reacting at the particle surface, the lithium must subsequently diffuse through the solid particle. The material balance for this process is

$$\frac{\partial c_s}{\partial t} = \nabla \cdot (D_s \nabla c_s) \tag{2.3.13}$$

where c_s is the lithium concentration in the solid particle and D_s is the diffusion coefficient of lithium in the particle. This solid-state diffusion process is subject to the boundary conditions

$$\frac{\partial c_s}{\partial r}\Big|_{r=0} = 0 \tag{2.3.14}$$

and

$$-D_s \frac{\partial c_s}{\partial r}\Big|_{r=r_p} = \frac{\nu_{Li_+} i_{loc}}{F} \tag{2.3.15}$$

2.3.4 Initial and Boundary Conditions

We set the initial electrolyte concentration to 1 M. The initial electrode potentials were determined from the respective equilibrium potential functions according to the state of charge of each electrode, and the initial electrolyte potential was assumed to be equal to the initial anode potential. The system was assumed to be isothermal at 298 K.

No flux boundary conditions were imposed on the salt at the two ends of the cell, and a current density (i_{set}) was specified at the cathode/current collector interface to set the C-rate.

2.3.5 Assumptions

A few simplifying assumptions were necessary to enable a broad comparison of electrolytes of varying conductivity, transference number, and salt diffusion coefficient.

1. The binary salt liquid electrolyte was modeled with the following properties: σ=10mS/cm, t_+=0.40, D_l=3x10^{-6} cm^2/s. These properties are consistent with those reported for a 1 M $LiPF_6$ electrolyte in propylene carbonate/ethylene carbonate/dimethyl carbonate.[21]

2. A generalized activity coefficient concentration dependence was applied for all tested transport properties. The concentration dependence of the salt activity coefficient appears in the expression for current density. To incorporate this factor in our model, we used empirical activity coefficient data obtained for $LiPF_6$ in propylene carbonate/ethylene carbonate/dimethyl carbonate,[21] and we assumed that this activity coefficient data applied to all tested sets of σ, t_+, and D_l. In reality, this dependence will change if the solvent or salt are changed, but we assumed it was valid over all simulated transport properties for simplicity.

3. The parameters that were varied between simulations (σ, t_+, and D_l) were assumed to be independent of salt concentration. That is, the parameters did not vary across the length of the cell during a simulation.

4. The salt diffusion coefficient (D_l) was varied between simulations as t_+ was varied. To determine the salt diffusion coefficient for a given t_+, we used the expressions below,[17]

$$D_l = \frac{c_T}{c_0}(1 + \frac{\partial ln f}{\partial ln c})\frac{D_{0+}D_{0-}(z_+ - z_-)}{z_+D_{0+} - z_-D_{0-}} \tag{2.3.16}$$

$$t_+ = \frac{z_+D_{0+}}{z_+D_{0+} - z_-D_{0-}} \tag{2.3.17}$$

where c_T is the total solution concentration (including solvent, cation, and anion), c_0 is the concentration of solvent, f is the mean molar salt activity coefficient, D_{0+} and

D_{0-} are the diffusion coefficients of the cation (+) and anion (-) in the solvent (0), and z_+ and z_- are the charge numbers of the cation and anion, respectively. We set D_{0+} and D_{0-} to 2.5x10^{-6} cm^2/s and 3.75x10^{-6} cm^2/s, respectively, for the binary salt liquid electrolyte case in accordance with data from the literature.[21] We then held D_{0+} constant at 2.5x10^{-6} cm^2/s for all simulated t_+ and σ, such that new D_l and D_{0-} were calculated for each tested t_+. This method is consistent with altering t_+ by immobilizing the anion while keeping the Li^+ cation diffusion coefficient the same. We additionally assumed that the factor c_T/c_0 was equal to 1 for all simulations.

2.3.6 Model Parameters

Table 2.1: Base case model parameters.

Symbol	Value	Units	Reference
L_{pos}	100	µm	assumed
L_{sep}	25	µm	assumed
L_{neg}	91.8	µm	calculated
$\epsilon_{s,pos}$	0.62		assumed
$\epsilon_{l,pos}$	0.20		assumed
$\epsilon_{f,pos}$	0.18		assumed
$\epsilon_{s,neg}$	0.65		assumed
$\epsilon_{l,neg}$	0.25		assumed
$\epsilon_{f,neg}$	0.10		assumed
$\epsilon_{l,sep}$	0.39		assumed
$c^0_{s,pos}$	50051	mol/m^3	assumed
$c^{max}_{s,pos}$	50051	mol/m^3	assumed
$c^0_{s,neg}$	0	mol/m^3	assumed
$c^{max}_{s,nag}$	31507	mol/m^3	assumed
c^0_l	1	mol/L	assumed
$r_{p,pos}$	8	µm	assumed
$r_{p,neg}$	11	µm	assumed
$D_{s,pos}$	5x10^{-8}	cm^2/s	[22]
$D_{s,neg}$	3x10^{-8}	cm^2/s	[23]
$\sigma_{s,pos}$	0.1	S/m	[24]
$\sigma_{s,neg}$	100	S/m	[24]
k_{pos}	6.67x10^{-11}	mol$^{-1/2}$m$^{-3/2}$s^{-1}	[25]
k_{neg}	1x10^{-9}	mol$^{-1/2}$m$^{-3/2}$s^{-1}	[25;26] (intermediate value)
α_a	0.5		assumed
α_c	0.5		assumed
T	298	K	assumed
V_{cut}	4.2	V	assumed
D_{0+}	2.5x10^{-6}	cm^2/s	[21] (calculated)

Table 2.2: Modeling framework nomenclature.

Symbol	Meaning
L	length
ϵ	volume fraction, porosity
c	concentration
r	radius
D	diffusion coefficient
σ	conductivity
k	reaction rate constant
α	transfer coefficient
T	temperature
V	voltage

Table 2.3: Modeling framework subscripts.

Subscript	Meaning
pos	cathode
neg	anode
sep	separator
s	solid phase
l	liquid phase
f	filler (binder, carbon black)
p	particle
a	anodic
c	cathodic
cut	cutoff
0+, 0-	cation, anion with respect to solvent

Table 2.4: Modeling framework superscripts.

Superscript	Meaning
0	initial
max	maximum theoretical

2.4 Modeling Results

2.4.1 Attainable State of Charge with a High Transference Number Electrolyte

Given many studies that attempt to improve electrolyte t_+, one would expect an inherent trade-off between σ and t_+; therefore, we chose to study charge behavior of cells where t_+ of the electrolyte is varied between 0.4 and 1 and σ is varied between 1 and 10 mS/cm (i.e., higher t_+ and lower σ than traditional liquid electrolytes). The base case cell geometry is shown in Figure Figure 2.3a. Typical charge voltage profiles (with a voltage cutoff of 4.2 V) are shown in Figure 2.3b, and the total attainable SOC prior to reaching the cutoff voltage is shown as a function of charge rate for these cells in Figure 2.3c,d. Although little difference is observed in the attainable SOC at low current densities (<1C), the beneficial effects of high t_+ can be clearly observed at 2C rates and above, where we observe a precipitous increase in attainable SOC as t_+ is increased. Perhaps of most interest, we have determined the t_+ required at a given σ to achieve 75% SOC at 2C. We refer to this SOC as the 'breakeven' point, as it corresponds to the maximum attainable SOC for a standard liquid electrolyte (t_+=0.40, σ=10 mS/cm) when charged at 2C in our simulated cell configuration. These

results, in addition to the t_+ and σ needed for a 10% increase in attainable SOC compared to the standard liquid electrolyte case, are shown in Figure 2.3e. We observe that, for example, a t_+ of 0.80 allows for breakeven charge performance at 50% reduced conductivity compared to the standard liquid electrolyte. Clearly, the transference number has a dramatic effect on cell performance at EV battery-relevant rates. Additional benefits of HTNEs related to lithium plating, which can cause precipitous capacity fade during fast charge cycling, are discussed in the next section.

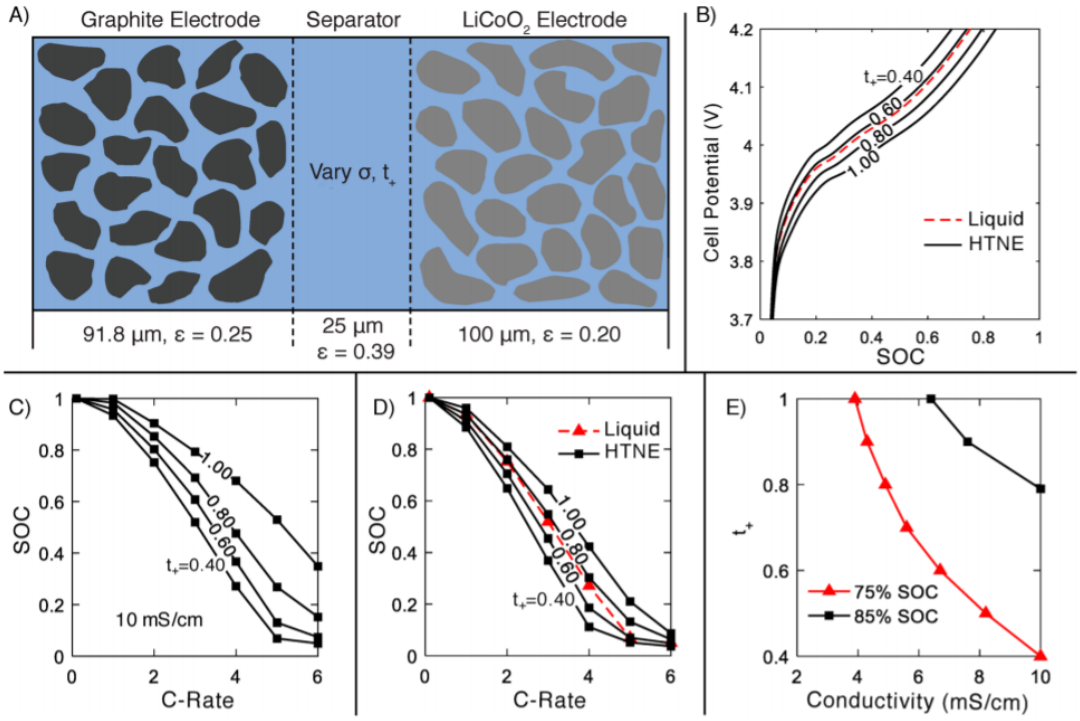

Figure 2.3: COMSOL modeling results for standard and HTNEs. **a.** Schematic of a modeled dual lithium ion insertion cell consisting of a graphite anode, $LiCoO_2$ cathode, and separator. Thicknesses and porosities (ϵ) are given for each cell component. **b.** Red dashed charge curve for standard binary salt liquid electrolyte (t_+=0.40, σ=10 mS/cm) and solid black charge curves for HTNE (t_+ varies, σ=6 mS/ cm) at 2C with a 4.2 V cutoff voltage. **c.** Attainable SOC versus charge rate for electrolyte with σ=10 mS/cm and variable t_+. **d.** Attainable SOC versus charge rate for standard liquid electrolyte (red dashed triangles) and HTNE (solid black squares). HTNE σ=5 mS/cm for this set of simulations. **e.** Minimum σ and t_+ values required to achieve 75% (red triangles) and 85% (black squares) SOC at 2C with a 4.2 V cutoff voltage. Our baseline binary salt liquid electrolyte (σ=10 mS/cm and t_+=0.4) achieved 75% SOC at 2C and a 4.2 V cutoff, as observed in panel b.

2.4.2 Lithium Plating with a High Transference Number Electrolyte

In the previous section, we applied a cutoff voltage of 4.2 V for all simulations, as we found that we could avoid lithium plating by doing so. If we raise the cutoff voltage to 4.3 V (see Figure 2.4a), we observe a considerable improvement in charge performance, but we run the

risk of plating lithium on the anode. We define the overpotential for the plating reaction according to Equation 2.4.1,

$$\eta_{\text{plating}} = \varphi_s - \varphi_l - E_{\text{plating}} \tag{2.4.1}$$

where η_{plating} is the overpotential for the lithium plating reaction, φ_s is the solid phase potential in the anode, φ_l is the electrolyte phase potential in the pores of the anode, and E_{plating} is the equilibrium potential for the plating reaction, which is taken to be 0 V vs Li/Li^+.[27] When η_{plating} is negative, the plating reaction is thermodynamically favorable. We found that, in order to avoid a negative η_{plating} with a 4.3 V cutoff voltage at 2C, a t_+ of 0.73 or above coupled with a σ of 10 mS/cm would be required, which is a considerably more stringent constraint on electrolyte transport properties than shown in Figure 2.4a to achieve 75% SOC. The Li plating reaction places an additional constraint on the system that must be considered.

In Figure 2.4b, we show a breakeven analysis which accounts for a 'safety window' constraint placed by lithium plating. The breakeven curves from Figure 2.3e are superimposed with two curves representing the t_+ and σ needed to ensure $\eta_{\text{plating}} \geq 10$ mV and $\eta_{\text{plating}} \geq 20$ mV at every point in the anode throughout the entire charge cycle at 2C with a 4.2 V cutoff voltage. Interestingly, low transference number electrolytes run a higher risk of lithium deposition, such that the low t_+, high σ cases in the original breakeven analysis become unviable if we require a 20 mV safety window to avoid lithium plating. However, the high transference number cases in the original breakeven analysis remain viable even after implementing the 20 mV safety window. It is clear that high t_+ electrolytes present an attractive option for suppressing lithium plating at high charge rates.

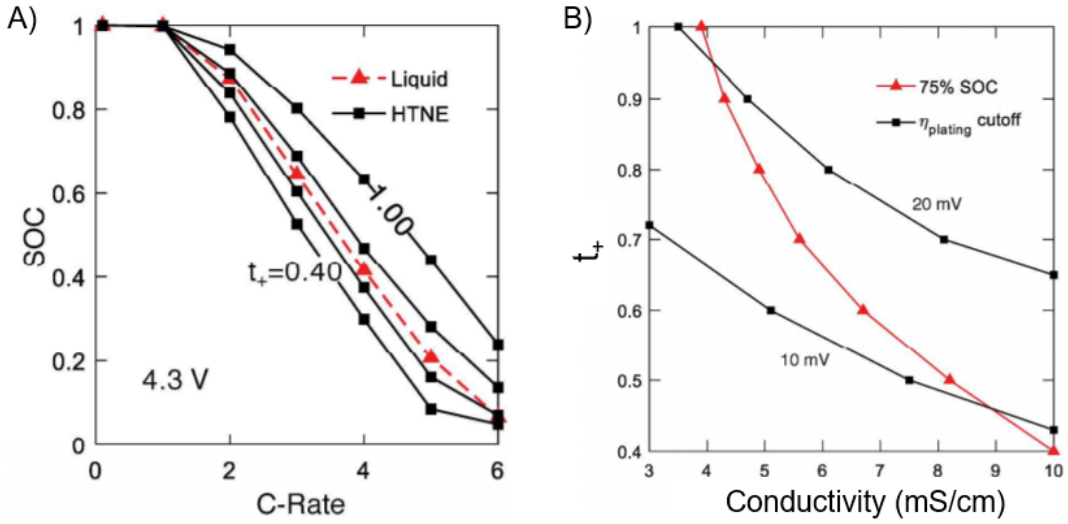

Figure 2.4: COMSOL modeling results for Li plating with HTNEs. **a.** Attainable SOC versus charge rate for standard liquid electrolyte (red dashed triangles) and HTNE (solid black squares). HTNE σ=5 mS/cm for this set of simulations, and the upper cutoff voltage was increased to 4.3 V compared to the 4.2 V cutoff in Figure 2.3d, causing Li plating conditions to be met. **b.** Minimum σ and t_+ values required to achieve 75% SOC (red triangles) at 2C with a 4.2 V cutoff voltage (from Figure 2.3e) overlaid with minimum σ and t_+ values (black squares) required to remain 10 mV and 20 mV above plating overpotential of 0 V throughout an entire charge cycle to 4.2 V at 2C.

2.4.3 Li^+ Concentration Profiles

Lithium ion concentration gradients that arise during charge limit the utilization of active graphite material in the anode. At early times during charge, steep concentration gradients develop for electrolytes with low t_+, and the concentration gradients become gradually less steep with increasing t_+, becoming completely flat as t_+ approaches one. In Figure 2.5, lithium ion concentration gradients are shown for a cell charged at 2C with σ=10mS/cm and varying t_+. At 50 seconds, the lithium ion concentration has already plummeted to 0.4 mol/dm^3 in the anode for the t_+=0.40 case, making the back end of the anode (near x=0) relatively less utilized than the front end (near x=L_{neg}). In turn, the lithium ions continue to insert primarily at the front end of the anode (because lithium ions are more abundant there compared to the back end) despite the thermodynamic penalty incurred as the front end graphite becomes more lithiated. In contrast, higher t_+ electrolytes afford more even utilization of the anode material, as the lithium ion concentration gradients are less steep, resulting in a higher concentration of lithium ions towards the back end of the anode at short times. By 1350 seconds (the end of the charge cycle for the t_+=0.40 case), the lithium ion concentration profiles for the nonunity transference number cases converge, but the more even utilization of the anode afforded by higher t_+ electrolytes reduces the overpotential required during charging, allowing the high t_+ electrolytes to attain a higher SOC before reaching the cutoff voltage.

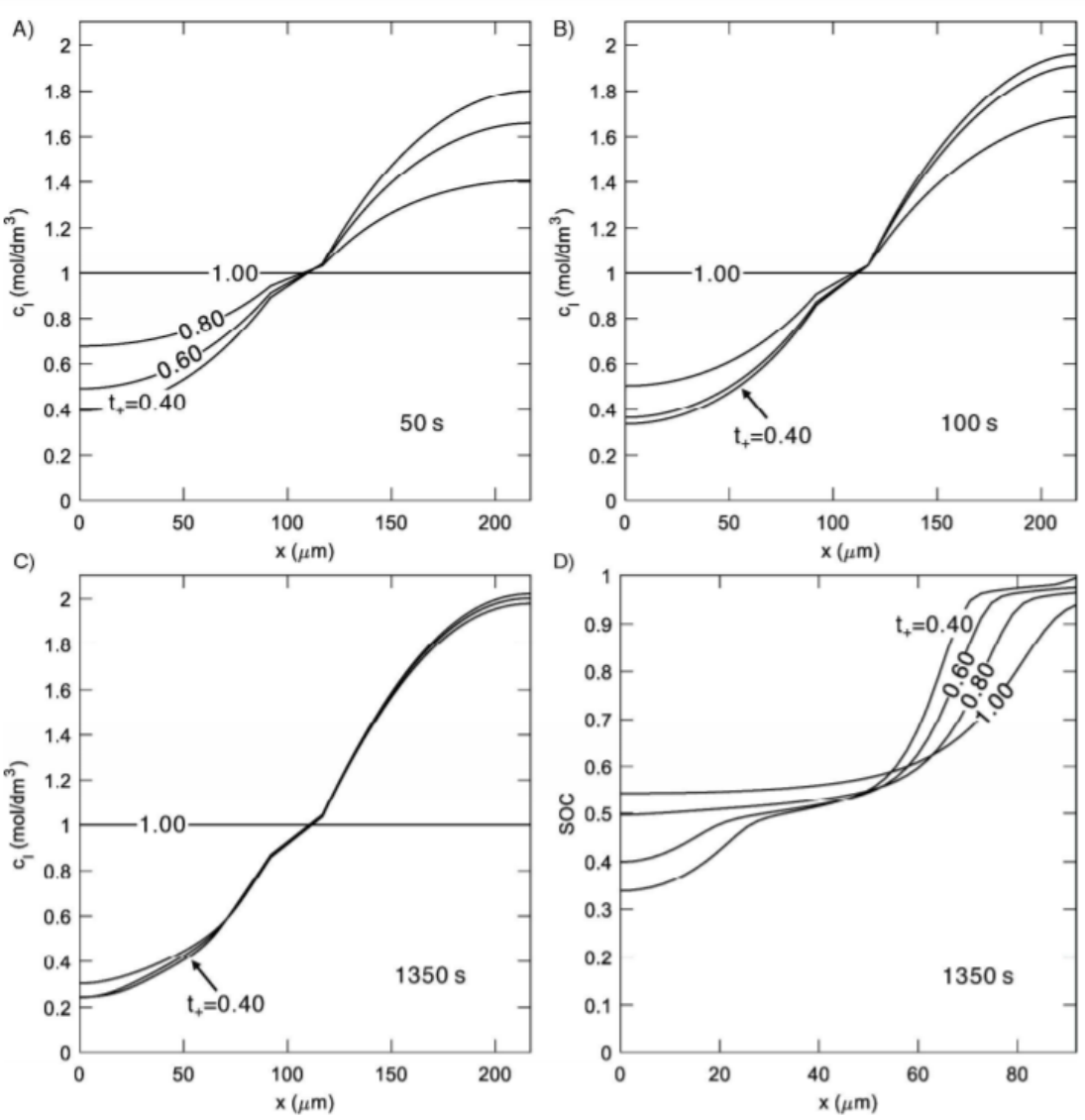

Figure 2.5: Modeled Li^+ concentration gradients at 2C charge rate with σ=10mS/cm and varying t_+ at **a.** 50 seconds, **b.** 100 seconds, and **c.** 1350 seconds. **d.** Local graphite state of charge with varying t_+ for 2C charge rate at 1350 seconds.

2.4.4 Graphite Porosity

We also explored the effect of varying the graphite anode porosity (and adjusting the anode length accordingly to retain 20% excess anode capacity) on charge performance across a range of t_+ and σ. As shown in Figure 2.6, although the attainable state of charge decreases with decreasing porosity for all tested t_+ and σ, the high transference number electrolytes decrease less relative to the standard liquid electrolyte. This insight may be useful for optimizing cell weight, as less porous electrodes in combination with high t_+ electrolytes may prove economically superior despite the loss in attainable capacity.

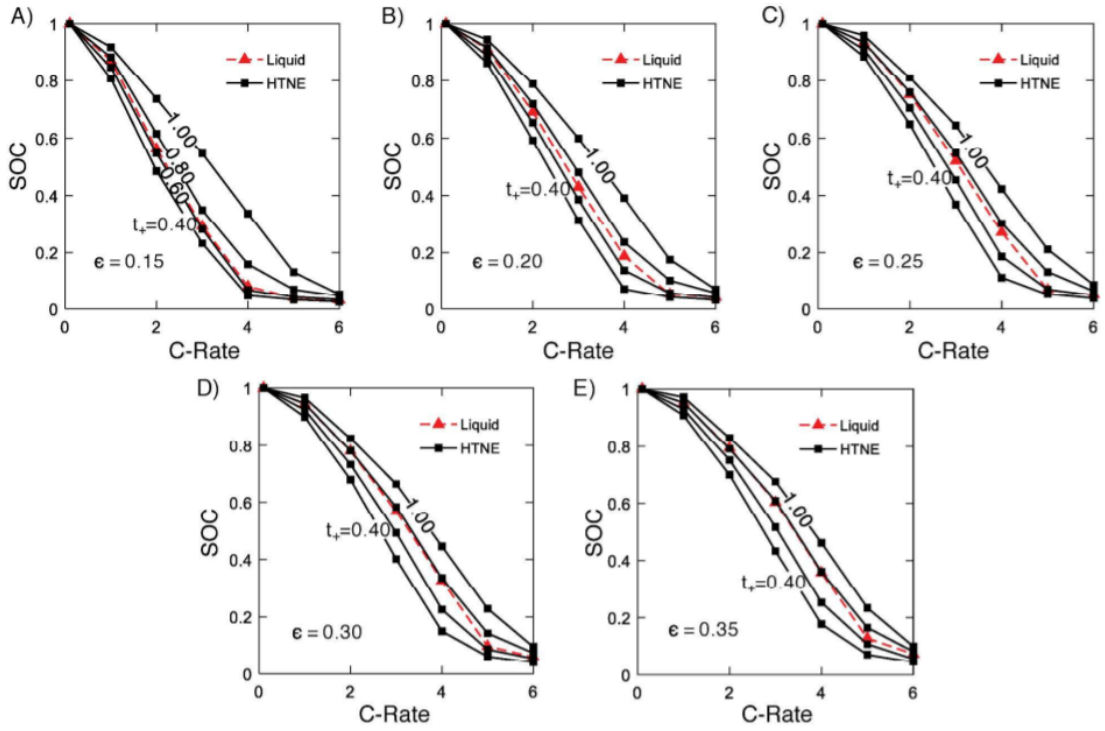

Figure 2.6: Modeled effect of graphite porosity on charge performance. Attainable state of charge versus C-rate with σ=5mS/cm and varying t_+ using graphite anode porosity of **a.** 0.15, **b.** 0.20, **c.** 0.25, **d.** 0.30, and **e.** 0.35. Cutoff voltage was set to 4.2 V for all simulations, and the graphite electrode length was adjusted to retain 20% excess anode capacity. The liquid electrolyte was assumed to have σ=10mS/cm and t_+=0.4.

2.4.5 $LiCoO_2$ Electrode Length

As shown in Figure 2.7, if we increase the $LiCoO_2$ electrode length from 100 to 150 µm (and adjust the graphite electrode length accordingly), we see that the charging performance suffers heavily, especially at high rates. However, the relative improvement offered by a high transference number electrolyte over a standard liquid electrolyte increases slightly as the electrode length increases.

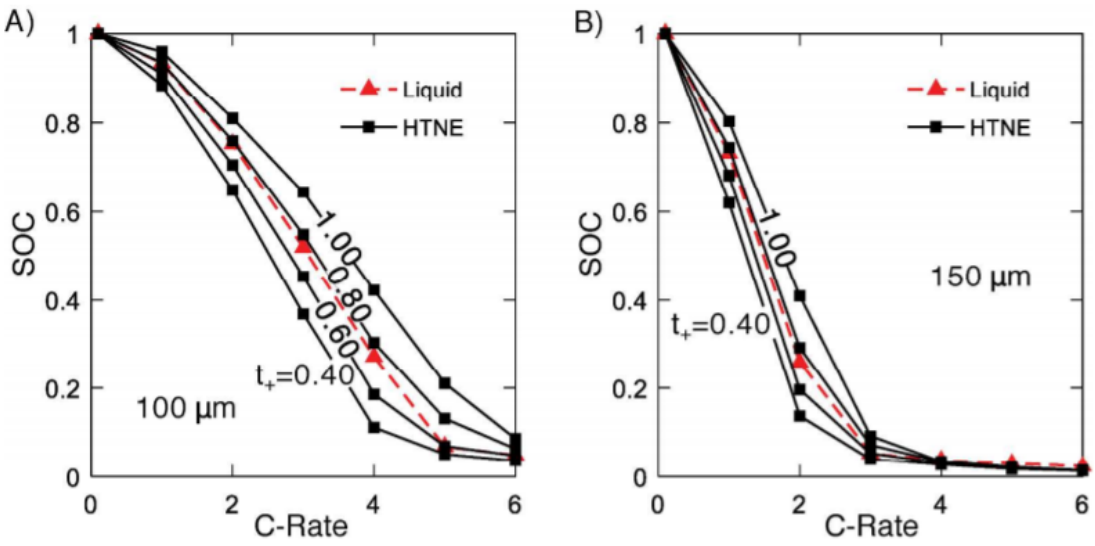

Figure 2.7: Modeled effect of $LiCoO_2$ length on charge performance. Attainable state of charge versus C-rate with σ=5mS/cm and varying t_+ using $LiCoO_2$ length of **a.** 100 µm and **b.** 150 µm. Graphite anode length was also varied to retain 20% excess anode capacity. The liquid electrolyte was assumed to have σ=10mS/cm and t_+=0.4.

2.4.6 Graphite Reaction Rate Constant

The charge performance is also sensitive to the graphite reaction rate constant used, yet this constant is difficult to measure accurately. As shown in Figure 2.8, if the rate constant is increased above the base case ($1x10^{-9}$ m/s), only slight improvements in charge performance are observed. However, lower rate constants cause a precipitous reduction in attainable SOC, severely limiting the attainable capacity at rates above 2C.

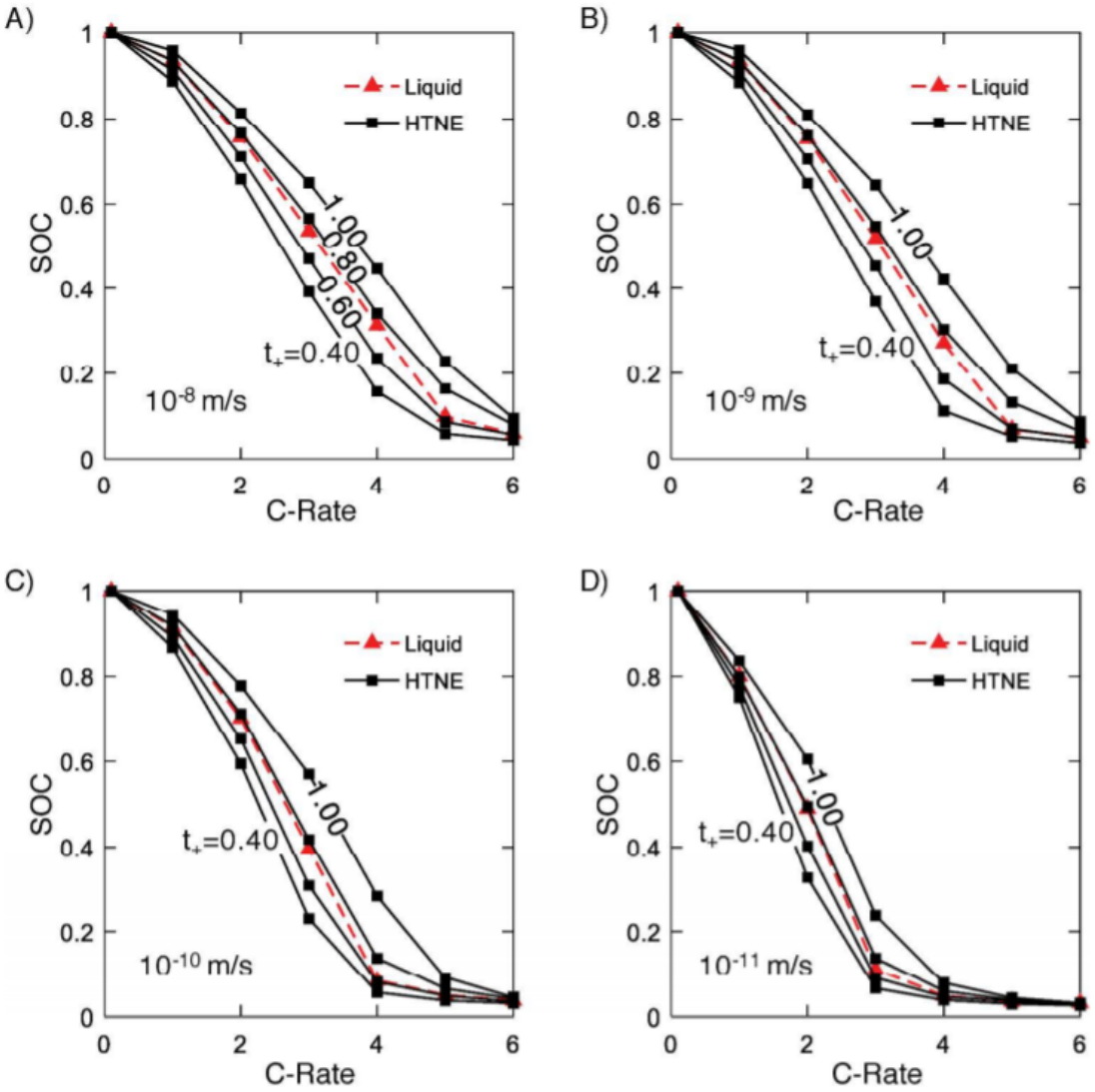

Figure 2.8: Modeled effect of graphite rate constant on charge performance. Attainable state of charge versus C-rate with σ=5mS/cm and varying t_+ using graphitic reaction rate constant of **a.** 10^{-8} m/s, **b.** 10^{-9} m/s, **c.** 10^{-10} m/s, and **d.** 10^{-11} m/s. The liquid electrolyte was assumed to have σ=10mS/cm and t_+=0.4.

2.4.7 Lithium Diffusion Coefficient, $D_{0,+}$

The diffusion coefficient of the lithium ion (D_{0+}) was held constant at 2.5x10^{-6} cm^2/s (which is the D_{0+} for the binary salt liquid electrolyte case) for all previously mentioned simulations in this chapter. In Figure 2.9, we allow D_{0+} to be reduced below 2.5x10^{-6} cm^2/s (which may be expected in a concentrated polyelectrolyte solution or in an electrolyte with a more viscous solvent), and track the t_+ and σ needed to reach 75% SOC at 2C with a 4.2 V cutoff voltage. As expected, slightly higher t_+ and σ are required to break even with the binary salt liquid electrolyte case (75% SOC at 2C) as D_{0+} is decreased.

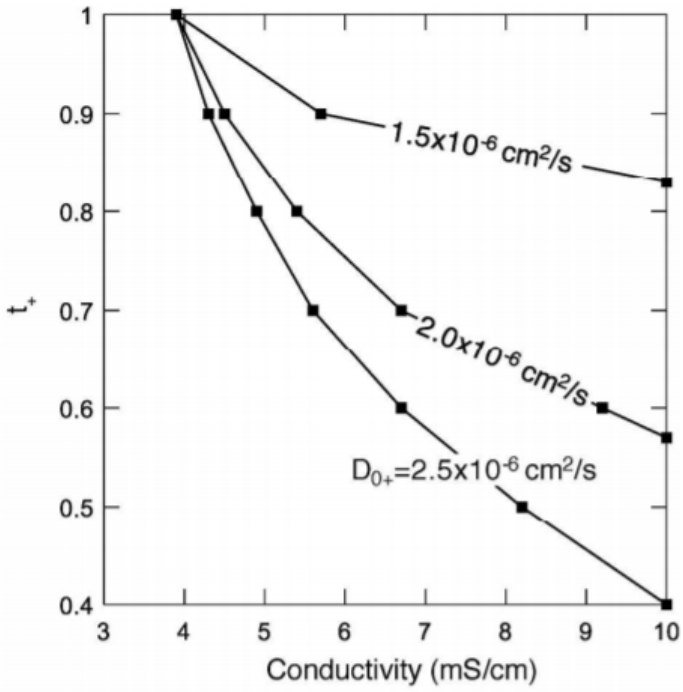

Figure 2.9: Modeled effect of D_{0+} on breakeven analysis. Minimum t_+ and σ values required to achieve 75% state of charge at 2C with 4.2 V cutoff voltage using D_{0+} of 2.5x10^{-6} cm^2/s, 2.0x10^{-6} cm^2/s, and 1.5x10^{-6} cm^2/s.

2.5 Conclusions

Our modeling work indicated that HTNEs with sufficient conductivity increased the attainable energy density and improved fast charge performance beyond what was possible with a standard liquid electrolyte. We also used the model to provide useful targets for σ and t_+ required to meet and surpass the attainable SOC at a given charge rate offered by the standard electrolyte formulation. For example, when charged at 2C, we found that an electrolyte with σ of ~5 mS/cm performed better than a standard electrolyte, provided t_+ was above ~0.75. HTNEs also delayed the expected onset of Li plating by inducing uniform lithiation of the whole graphite electrode. As next-generation electrolytes are developed for fast charge applications, they should be engineered with the benefits of a high t_+ in mind.

Chapter 3

Mass Spectrometry Titration for Quantification of Plated Lithium and Solid-Electrolyte Interphase Species

3.1 Abstract

Rapid charging of Li-ion batteries is limited by lithium plating on graphite anodes, whereby Li^+ ions are reduced to Li metal on the graphite particle surface instead of inserting between graphitic layers, which directly contributes to capacity loss due to the low reversibility of the Li plating/stripping process. Precisely identifying the onset and amount of Li plating is therefore a vital step toward remedying these issues. We demonstrate a titration technique with a detection limit of 20 nmol (5×10^{-4} mAh) Li which is used to quantify dead Li that remains on the graphite electrode after fast charging. The titration is extended to quantify the total amount of solid carbonate species and lithium acetylide (Li_2C_2) within the solid-electrolyte interphase (SEI), and electrochemical modeling is used to determine the Li plating exchange current density (10 A/m^2) and stripping efficiency (65%) of plated Li metal on graphite. These techniques provide a highly accurate measure of Li plating onset and quantitative insight into graphite SEI evolution during fast charge.[ii]

3.2 Introduction

The Department of Energy's stated goal for extreme fast charging (XFC) electric vehicle batteries is a 15-minute charge time that provides 300 miles of range, an approximate twofold improvement upon existing state-of-the-art batteries.[28] However, several outstanding challenges must be addressed to bring such batteries to fruition. First, severe Li^+ concentration gradients necessarily manifest during fast charging, depleting the Li^+ concentration within the pores of the graphite electrode near the current collector, thereby limiting the capacity

[ii]This chapter is largely adapted from previously published work in: E.J. McShane, A.M. Colclasure, D.E. Brown, Z.M. Konz, K. Smith, and B.D. McCloskey. *ACS Energy Letters.* **2020**, *5*, 2045-2051.

that can be attained for a given cutoff voltage.[6;29] Additionally, high overpotentials required to drive the necessary current can lead to Li metal deposition on the graphite particle surface.[30;31] This process, commonly referred to as Li plating, is problematic for two reasons: 1) Li is known to deposit as dendrites, which can propagate across the separator and short the cell, and 2) Li metal plating/stripping is notoriously irreversible, either due to the highly reactive nature of Li with the battery electrolyte or because a large portion of the plated Li is electronically isolated upon stripping.[32;33;34] Thus, evaluating the onset and extent of Li plating is crucial to enable XFC batteries.

Many have reported techniques that can detect Li plating during cycling – an important advance for enabling XFC – but few have been able to provide quantifiable information from the observed plating signals. Some of these methods for operando detection of Li plating on graphite include microscopy,[35] neutron diffraction,[36;37] calorimetry,[38] and monitoring of electrochemical signatures during rest and discharge.[7;8;39;40] All of the techniques come with unique challenges from a cell design, breadth of view, and sensitivity perspective, but the overarching challenge remains the lack of quantifiable information from the observed plating signal. It remains important to determine the amount of Li that has plated when a signal has been observed, particularly at the onset of plating where it is important to detect Li in the smallest amounts possible.

Lithium plating is difficult to detect and quantify for several reasons. Detection by inspection of voltage profiles is challenging because Li plating occurs simultaneously with Li insertion into graphite during charging. Quantitative detection with other techniques is difficult because Li may undergo up to four additional processes upon deposition:

1. It can be reversibly stripped from the graphite surface upon deintercalation.
2. It can chemically insert into graphite.[7;8]
3. It can become electronically isolated from the graphite, resulting in 'dead Li,' or plated Li metal which is no longer electrochemiclly active.[2]
4. It can react with other SEI components or with electrolyte to form additional SEI species, which are referred to as 'inactive Li.'[2]

We refer to the resultant isolated Li metal from the third process, along with electronically isolated Li_xC_6 ($x \leq 1$), as 'dead Li,' as both Li and Li_xC_6 would be sources of reversible Li if not for the isolation from the bulk electrode. However, we do not consider Li which has reacted with electrolyte (as mentioned in the forth process) or other SEI species under the term 'dead Li.' Using our titration technique, we show herein that the predominant mechanism of capacity loss during fast charging is the formation of dead Li, and additional electrolyte degradation reactions (forming inactive Li) become apparent after prolonged cycling.

Much of the previous work on Li plating quantification has been limited to visual inspection of graphite electrodes post-mortem. Indeed, after cells have been cycled at moderate to fast

(~1C to 6C) charge rates for hundreds of cycles, a gray film of plated Li can be observed on the extracted graphite electrode.[38;41;42] This insight is valuable to confirm that plated Li is a culprit in the resultant cell capacity loss but lacks quantitative information about the extent and onset of plating. To our knowledge, only one operando technique for quantification of plated Li on graphite at the electrode scale currently exists, and this involves a customized cylindrical electron paramagnetic resonance spectroscopy (EPR) cell with a copper wire current collector.[43] This technique is remarkably sensitive (~300 nmol Li precision) and fairly rapid (~2 minutes/measurement), but it remains important to extend these desirable traits to more conventional cell configurations. More recently, a titration gas chromatography (TGC) technique was developed for ex-situ quantification of dead Li in Li metal batteries.[32] In the TGC work, extracted Cu electrodes and separators from Cu-Li cells were placed into an Ar-filled air-tight septum vessel and water was injected into the vessel, producing H_2 gas from the reaction of water with residual dead Li. The headspace of the vessel was sampled with an air-tight syringe and injected into a GC for H_2 quantification, with a reported sensitivity of ~150 nmol Li.[32]

In this chapter, we demonstrate a mass spectrometry titration (MST) for dead Li quantification on graphite with a detection limit of 20 nmol Li (see Section 3.9.3), which corresponds to 0.5 µAh of total dead Li. This technique is a modified version of a similar titration[44;45] to quantify Li_2CO_3 on extracted Li-O_2 battery cathodes and was more recently used to quantify surface Li_2CO_3 on Li-rich and Li-stoichiometric NMC cathodes.[46] With MST, we precisely identify: 1) the charge rate at which Li plating is observed if the electrode is charged to its nominal full capacity (corresponding to 372 mAh/g graphite), and 2) the state of charge at which Li plating commences at a 4C rate (full charge in 15 minutes). We also use electrochemical modeling to determine the Li plating exchange current density and the efficiency of plated Li stripping during discharge.

3.3 Mass Spectrometry Titration (MST)

A comprehensive description of the titration procedure can be found in Section 3.9.1. Graphite electrodes (2.18 mAh/cm^2, 91.83 wt% Superior Graphite SLC1506T, 2 wt% Timcal C45 carbon, 6 wt% Kureha 9300 PVDF binder, 0.17 wt% oxalic acid, 6.38 mg/cm^2, 37.4% porosity, 47 µm coating thickness) were provided by the Cell Analysis, Modeling and Prototyping (CAMP) facility at Argonne National Laboratory. Electrodes were punched in 11 mm disks for the studies outlined in Figures 3.2, 3.3, and 3.4, and 12.5 mm disks were used for the prolonged cycling study in Figure 3.5. Cells were cycled on a Biologic VMP3 potentiostat at 30 °C in Li-graphite Swagelok cells (12.5 mm inner diameter) with 1.2 M $LiPF_6$ in ethylene carbonate/ethyl methyl carbonate (EC/EMC) (3:7 wt/wt) electrolyte and a Whatman QMA glass fiber separator. After cycling (always ending the cycle with delithiation to 1.5 V), the graphite electrodes were extracted from the cells and rinsed gently (except where otherwise noted) for one minute in 300 µL of dimethyl carbonate three times to remove residual electrolyte, which was necessary to avoid CO_2 evolution from residual ethylene carbonate upon titration.[47] We also examined the influence of rinsing on the amount of Li detected, as is

discussed later. The electrodes were then dried in the glovebox antechamber and preserved in airtight vials in the glovebox prior to titration. To quantify the dead Li on the extracted electrode, the sample was placed in a titration vessel with a septum port as described in Section 3.9.1 and attached to an in-line mass spectrometer (MS), all the while maintaining an air-free environment in the vessel. After attaching the vessel and acquiring a baseline on the MS, 3.5 M sulfuric acid was injected into the vessel, evolving H_2 via Reactions 3.3.1 and 3.3.2 (from dead Li metal and dead Li_xC_6 that has become electronically isolated during the first few cycles), CO_2 via Reactions 3.3.4, 3.3.3, and 3.3.5 (from carbonate-containing species in the SEI such as lithium ethylene monocarbonate (LiEMC), lithium ethylene dicarbonate (LiEDC), or lithium carbonate), and acetylene (C_2H_2) via Reaction 3.3.6 from lithium acetylide (Li_2C_2).[48;49;50] We note here that we are not able to differentiate between H_2 evolved due to Reactions 3.3.1 and 3.3.2. Given that we always perform these titrations after a slow discharge to 1.5 V, where no reversible Li_xC_6 or Li metal should be present on the electrode, we define any H_2 evolved as originating from 'dead Li,' a combination of Li and Li_xC_6 that persists after discharge. The headspace of the titration vessel was regularly sampled at two-minute intervals and sent to the MS until the m/z=2, m/z=44, and m/z=26 signals had fully attenuated, allowing us to quantify the total amount of H_2, CO_2, and C_2H_2, respectively, evolved. Measurement error from baseline correction of the titration gas evolution curves was estimated to be ±10% of the measured total gas evolved for H_2 and CO_2 and ±20% for C_2H_2 due to differences in calibration (see Section 3.9.2). An illustration of the titration technique is shown in Figure 3.1.

$$\mathrm{Li + H_2O \longrightarrow LiOH + \frac{1}{2}H_2} \tag{3.3.1}$$

$$\mathrm{Li_xC_6 + xH_2O \longrightarrow xLiOH + C_6 + \frac{x}{2}H_2} \tag{3.3.2}$$

$$\mathrm{(CH_2OCO_2Li)_2\ (LiEDC) + 2\,H^+ \longrightarrow (CH_2OH)_2\ (EG) + 2\,Li^+ + 2\,CO_2} \tag{3.3.3}$$

$$\mathrm{HOCH_2CH_2OCO_2Li\ (LiEMC) + H^+ \longrightarrow (CH_2OH)_2\ (EG) + Li^+ + CO_2} \tag{3.3.4}$$

$$\mathrm{Li_2CO_3 + 2\,H^+ \longrightarrow H_2O + 2\,Li^+ + CO_2} \tag{3.3.5}$$

$$\mathrm{Li_2C_2 + 2\,H^+ \longrightarrow 2\,Li^+ + C_2H_2} \tag{3.3.6}$$

Figure 3.1: MST Schematic. Left side: Common gases evolved during MST. SEI components are primarily solid carbonates (e.g., lithium ethylene dicarbonate), which evolve CO_2 upon immersion in acid. Li metal is known to form lithium acetylide (Li_2C_2) in small quantities when reacted with other carbonate-containing SEI components. Upon exposure to water, Li_2C_2 releases acetylene gas (C_2H_2). Li metal is highly reactive with water and evolves H_2 gas. Right panel: an image of the MST titration vessel. An electrode is sealed in the vessel and acid is injected. Gases are carried to a mass spectrometer where they are quantified using an in-line gas handling unit.

3.4 Electrochemical Modeling

To interpret results and predict lithium plating/stripping amounts during XFC, we employed a previously developed macro-homogeneous electrochemical half-cell model[30;31;51] coupled with a lithium plating/stripping model which uses the framework proposed by Ren et al.[52] The electrochemical properties of anodes using Superior 1506T graphite have been well characterized and reported in previous work.[30;31] Due to difficulties in the galvanostatic intermittent titration technique (GITT) for multi-phase materials, the solid-state diffusion coefficient and exchange current density were approximated from fitting to electrochemical data. Reported electrolyte transport properties for standard 1.2 M $LiPF_6$ in 3:7 by weight EC:EMC electrolyte were obtained from literature.[51] Lastly, the lithium electrode was treated as an ideal electrode with the exchange current density set artificially high to prevent any significant overpotential at all charging rates. Relevant model parameters are summarized in Tables 3.1 and 3.2. This model was developed by collaborators at the National Renewable Energy Laboratory and summarized with their permission in comparison to our experimental results.

3.5 Dead Li and SEI Trends with C-rate

Each Li-graphite half-cell tested underwent two C/10 formation cycles with 0.010 V and 1.5 V cutoff potentials before fast charging, with the C/10 rate based on a 372 mAh/g graphite lithiation capacity. Here we refer to lithium insertion into graphite as 'charging' and deinsertion as 'discharging' despite the half-cell configuration. Figure 3.9a presents a

typical cell cycling protocol: two formation cycles followed by three charge/discharge cycles with constant-current (CC) charge to 372 mAh/g and CC discharge to 1.5 V. The charge rates were varied for different cells (C/4, C/2, 1C, 2C, and 4C) while the discharge rates remained constant (C/4) for all cells. Similar results were obtained using slower discharge rates; for example, the same amount (within standard cell-to-cell variability) of dead Li was measured using a C/4 and a C/10 discharge rate following a given charge rate, indicating that the C/4 discharge was sufficient to remove all reversible Li and Li_xC_6 from the graphite (see Figure 3.13). The amount of dead Li present after the final discharge to 1.5 V, as well as the cumulative irreversible capacity as measured using the difference between charge and discharge capacity of all fast charge cycles (i.e., not including the irreversible capacity of the formation cycles), is presented in Figure 3.2a. Of note, the cells cycled at the lowest charge rate studied, C/4, show non-zero dead Li (~100 nmol/cm^2) as measured using our titration protocol. We do not attribute this to plated Li metal, as we do not expect Li plating at a slow C/4 charge rate, but rather to electronically isolated Li_xC_6 that is inevitably present due to volumetric expansion and subsequent detachment of Li_xC_6 during the first formation cycle.[53] This is supported by a control experiment wherein we titrated an electrode after just two C/10 formation cycles and measured 170 nmol/cm^2 dead Li, statistically equivalent to the dead Li present on the electrode that underwent both the formation cycles and C/4 cycles (Figure 3.2a). Along these lines, we can conclude from Figure 3.2a that plating commences between C/2 and 1C, as the dead Li measured for C/4 and C/2 are within error of the 170 nmol/cm^2 measured after just formation cycling, while the 1C case is clearly higher (~400 nmol/cm^2).

By comparison of the dead Li measured via titration (red) and the total irreversible capacities (black) in Figure 3.2a, we can conclude that a substantial portion of the irreversible capacity at higher charge rates is in fact due to dead Li, as both the dead Li capacities and cumulative irreversible capacities increase similarly with increasing charge rate. We define an offset capacity (Q_{offset}) in Equation 3.5.1, which is the difference between the total irreversible capacity (Q_{tot}) from cycling (excluding formation cycles) and the equivalent capacity of dead Li (Q_{Li}) measured via titration, and we plot this for each C-rate in Figure 3.2b. The offset capacity is similar within error at a baseline value of 20-30 µAh/cm^2 for C-rates of 2C and below, with a slight increase at 4C.

$$Q_{offset} = Q_{tot} - Q_{Li} \tag{3.5.1}$$

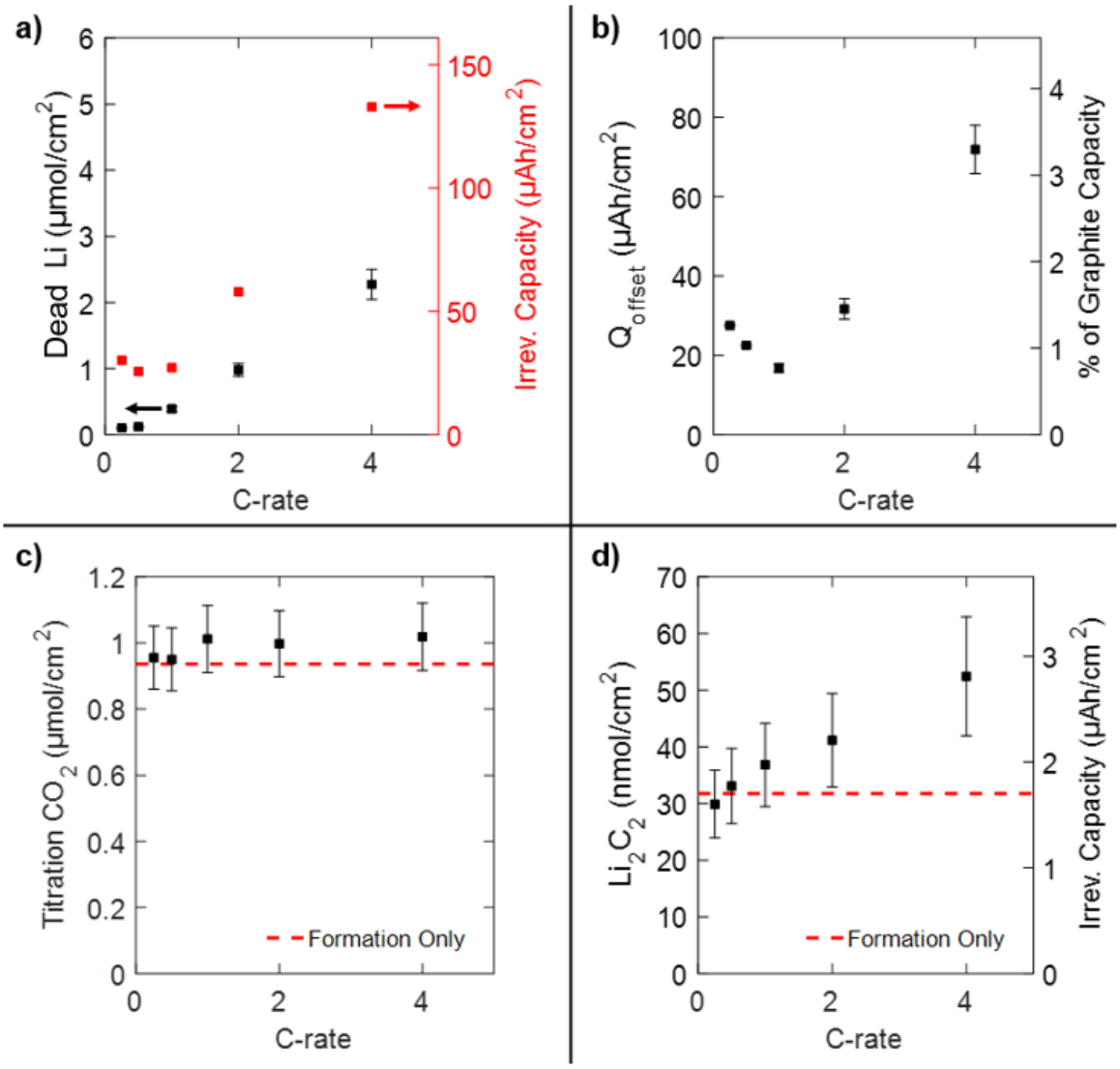

Figure 3.2: Quantification of dead Li and SEI via MST as a function of charge C-rate. Acid titrations were performed on 11 mm diameter graphite electrodes cycled three times in Li-graphite cells at various charge rates with slow C/4 discharge rate (see Figure 3.9a for full voltage profiles). **a.** Dead Li (black) measured via H_2 evolution upon titration and cumulative irreversible capacity (red, obtained from cycling data) of the three fast charge cycles as a function of charge C-rate. Left and right y-axes are scaled equivalently (i.e. 1 µmol Li/26.8 µAh, see Section 3.9.4). Error bars indicate measurement error, which is 10% of the total measured dead Li for Li titration results and <1 µAh for irreversible capacities. **b.** Q_{offset} (defined in Equation 3.5.1) as a function of C-rate. **c.** CO_2 evolution upon titration as a function of C-rate. Error bars indicate measurement error of 10% of the total measured CO_2. Amount of CO_2 measured upon titration for an electrode that underwent only formation cycles is overlaid as a red dashed line for reference. **d.** Li_2C_2 measured via titration as a function of C-rate. Error bars indicate measurement error of 20% of the total measured Li_2C_2. Equivalent capacity of Li_2C_2 is shown on the right y-axis (see Section 3.9.7). Amount of Li_2C_2 measured for an electrode that underwent only formation cycles is overlaid as a red dashed line for reference. All data points are averages from the results of two cells, and the full data set along with a breakdown of the percent contribution of each source of capacity loss at each C-rate can be found in Sections 3.9.5 and 3.9.6.

The baseline Q_{offset} observed at all C-rates could arise from a number of different phenomena, including electrode rinsing or the formation of additional SEI components. To understand the impact of rinsing, we titrated an unrinsed electrode that underwent the standard formation cycles followed by three 4C charge, C/4 discharge cycles. We found that Q_{offset} and the measured dead Li were similar within error to those reported in Figures 3.2a and 3.2b for the rinsed electrode counterparts (see Figure 3.11). Thus, dislodgement of dead Li from rinsing is not a major contributor to the offset capacity after just three fast charge cycles (we will show later that rinsing does influence the titration results after more cycles). Another plausible explanation for the observed Q_{offset} is further SEI formation beyond the two formation cycles. We must be careful when addressing 'SEI formation' broadly because the species comprising the SEI on graphite are diverse, almost always including solid carbonates, LiF, and Li_2O, but occasionally also reported to include trace amounts of oxalates, succinates, and alkoxides, although truly quantitative information remains elusive.[1;54;55;56] From our carbonate titration results in Figure 3.2c, we see that the amount of carbonate-containing SEI remains within error of the amount measured after just formation cycling for all C-rates, indicating that either carbonates do not continue to form beyond the formation cycles or are only loosely attached to the surface such that they are removed during the rinsing procedure. As outlined in Section 3.9.7, the slight increase in CO_2 evolution observed for the 4C case only amounts to ~5 µAh/cm^2 equivalent capacity, which is not enough to explain the total increase in Q_{offset} at 4C. Finally, we discuss the possibility that Q_{offset} might result from plated Li reacting to form a new (likely non-carbonate) species. Multiple reports have indicated that Li_2C_2 is observed on plated Li metal when using a $LiPF_6$ in EC/EMC electrolyte, and the Li_2C_2 hydrolyzes to form C_2H_2 gas upon exposure to water.[49;50] In Figure 3.2d, we see that the amount of Li_2C_2 measured via the C_2H_2 evolved upon titration grows with increasing C-rate, indicating that Li_2C_2 formation is correlated with total Li plated (which also increases with increasing C-rate above C/2) and contributes to the increased Q_{offset} at 4C. The Li_2C_2-forming reaction during fast charge cycling is likely chemical as opposed to electrochemical, as the amount of Li_2C_2 grows with increasing OCV time between charge and discharge (see Figure 3.14d), when plated Li is free to react chemically, and we will show in the Section 3.7 that Li_2C_2 is likely formed via a chemical reaction between plated Li and $LiRCO_3$ in the SEI. With this in mind, we can calculate an equivalent capacity of Li_2C_2 (right y-axis in Figure 3.2d) based on the loss of Li inventory due to Li_2C_2 formation (see Section 3.9.7), and we see that again Li_2C_2 alone cannot account for the overall increase in Q_{offset} with increasing charge rate, although we use the increased amount of Li_2C_2 as evidence that the relatively larger amount of plated Li at high charge rates is more susceptible to reaction. Other species that are rinsed off, dissolve into the electrolyte, or cannot be measured with our titration must account for the remainder of the offset. In summary, a substantial portion of the irreversible capacity from fast charging can be attributed to dead Li, but further SEI formation beyond the formation cycles and the reaction of plated Li with electrolyte and other SEI species also contribute, especially at higher charge rates. The baseline Q_{offset} is due to formation of non-carbonate SEI species such as LiF or Li_2O or 'loose' carbonate species formed beyond the formation cycles,[1] and the increase in offset capacity at higher C-rates is due to the reaction of plated Li to form new species such as Li_2C_2 and other non-carbonates. This is summarized in Figure 3.9, which quantifies the relative contributions of dead Li, solid carbonate formation, Li_2C_2 formation, and other product formation (e.g., LiF, Li_2O, and

electrolyte soluble species) to the observed irreversible capacity.

It should be reiterated here that our technique is limited to quantifying dead Li when the graphite electrode is in the fully discharged state. To obtain information about the expected amount of plated Li at other states during cycling, we combine our experimental data with electrochemical modeling as described in the Section 3.4. The model was first tested against cell cycling data to ensure fidelity between the experimental and model-predicted voltage profiles. From this fitting, we were also able to determine an appropriate exchange current density for the Li plating process, $i_{0,Li}$. In Figure 3.3a, we see that, while we experimentally observe a consistent decrease in voltage throughout the 4C charge, the model predicts a precipitous drop in the voltage near the end of the 4C charge for $i_{0,Li}$ less than ~5 A/m^2, and the model more closely matches experimental data when $i_{0,Li}$=10 A/m^2. Further, other $i_{0,Li}$ values reported in the literature are consistently at or near $i_{0,Li}$=10 A/m^2.[52;57] Thus, we use $i_{0,Li}$ of 10 A/m^2 for further analysis. The model inputs were designed to replicate the charging conditions in Figure 3.2 by simulating a single charge and multiplying the predicted amount of plated Li by three to simulate three charge-discharge cycles. We note that the amount of predicted dead Li if all Li plates irreversibly (red line in Figure 3.3b) is around 3 times that measured at 4C in Figure 3.2a. This difference can be rationalized by assuming that a sizable fraction of lithium plated during fast charging is reversibly stripped during the C/4 discharge. Using a lithium stripping efficiency (α_{str}, defined as the percent of plated lithium that is stripped on subsequent discharge) of 65%, which has been identified as a reasonable value in prior reports,[43] our model with $i_{0,Li}$=10A/m^2 is in good agreement with the experimentally quantified amount of dead Li (Figure 3.3b, green line). Modeling of lithium stripping is discussed in more detail in Section 3.9.11.

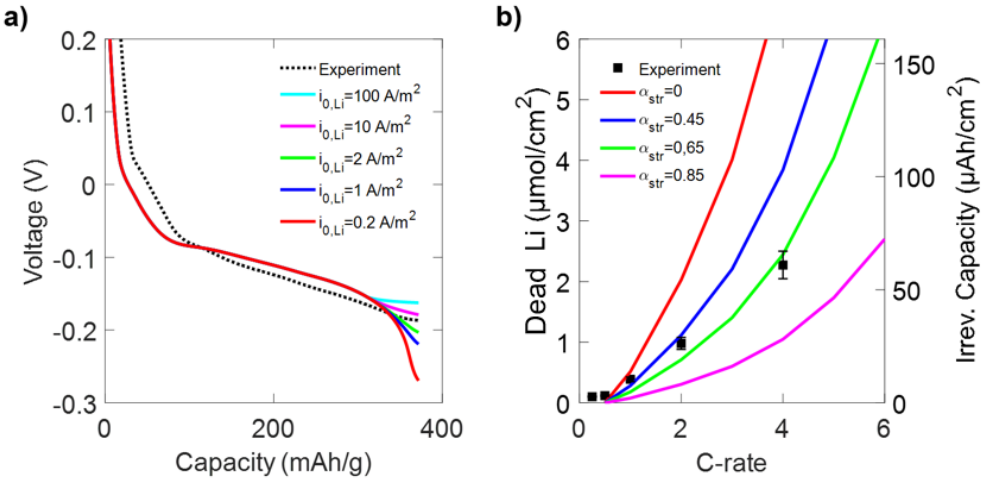

Figure 3.3: Model comparison to experimentally measured dead Li and voltage profile. **a.** Experimentally measured 4C charge voltage profile (dotted line) overlaid with 4C charge modeling results (solid lines) with varying Li plating exchange current densities ($i_{0,Li}$). **b.** Experimentally determined dead Li (black squares) from Figure 3.2a overlaid with model-determined dead Li (solid lines) assuming various Li stripping efficiencies (α_{str}) using $i_{0,Li}$=10 A/m^2. Modeling results were obtained by simulating a single 4C charge and multiplying the resultant dead Li by three to simulate three CC charge-discharge cycles to directly compare to Figure 3.2 results.

3.6 Dead Li and SEI Trends with State of Charge (SOC)

With our ability to precisely quantify dead Li, we were also able to determine the onset of Li plating at the fastest tested 4C charge rate and compare this against the model. To do this, we cycled a different set of cells, each with two C/10 formation cycles as before followed by one 4C charge to varying capacities corresponding to 20%, 40%, 60%, 80%, and 100% SOC (assuming 372 mAh/g capacity at 100% SOC) and a subsequent C/4 discharge to 1.5 V (see Figure 3.4a). From Figure 3.4b, we see that dead Li below 80% SOC remains reasonably constant at ~250 nmol/cm^2 (again within error of 170 nmol/cm^2, the amount measured after just formation cycling) and is likely due to electronically isolated Li_xC_6 given the similarity with the dead Li after only the formation cycles. Since we typically measure a range of 100-250 nmol/cm^2 (a modest range corresponding to only ~0.18% of the total graphite capacity) dead Li from isolated Li_xC_6 on samples where we expect no Li plating, the consistency at ~250 nmol/cm^2 in this study is notable. We expect this consistency is due to the close proximity from which the electrode samples were punched from the full electrode laminate sheet, imparting less sample-to-sample variability. With this in mind, we conclude that plating occurs at 80-90% SOC, as there is a clear rise in the measured dead Li above 80% SOC. This is in excellent agreement with the expected onset of Li plating based on the electrochemical model, as shown in Figure 3.4b. The model also predicts that Li plating commences at 99% SOC at 1C and at 96% SOC at 2C, both of which are reasonable values given the relative amounts of plated Li quantified in Figure 3.2a. As evidenced by Figures 3.4c and 3.4d, further carbonate-containing SEI formation and the reaction of plated Li to form Li_2C_2 do not influence our results, indicating that the relatively small amount of plated Li in this study is low enough to remain shielded from degradation by the already existing SEI from formation cycling. We note here that plating occurs at a high SOC because the electrodes used in this study are thin compared to typical electric vehicle battery loadings. We would expect plating to occur at lower SOCs for thicker electrodes, and this will be a subject of future studies. Additionally, plating does not occur until the potential falls well below 0 V vs. Li/Li$^+$ due to the voltage loss across the thick separator.

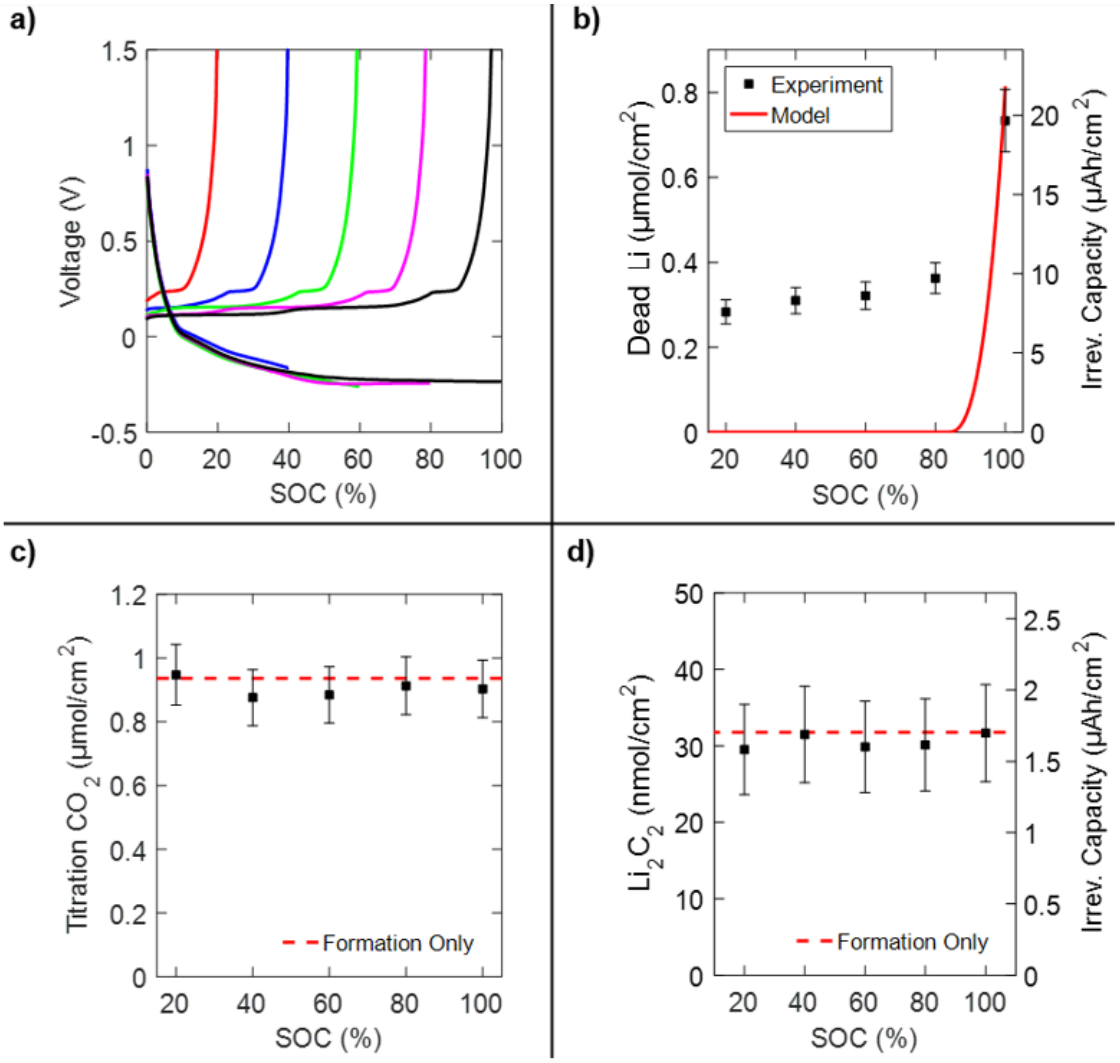

Figure 3.4: Quantification of dead Li and SEI via MST as a function of SOC. **a.** Overlaid voltage profiles of five cells charged to 20%, 40%, 60%, 80%, and 100% SOC at 4C followed by C/4 discharge to 1.5 V. Formation cycles are omitted for clarity. **b.** Dead Li measured via titration for the five electrodes from panel a overlaid with model-predicted dead Li for one simulated 4C charge assuming 65% reversible stripping of plated Li. **c.** CO_2 evolution upon titration as a function of SOC with reference CO_2 evolution after just two formation cycles shown with a red dashed line. **d.** Li_2C_2 measured via titration as a function of SOC with reference Li_2C_2 amount measured after just two formation cycles shown with a red dashed line.

3.7 Dead Li and SEI Trends with Cycling

Comparing Figures 3.2a and 3.4b, we notice that the amount of dead Li after three 4C charge cycles (~2.1 µmol/cm^2) is about three times the amount after a single 4C cycle (~0.7 µmol/cm^2). In Figure 3.5, we explore this trend further, now using electrodes of full 12.5 mm diameter to fill the interior of the cell and avoid degradation on the edges during prolonged cycling. We see in Figure 3.5a that the irreversible capacity continues to increase linearly with cycle number up to 10 cycles, which is consistent with the linear capacity

decay typically observed over the first ~30 fast charge cycles in full pouch cells with similar graphite electrodes.[58] However, the amount of dead Li begins to taper off with increasing cycle number, resulting in increased Q_{offset} as shown in Figure 3.5b. A possible explanation for this behavior is that our post-cycling rinsing procedure (three brief rinses in DMC) removes some loosely bound Li that deposited during cycling. From the discussion related to Figure 3.2a and Figure 3.11, we know that rinsing has minimal effect on the measured amount of dead Li after three 4C charge cycles. Analyzing Figure 3.5a, however, we notice that rinsing begins to have a noticeable effect on the measured amount of dead Li for five 4C charge cycles and above. The unrinsed electrode cycled 10 times, for example, had ~4 µmol/cm^2 more dead Li compared to its rinsed counterpart.

We also observe a clear rise in carbonate-containing species (see Figure 3.5c) after 5 and 10 cycles, which coincides with the point which rinsing removes a portion of the plated Li. We suspect that beyond 5 cycles, Li plates increasingly as mossy or dendritic Li which is more susceptible to being removed by rinsing given that it is poorly adhered to the graphite surface. Furthermore, mossy Li has very high electrolyte-exposed Li surface area, which causes more electrolyte degradation, resulting in more solid carbonate deposition in the SEI (as shown in Figure 3.5c). Interestingly, the measured amount of Li_2C_2 (as shown in Figure 3.5d) grows linearly with cycling and appears to be independent of rinsing. We hypothesize that Li_2C_2 forms via the chemical reaction of plated Li with existing carbonate-containing SEI species and remains in the SEI bulk as opposed to near the SEI-electrolyte interface, which makes Li_2C_2 less susceptible to being removed during rinsing. Previous studies have shown that Li_2C_2 can form from the reduction of Li_2CO_3.[49;59] This electrochemical reaction can be extended in our scenario to a chemical reaction involving the coupled oxidation of plated Li metal and reduction of Li_2CO_3 (and perhaps alkyl carbonates as well) to form Li_2C_2 chemically. This is further supported by our study on the influence of OCV rest time between charge and discharge (see Section 3.9.10), where we observe that a longer OCV rest time after 4C charge (when a large amount of plated Li is free to react chemically before chemically inserting into graphite or being stripped from the surface) leads to increased Li_2C_2 formation. A comprehensive breakdown of the relative contributions of solid carbonates, Li_2C_2, and other species to the observed irreversible capacity can be found in Figure 3.10. In summary, plated Li undergoes a chemical reaction with Li_2CO_3 (and perhaps alkyl carbonates as well) to form a consistent amount of Li_2C_2 in the bulk of the SEI every cycle, and mossy plated Li (which is susceptible to being removed by rinsing) present after 5 and 10 cycles leads to more solid carbonate formation on the exposed Li surface area.

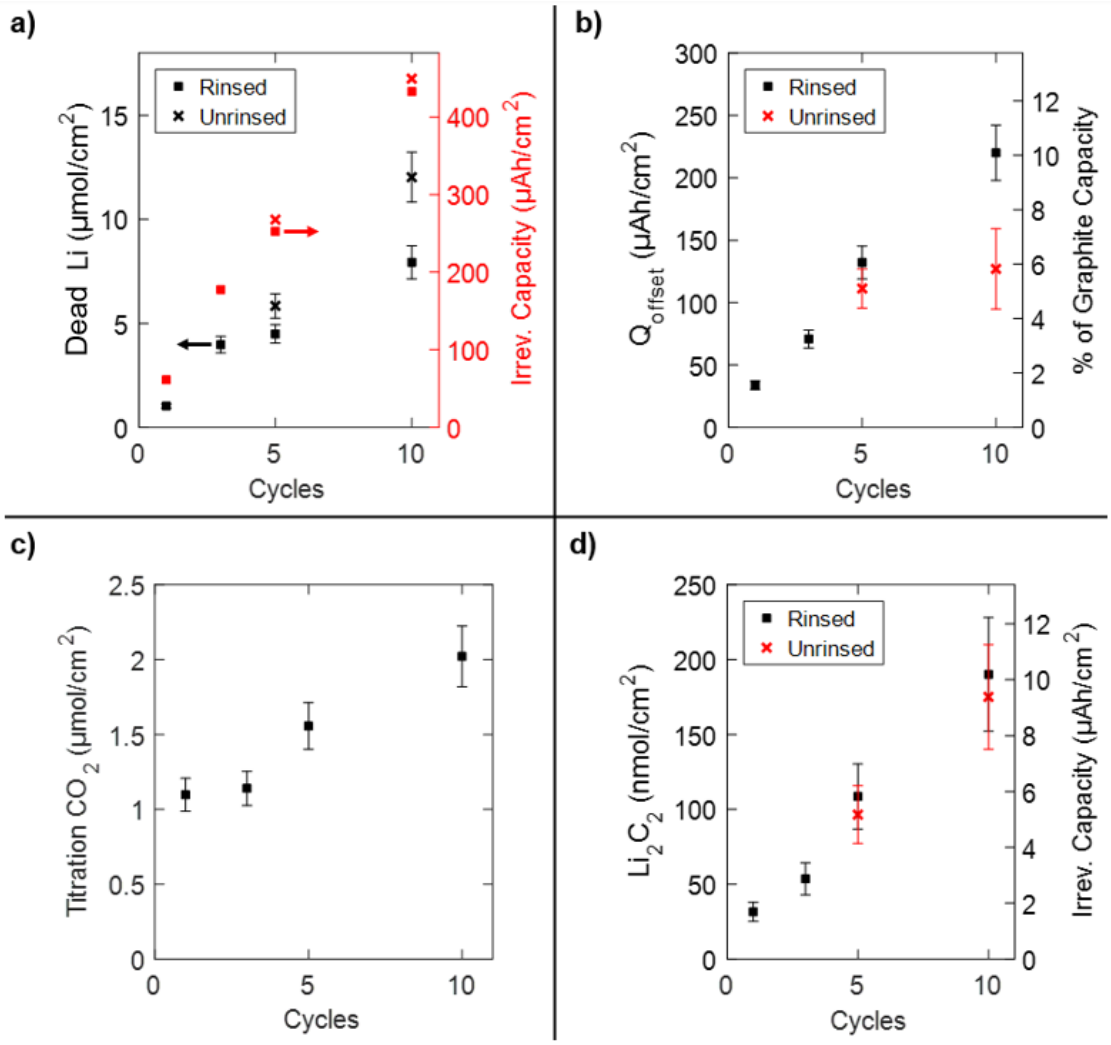

Figure 3.5: Quantification of dead Li and SEI via MST as a function of cycle number. Acid titrations were performed on 12.5 mm diameter graphite electrodes cycled multiple times at 4C charge rate. **a.** Dead Li (black) measured via titration and cumulative irreversible capacity after formation (red) for electrodes that have undergone varying numbers of 4C charge, C/4 discharge cycles. Rinsed extracted electrode samples are shown with square markers while unrinsed samples are shown with 'x' markers. **b.** Offset capacity (defined in Equation 3.5.1) as a function of cycle number for rinsed and unrinsed samples. **c.** CO_2 evolution upon titration as a function of cycle number. **d.** Li_2C_2 amount as a function of cycle number. A full breakdown of the relative contribution of each species to the observed irreversible capacity can be found in Figure 3.10.

3.8 Conclusions

In summary, we have developed a highly sensitive titration technique to quantify dead Li, carbonate-containing SEI, and Li_2C_2 on cycled graphite electrodes. Using the titration technique, we: 1) identified the SOC at which plating occurred at a fast 4C charge rate, 2) determined the charge rate at which plating occurred if charged to full nominal capacity, and 3) quantified the contribution of dead Li, solid carbonates, and Li_2C_2 to the observed

irreversible capacity during fast charging. By employing electrochemical modeling, we also determined the Li plating exchange current density and the stripping efficiency of plated Li on graphite. This study lays the groundwork for benchmarking the detection limit of other Li plating detection techniques and provides an avenue to pursue more comprehensive studies of plating, stripping, and chemical insertion of Li on graphite surfaces.

3.9 Supporting Information

3.9.1 MST Procedure

The graphite electrode sample is first placed in an airtight titration vessel (depicted in Figure 3.1) inside the glovebox. The cap of the vessel has a septum port (for acid injection) as well as two protruding capillaries which are capped prior to removal from the glovebox. To attach the vessel to the MST apparatus, the lines of the apparatus are purged with Ar, and the transfer line is removed while maintaining a positive Ar flow. The left capillary cap of the titration vessel is removed, and this side is quickly connected to the MST apparatus. The right capillary cap is then removed from the vessel, allowing Ar to flow through the vessel briefly, and the right capillary is then quickly connected to the MST apparatus as well. With the vessel attached, Ar is continuously flowed through the vessel for five minutes to purge the headspace of any residual contaminants. The mass spectrometer is then turned on, and the filament is allowed to operate for one hour until ion currents have stabilized. A Labview program is used to sample gas from the vessel headspace every two minutes, replenish Ar to the vessel after sampling, and record ion currents, pressure, and temperature throughout the experiment. While the Labview program is running, 3.5 M H_2SO_4 is injected with an airtight syringe through the septum port on the titration vessel. Previous work on quantification of Li_2CO_3 on cathode materials[60] using the same MST setup showed that any concentration above 1 M H_2SO_4 provides sufficient excess acid to react all present carbonate species, and H_2SO_4 is chosen over other acids to remain consistent with similar previous carbonate titration studies.[44;46] Carbonate titrations using phosphoric acid have also been reported and yield similar results.[45] We also emphasize issues related to safety: the maximum amount of gas evolved in any single experiment was roughly 15 µmol, which we calculate would only increase the pressure of our sealed titration vessel ~30 torr, a reasonable value given the wall thickness of our glass titration vessel. Any use of these techniques should carefully consider maximum pressure rises that could occur due to gas evolution and limit the total amount of electrode titrated according to the expected amount of dead Li. Furthermore, an inert gas should be used as the carrier gas to ensure evolved H_2 does not combust given the high exothermicity of Li reacting with acid or water.

3.9.2 Titration Data Analysis Example

To determine the total amount of H_2, CO_2, and C_2H_2 evolved upon titration, 2 mL of the titration vessel headspace is sampled at 2-minute intervals. The gas is sent to a mass spectrometer which has been calibrated with various concentrations of H_2, CO_2, and O_2 (in place of C_2H_2, introducing ~20% error in quantification, as permanent gases besides H2 exhibit calibration slopes within 20% of one another) in Ar. Using the ratio between the m/z=2 signal (for H_2) and m/z=36 signal (for Ar) along with our calibration line, we can calculate the mole fraction of H_2 in each gas sample. The analogous process is done for CO_2 (using m/z=44 instead of m/z=2) and C_2H_2 (using the m/z=26 signal with the O_2 calibration slope). An example calibration line for H_2 in Ar is shown in Figure 3.6.

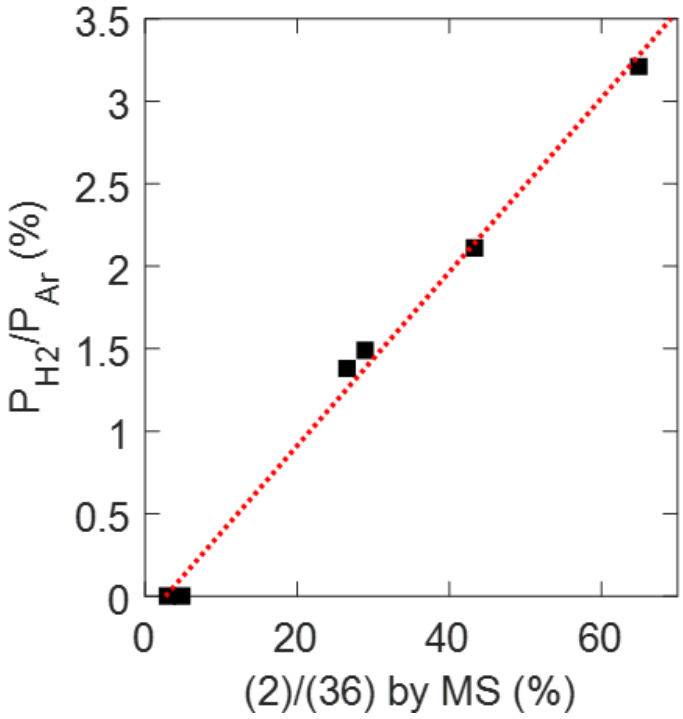

Figure 3.6: MST calibration line. Example calibration data used to quantify the mole ratio of H_2 in an Ar carrier gas. Each point was obtained by supplying a gas of known H_2 and Ar partial pressure (y-axis) to the MS, where the ion currents at m/z ratios of 2 and 36 are recorded. The r^2 for the calibration line is 0.994.

We then use the Ideal Gas Law to calculate the total moles of H_2, CO_2, and C_2H_2 in each gas sample. Example H_2 titration curves for the electrode samples in Figure 3.2 are overlaid in Figure 3.7. After allowing the signal to fully attenuate, we calculate the total gas evolved from the integration of each curve. Again, the analogous process is done for CO_2 using the m/z=44 signal and C_2H_2 using the m/z=26 signal.

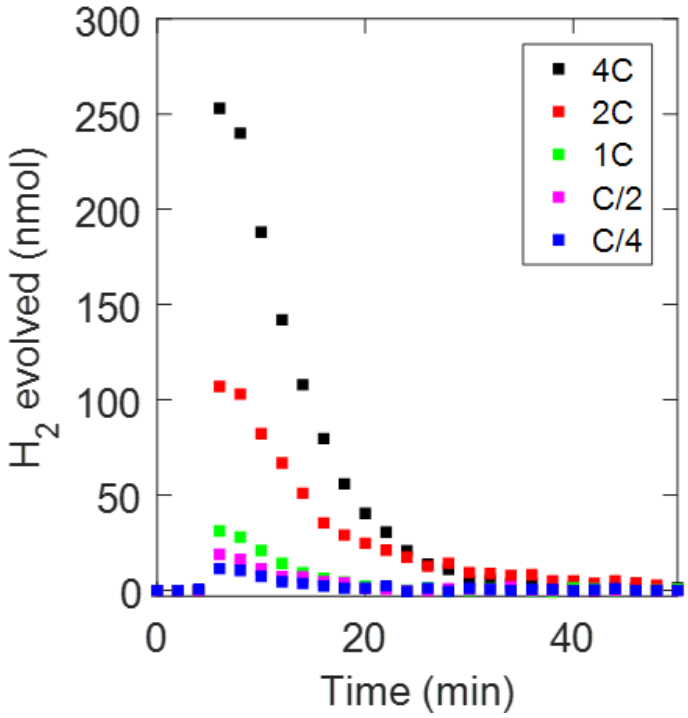

Figure 3.7: Overlaid MST H_2 gas evolution signatures from C-rate sweep. H_2 gas evolution during titration for electrodes in Figure 3.2. Acid was injected before the fourth data point in each case.

3.9.3 MST Dead Li Detection Limit

We claim a detection limit of 20 nmol dead Li with MST in Section 3.2, which is based upon the expected minimum H_2 signal that we can quantify upon titration (noting that one mole H_2 corresponds to 2 moles of dead Li). Figure 3.8 shows how we arrived at this conclusion. The lowest amount of dead Li measured with MST in Chapter 3 was 105 nmol Li, which is well above the limit of detection based on the ratio of signal to noise. Given the typical ion current response to H_2, we expect that an evolution of ~5 nmol H_2 (~10 nmol of dead Li) would still be perceptible, although not quantifiable. 10 nmol of H_2 (20 nmol dead Li) is clearly distinguishable from baseline noise, as scaling the 105 nmol dead Li data by 1/5 shows (Figure 3.8).

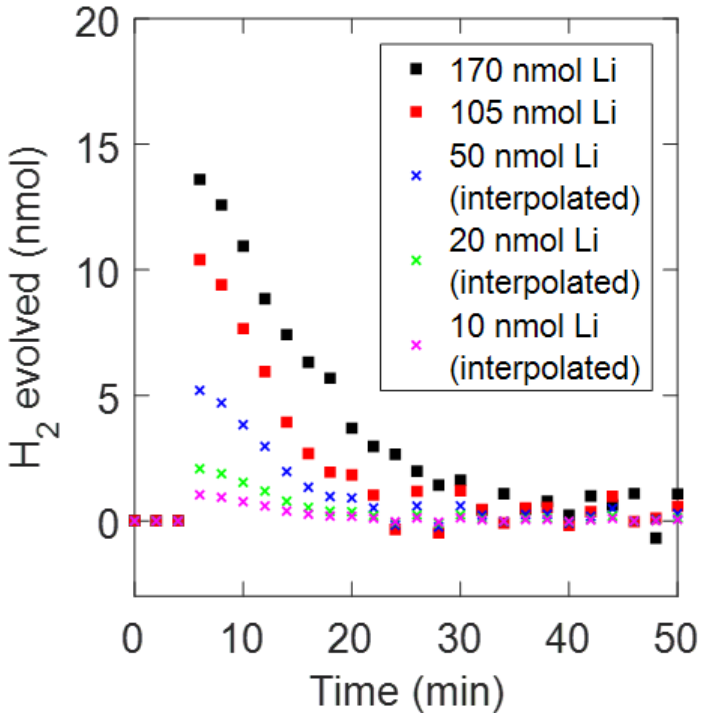

Figure 3.8: Dead Li detection limit of MST. H_2 gas evolution during titration for real electrode samples (squares) and interpolated data ('x' markers). Interpolation was done by scaling the 105 nmol Li experimental data by a factor of two (for 50 nmol Li), a factor of five (for 20 nmol Li), and a factor of ten (for 10 nmol Li). Acid was injected before the fourth data point in each case.

3.9.4 Equivalent Dead Li Capacity

Under our definition of dead Li, which includes only electronically isolated Li and Li_xC_6, we can calculate an equivalent capacity of dead Li by assuming that plated Li is formed via a 1 electron/Li process and Li_xC_6 is formed via a x electron/Li_xC_6 process, i.e., 1 mole electron per mole dead Li. This calculation is shown in Equation 3.9.1, where Q_{Li} is the dead Li equivalent capacity and n_{Li} is the number of moles of dead Li measured via H_2 evolution upon titration.

$$Q_{Li} = n_{Li}(\frac{1\ mole\ e^-}{1\ mole\ Li})(\frac{96485\ C}{1\ mole\ e^-})(\frac{mAh}{3.6\ C}) \tag{3.9.1}$$

3.9.5 Capacity Loss Breakdown from Figures 3.2 and 3.5

Data from Figures 3.2 and 3.5 can be recast as individual contributions to the total irreversible capacity loss during fast charge cycling after formation. The results are shown in Figures 3.9 (for Figure 3.2 data) and 3.10 (for Figure 3.5 data) below. We note that in both

Figures 3.9 and 3.10, the solid carbonate and Li_2C_2 contributions to the total irreversible capacity are calculated based on the increase in the amount of carbonate and Li_2C_2 above the baseline values observed after formation cycling (see Section 3.9.7). Additionally, Figure 3.10 shows results for unrinsed samples (denoted by a '*' in the x-axis label) that had undergone five and ten 4C charge cycles. The capacity loss due to carbonate formation on the unrinsed samples was assumed to be equivalent to the rinsed counterparts (i.e., the five cycle unrinsed sample carbonate capacity was assumed to be equivalent to the five cycle rinsed sample carbonate capacity), as the CO_2 evolved upon titration for the unrinsed samples was affected by residual electrolyte (solid ethylene carbonate evolves CO_2).

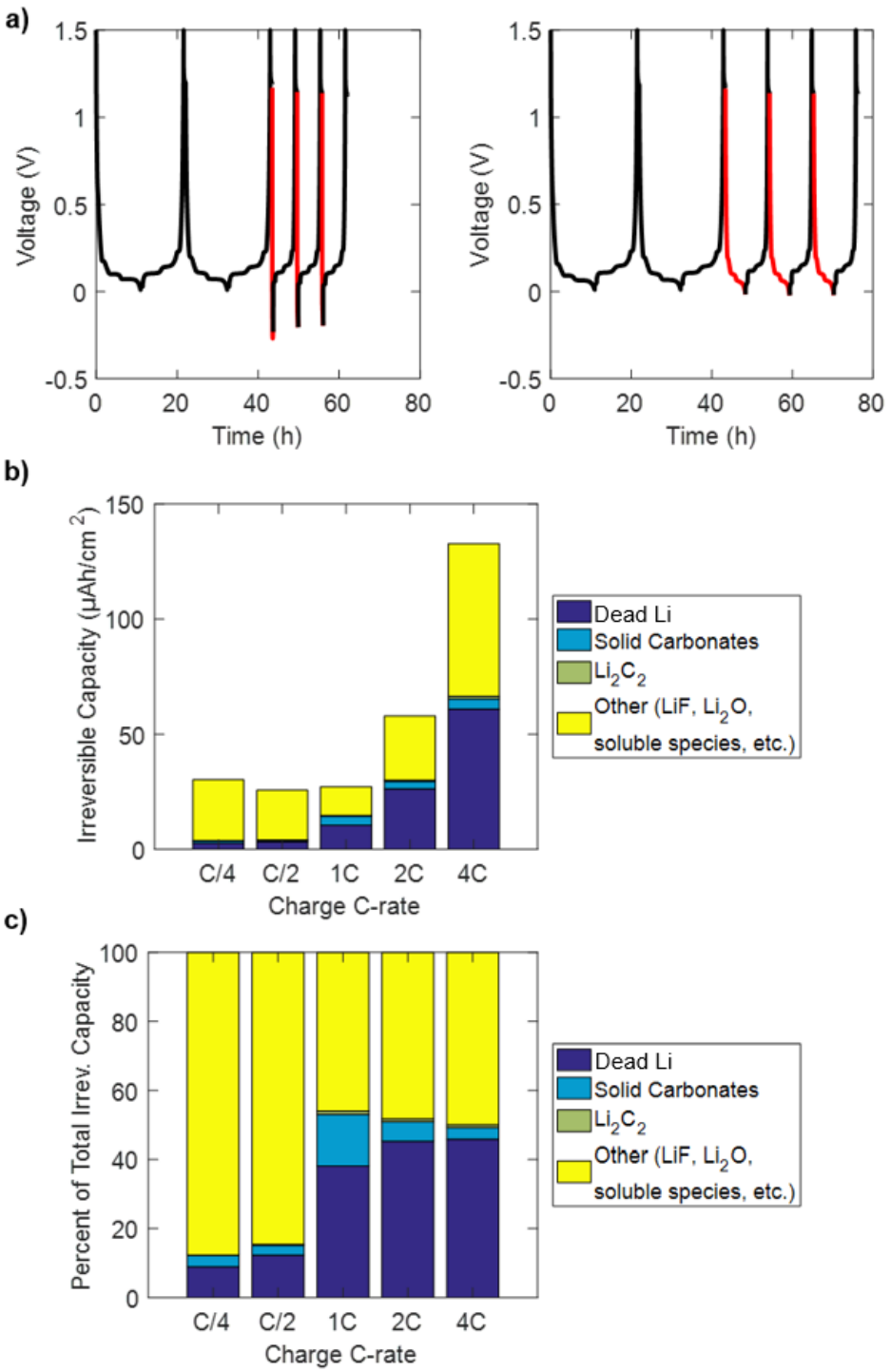

Figure 3.9: Capacity breakdown for Figure 3.2. **a.** Examples of cell cycling procedure: two C/10 formation cycles (0.010-1.5 V) followed by three cycles of varying charge rate (shown in red) and C/4 discharge to 1.5 V with 30-minute OCV period between each charge/discharge. Left: C/4 charge rate. Right: 4C charge rate. **b.** Total contributions of dead Li, solid carbonates, Li_2C_2, and other species to the observed irreversible capacity after three cycles of varying charge C-rate. **c.** Percent contributions of dead Li, solid carbonates, Li_2C_2, and other species to the observed irreversible capacity from panel b.

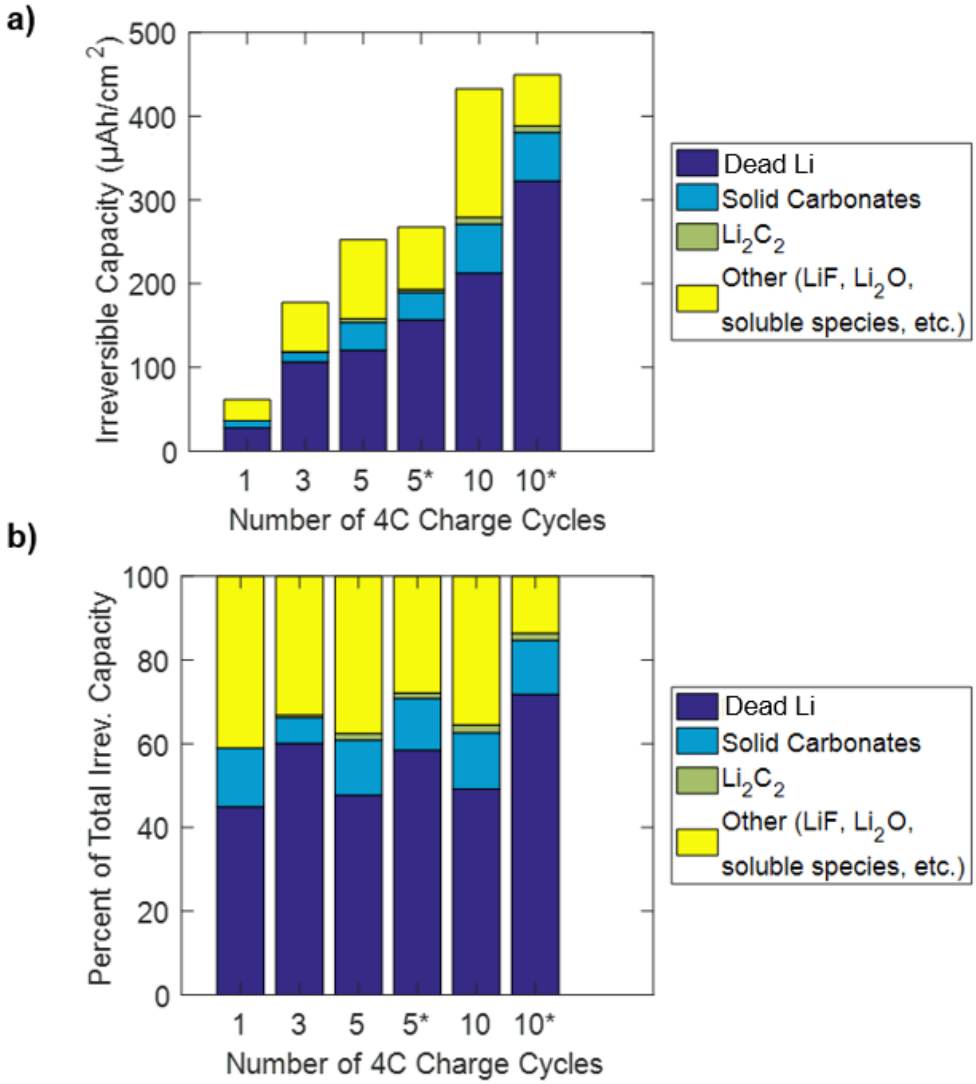

Figure 3.10: Capacity breakdown for Figure 3.5. **a.** Total contributions of dead Li, solid carbonates, Li_2C_2, and other species to the observed irreversible capacity after varying numbers of 4C charge, C/4 discharge cycles. '*' in the x-axis label denotes an unrinsed sample. Lost capacity due to solid carbonates for the unrinsed samples were assumed to be equivalent to the rinsed counterparts. **b.** Percent contributions of dead Li, solid carbonates, Li_2C_2, and other species to the observed irreversible capacity from panel a.

3.9.6 Rinsing Effect on Dead Li Measurement in Figure 3.2

We see in Figure 3.2b that Q_{offset} (defined in Equation 3.5.1) is steady at a baseline value of 20-30 µAh/cm^2 for C-rates of 2C and below but increases slightly to ~75 µAh/cm^2 for the 4C charge rate. One could propose that this increase in offset capacity is due to dead Li being rinsed off the electrode surface prior to titration. To test this, we titrated an unrinsed electrode that had undergone the standard formation cycles followed by three cycles of 4C charge, C/4 discharge as in Figure 3.2. The results of the unrinsed electrode titration (Figure 3.11a) and the calculated offset capacity (Figure 3.11b) are shown overlaid upon data from

Figures 3.2a and 3.2b, respectively. We see that both the measured dead Li and offset capacity are within error of the rinsed counterparts, indicating that rinsing does not have a significant effect on the measured dead Li for three cycles and below of 4C charge, C/4 discharge. However, we see in Figure 3.5 that rinsing does have a significant impact for five or more cycles of 4C charge, C/4 discharge.

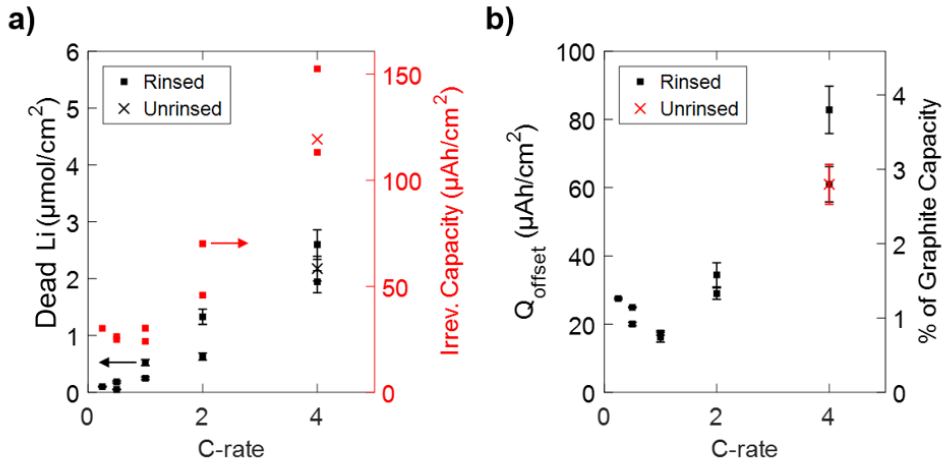

Figure 3.11: Rinsing effect on Figure 3.2 measurements. **a.** Dead Li (black) and cumulative irreversible capacity (red) measured on unrinsed electrode ('x' markers) overlaid with rinsed electrode data (squares) from Figure 3.2a. **b.** Q_{offset} (defined in Equation 3.5.1 of Chapter 3) for unrinsed electrode ('x' marker) overlaid with rinsed electrode data (squares) from Figure 3.2b.

3.9.7 Equivalent Solid Carbonate and Li_2C_2 Capacities

In Figure 3.2c, we notice that the electrodes that underwent three 4C charge, C/4 discharge cycles after formation evolved ~1 µmol/cm^2 CO_2 upon titration, while the baseline electrode that only underwent two formation cycles evolved ~0.9 µmol/cm^2 CO_2, meaning there was a ~100 nmol/cm^2 CO_2 increase as a result of the three fast charge cycles after formation (although we note that 100 nmol/cm^2 is just within the error of the measurement). Assuming this CO_2 all comes from LiEMC, which was recently reported to be the most abundant species in the graphite SEI when using a similar electrolyte,[48] we can convert the additional CO_2 (n_{CO2}) evolved after the three cycles to an equivalent irreversible capacity (IC_{CO2}).

$$IC_{CO2} = n_{CO2}\left(\frac{1\ mole\ LiEMC}{1\ mole\ CO_2}\right)\left(\frac{2\ mole\ e^-}{1\ mole\ LiEMC}\right)\left(\frac{96485\ C}{1\ mole\ e^-}\right)\left(\frac{mAh}{3.6\ C}\right) \tag{3.9.2}$$

We assume two electrons are used to form one LiEMC, as recent reports propose LiEDC is formed first via a two-electron process, and this LiEDC chemically reacts to form LiEMC.[48] Using 100 nmol/cm^2 for n_{CO2}, we calculate IC_{CO2}~5 µAh/cm^2, which is not nearly enough to account for all of the offset capacity in Figure 3.2b. Thus, we suspect the remainder of

the offset capacity is due to a non-carbonate-containing SEI component (e.g., LiF) or the formation of electrolyte soluble solvent degradation products.

$$IC_{Li2C2} = n_{Li2C2}(\frac{2\ mole\ Li}{1\ mole\ Li_2C_2})(\frac{1\ mole\ e^-}{1\ mole\ Li})(\frac{96485\ C}{1\ mole\ e^-})(\frac{mAh}{3.6\ C}) \tag{3.9.3}$$

The equivalent capacity of Li_2C_2 (IC_{Li2C2}) was calculated based on the amount of Li contained in the total moles of Li_2C_2 (n_{Li2C2}) formed.

We note that this equivalent capacity of Li_2C_2 does not necessarily represent the total amount of plated Li that may have reacted to form Li_2C_2, as the stoichiometry of the Li_2C_2-forming reaction may indicate that more than two moles of plated Li must react to form one mole of Li_2C_2. As in the example solid carbonate capacity calculation above, the Li_2C_2 equivalent capacity used in Section 3.9.5 is based on the increase in the amount of Li_2C_2 above the baseline amount observed after formation cycling (~31 nmol Li_2C_2/cm^2).

3.9.8 Dead Li in Separator

Dead Li that dislodges from the graphite electrode and entrains in the separator is another possible source of irreversible capacity that would not normally be accounted for by our titration technique. Since the counter electrode is Li metal, simply removing the separator from the cell and titrating it may yield inconsistent results because Li from the Li metal counter electrode could become entrained in the separator as well. To estimate the contribution of Li dislodged from the graphite and entrained in the separator, we constructed a cell with two Whatman QMA separators and titrated (without rinsing) both the graphite electrode and the separator adjacent to it (not the separator adjacent to the Li metal counter electrode). We tried this for a cell that underwent five 4C charge, C/4 discharge CC cycles after formation as well as ten CC cycles after formation. The ten-cycle electrode had substantial plating, such that the separator was adhered to the electrode, making analysis difficult. The five-cycle electrode titration results are plotted in Figure 3.12, which is overlaid with the data from Figure 3.5a. We note that, due to the thick double separator, the cumulative irreversible capacity during the five cycles is almost twice as large as the one separator, five cycle counterparts. We measure ~9 µmol/cm^2 dead Li on the electrode alone and ~2 µmol/cm^2 dead Li in the separator for a combined ~11 µmol/cm^2 dead Li. This still does not account for all of the lost capacity during fast cycling, which would be ~17 µmol/cm^2 dead Li equivalent. This shows that dead Li entrainment in the separator cannot be ignored when a large amount of Li has plated, but it is not at first estimation a major contributor to capacity loss.

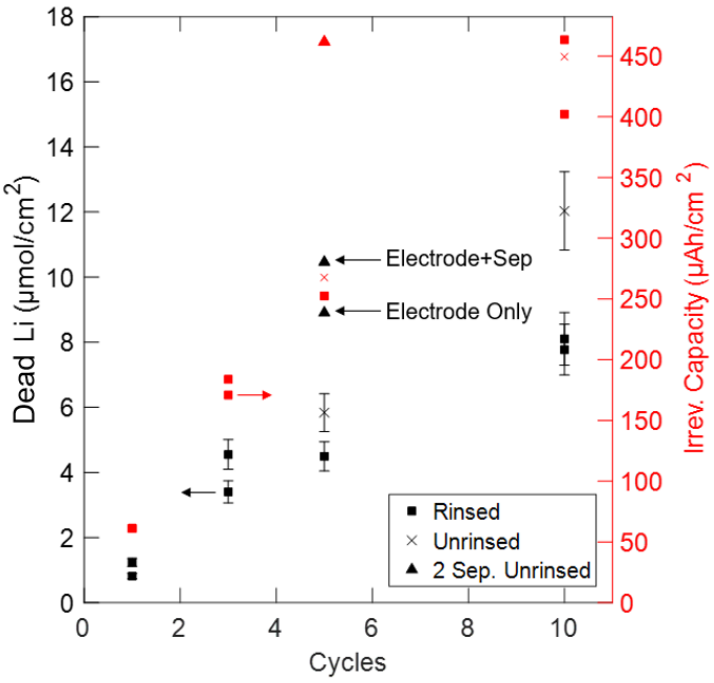

Figure 3.12: Quantification of dead Li entrained in separator. Two separator (triangles) titration results (black) and cumulative irreversible capacity (red) during 4C charge, C/4 discharge cycling overlaid with data from Figure 3.5a.

3.9.9 Effect of Slower Discharge Rate

Using a C/10 discharge instead of C/4 discharge after one 4C charge to 372 mAh/g yielded the same amount of dead Li and CO_2 upon titration within error. Figure 3.13 below overlays Figures 3b and 3c (which both contain C/4 discharge data) with the C/10 discharge result. This indicates that the C/4 discharge is a sufficiently slow rate to remove all reversible Li from the graphite.

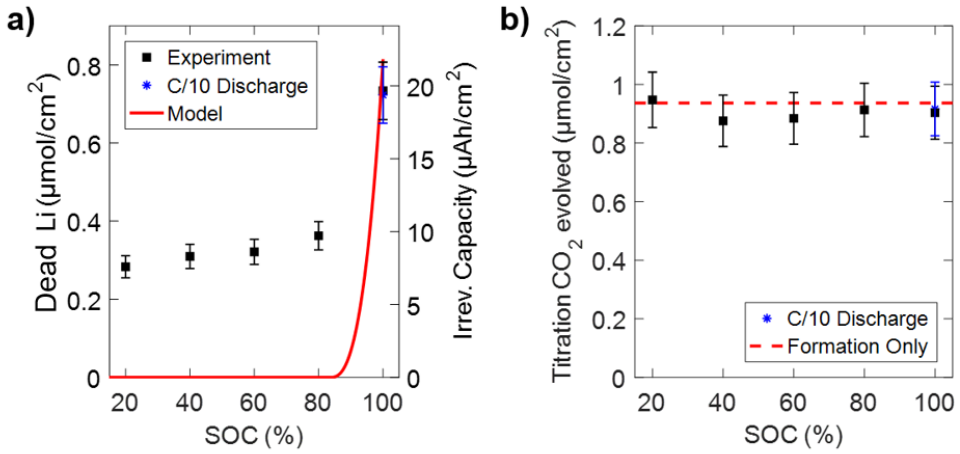

Figure 3.13: Effect of discharge rate on measured dead Li and solid carbonates. **a.** Dead Li titration result for C/10 discharge case (*, blue) overlaid with Figure 3.4b. **b.** CO_2 evolved upon titration for C/10 discharge case (*, blue) overlaid with Figure 3.4c.

3.9.10 Effect of OCV Rest Period

We also explored the impact of open circuit voltage (OCV) rest time between a 4C charge and C/4 discharge on the measured amount of dead Li. Previous work[7] suggests that a long OCV period (>15 minutes) would allow sufficient time for plated Li in intimate contact with graphite to chemically insert into graphite that is not fully lithiated, leaving behind a layer of electronically isolated dead Li. We hypothesized that by decreasing the OCV time, we could strip the plated Li before it had time to chemically insert, resulting in less dead Li. However, we found that the effect of OCV time was only modest, with an average difference of only ~0.5 µmol/cm^2 dead Li between the cells cycled with 0 and 30-minute OCV (Figure 3.14b), corresponding to an increase in stripping efficiency to 75% for the 0-minute OCV case compared to 65% for the 30-minute OCV case. The effect of decreased OCV time may be more pronounced when coupled with higher discharge rates, which would lower the possibility that plated Li continues to chemically insert into graphite during discharge, but we did not explore the effect of discharge rate in this work. We also note that the amount of carbonate-containing SEI remains the same within error regardless of OCV time (Figure 3.14c), but the amount of Li_2C_2 increases with increasing OCV time (Figure 3.14d). This implies that Li_2C_2 forms via a chemical reaction with plated Li, as it is formed during the rest period when plated Li is present and no current is being passed.

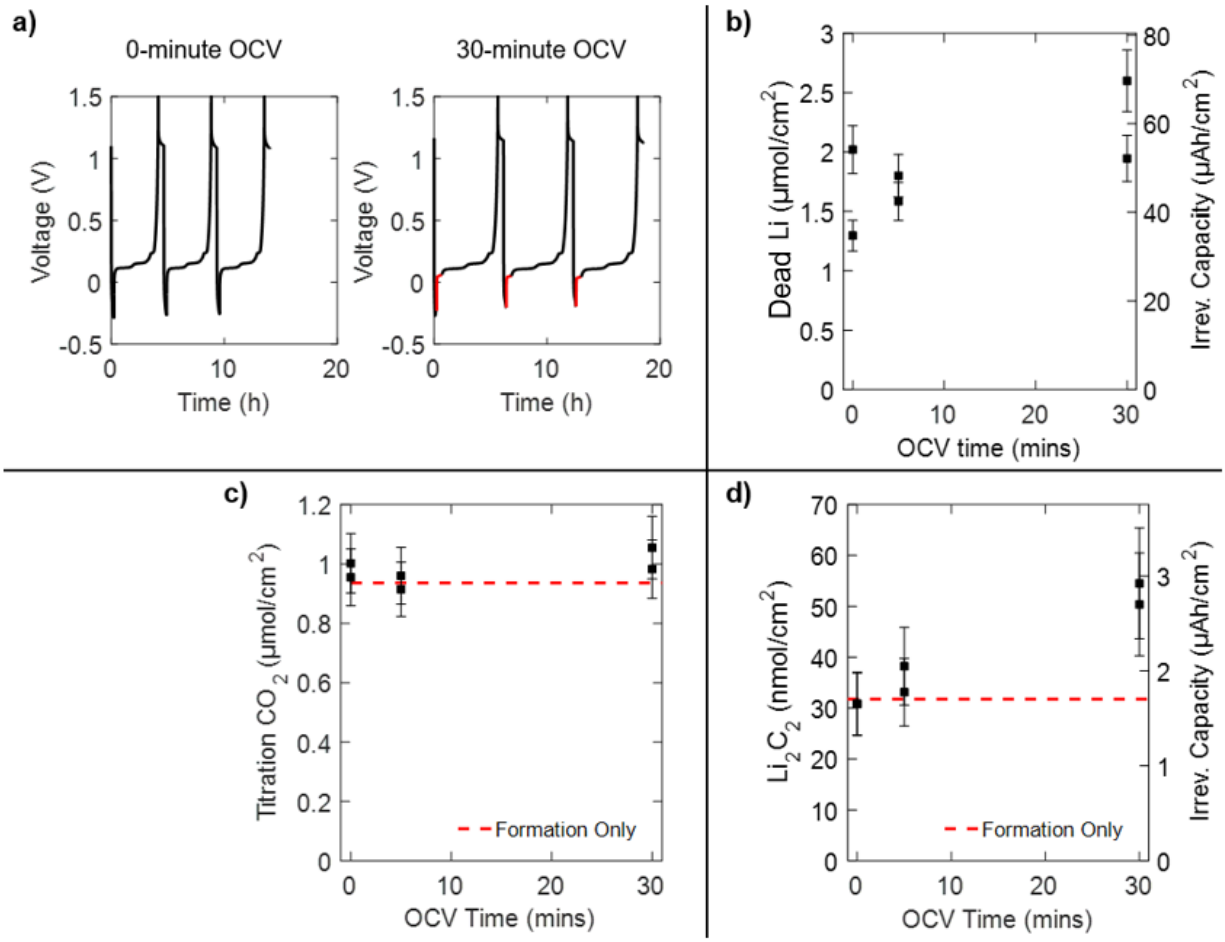

Figure 3.14: Effect of OCV rest period on titration results. **a.** Examples of cell cycling procedure (two formation cycles not shown): three 4C charge, C/4 discharge cycles with 0-minute and 30-minute OCV periods (shown in red) after each charge. OCV period after discharge remained at 30 minutes. **b.** Dead Li measured via titration as a function of OCV time after charge. **c.** CO_2 evolved upon titration as a function of OCV time between charge and discharge. **d.** Li_2C_2 measured via titration as a function of OCV time between charge and discharge.

3.9.11 Model Description

A previously reported macro-homogeneous half-cell model is modified to consider lithium plating via the following reaction:

$$\mathrm{Li^+(electrolyte) + e^-(anode) \longleftrightarrow \beta Li^{rev}(anode) + (1-\beta)Li^{irr}(anode)} \tag{3.9.4}$$

The text within the parentheses denotes the phase associated with the species. The lithium plating model builds upon the reaction framework proposed by Ren et al.[52] The symbol β represents the fraction of the lithium plating that can be reversibly stripped. For the

proposed model, β is assumed to be constant. The plating current associated with the above reaction is calculated with the following Butler-Volmer equation:

$$i_{Li} = i_{0,p} a_s (exp(\frac{\alpha_a F(\phi_s - \phi_e)}{RT}) - exp(\frac{-\alpha_c F(\phi_s - \phi_e)}{RT}))\ when\ (\phi_s - \phi_e) < 0 \tag{3.9.5}$$

where R, T, and F represent the universal gas constant, cell temperature, and Faraday's constant. Note the convention used is that cathodic current (plating) is negative and anodic current (stripping) is positive. The specific surface area is calculated using the standard assumption of ideal disconnected spheres,

$$a_s = \frac{3\epsilon_s}{r_p} \tag{3.9.6}$$

The cathodic plating occurs when the solid phase potential ϕ_s is below that of the surrounding electrolyte ϕ_e. An SEI film resistance was not considered in the model. The cathodic and anodic symmetry factors for lithium plating are taken to be α_a=0.3 and α_c=0.7.[57] The exchange current density for lithium plating, $i_{0,p}$, is found by fitting to gas titration measurements for moles of plated lithium and electrochemical voltage signatures as seen in Figure 3.3. Anodic stripping is modeled with a similar Butler-Volmer equation, which is modified such that the rate of stripping goes to zero when all reversible lithium is consumed:

$$i_{Li} = i_{0,p} a_s (exp(\frac{\alpha_a F(\phi_s - \phi_e)}{RT}) - exp(\frac{-\alpha_c F(\phi_s - \phi_e)}{RT}))\frac{c_{Li^{rev}}}{c_{Li^{rev}} + \gamma}\ when\ (\phi_s - \phi_e) > 0 \tag{3.9.7}$$

where γ is set sufficiently low such that the above fraction goes to zero when the concentration of reversible plated lithium, $c_{Li^{rev}}$, is very low and 1 when for any significant concentration. A value of γ=0.01 is found to meet these criteria. The change in concentration of reversible and irreversible plated lithium are calculated as follows when i_{Li}<0 and lithium is plating:

$$\frac{\partial c_{Li^{rev}}}{\partial t} = -\beta i_L \tag{3.9.8}$$

$$\frac{\partial c_{Li^{irr}}}{\partial t} = -(1 - \beta) i_L \tag{3.9.9}$$

Conversely, when i_{Li}>0 and lithium is being stripped:

$$\frac{\partial c_{Li^{rev}}}{\partial t} = -i_L \tag{3.9.10}$$

$$\frac{\partial c_{Li^{irr}}}{\partial t} = 0 \tag{3.9.11}$$

The total number of moles of plated lithium is found by integrating the concentration across the anode thickness and multiplying by cell area. The typical conservation equations for solid phase potential, electrolyte potential, and electrolyte concentration are modified to consider Faradaic current from both intercalation chemistry and lithium plating/stripping. Lithium ion fluxes from local changes in transference number are also considered in the model. The model assumes isothermal operation due to the small cell area and relatively large thermal mass of Swagelok cell. The effect of deposited lithium on intercalation kinetics is neglected, but will be the subject of investigation moving forward.

3.9.12 Model Parameters

The half-cell model uses electrochemical parameters determined for graphite anodes composed of Superior Graphite 1506T active particles. Model inputs for electrolyte transport properties are taken from previously reported Gen 2 electrolyte properties at 30 °C.[51] Tables 3.1 and 3.2 summarize model inputs. The porosity of compressed Whatman glass separator is obtained by measuring a compressed thickness, weight of separator, and assuming a density of 2.25 g/cm^3 for borosilicate. The modeled cell area 0.96 cm^2 is slightly larger than that of the electrode punch (0.95 cm^2) to match experimental results that measurable amounts of lithium plating occur only at rates above C/2. The Bruggeman exponent for graphite is based on measuring the tortuosity of 1506T graphite electrodes via microstructure reconstruction and fitting to electrochemical rate data.[31]

Table 3.1: Electrochemical model parameter inputs for half-cell model. Concentrations for electrolyte C_e and intercalated lithium C_s are evaluated in kmol/m^3.

Property	Graphite Electrode	Separator	Lithium
Thickness (µm)	47	200	N/A
Porosity (%)	37.4	70	N/A
Particle Radius, r_p (µm)	4	N/A	N/A
Bruggeman Exponent	2.1	1.5	N/A
Exchange current density, i_0 (A/m^2)	$0.4(C_e)^{0.5}(C_s)^{0.5}(C_s - C_s^{max})^{0.5}$	N/A	100
Solid-state Diffusion Coefficient, D_s (m^2/s)	3x10^{-14}	N/A	N/A
Maximum Intercalated Lithium Concentration, C_s^{max} (kmol/m^3)	31.0	N/A	N/A

3.9.13 Model Results

Figure 3.15 illustrates model results for half-cell voltage during a cycle with 4C lithiation. The entire cycle consists of a 900 second 4C lithiation, 30-minute rest, and C/4 delithiation.

Table 3.2: Electrolyte transport properties for Gen 2 electrolyte at 30 °C. Concentrations for electrolyte C_e are evaluated in kmol/m^3.

Electrolyte Property	Expression
Ionic conductivity, K (S/m)	$\frac{C_e}{10}(4.9464 - 1.8143C_e + 0.07968C_e^2 + 0.01947C_e^3)^2$
Diffusion Coefficient, D_s (m^2/s)	$0.0001\times10^{(-4.8321 - \frac{21.063}{T-62.147-12.195C_e} - 0.3852C_e)}$
Transference Number, $t_{Li+}{}^o$	$-0.002395C_e^4 + 0.024476C_e^3 - 0.077134C_e^2 + 0.074373C_e + 0.43031$
Activity Coefficient, $1 + \frac{dlnf_{+-}}{dlnC_e}$	$0.5556 + 1.85997C_e - 0.4917C_e^2 + 1.0474C_e^3 - 0.1376\ C_e^4$

The model-predicted voltage matches relatively well with that experimentally measured, but there are some slight discrepancies related to representing graphite as an intercalation material instead of a multi-phase material, constant solid-state Li diffusion coefficient, and treating the lithium electrode as ideal. Lithium plating is predicted to occur at 765 seconds into 4C charge, corresponding to an average intercalation fraction of 0.85 (as seen in Figure 3.4b). Plating is not predicted until the cell voltage is -155 mV due to voltage loss at the lithium electrode and across the thick separator. The reported lithium plating model will be refined in future work to incorporate geometric effects such as dead Li buildup, SEI growth, and varying stripping efficiencies depending on amount of plated Li and rest time.

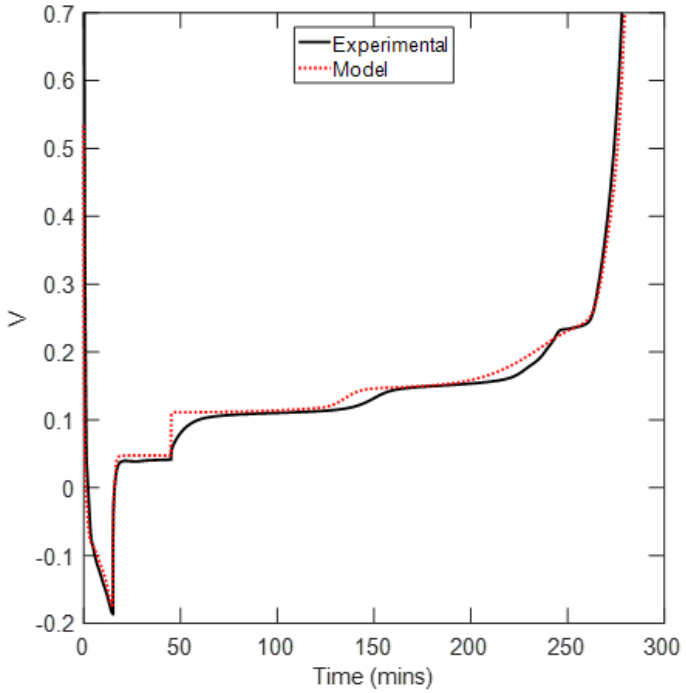

Figure 3.15: Comparison of modeled and experimental voltage profile for lithium-graphite half-cell during 4C lithiation, 30-minute rest, and C/4 delithiation. The plating current density was set to 10 A/m^2 and the stripping efficiency was set to 65%.

Chapter 4

Effect of Lithium Salt Concentration on Graphite Interphasial Chemistry and Implications for Fast Charging

4.1 Abstract

The solid-electrolyte interphase (SEI) formed on graphite electrodes enables the remarkable capacity retention of lithium-ion batteries, yet a comprehensive quantitative description of the SEI remains elusive. Using a combination of differential electrochemical mass spectrometry (DEMS) and mass spectrometry titration (MST), we quantify graphite SEI components formed under electrolytes of varying salt concentrations. We demonstrate that higher salt concentration electrolytes (up to 2.0 M $LiPF_6$) result in an overall thinner SEI that is rich in lithium fluoride with less solid carbonates deposited compared to lower concentration electrolytes. We also find that higher concentration electrolytes reduce the amount of dead lithium metal and inhibit the growth of a thick solid carbonate layer during prolonged fast charging. Owing to the advantages imparted by a thinner, fluoride-rich SEI, the onset state of charge for lithium plating for the 2.0 M electrolyte is significantly later than that predicted by a standard electrochemical model, suggesting that future electrochemical models should be refined to include explicit SEI effects in addition to electrolyte transport, solid-state diffusion, and graphite lithiation kinetics.[iii]

4.2 Introduction

Battery electric vehicles (EVs), combined with renewable energy generation, present a generational opportunity to replace internal combustion engine vehicles and decarbonize our transportation infrastructure. However, one key challenge hindering widespread adoption of EVs is the slow charge time of LIBs, which require ~40 minutes for a full recharge compared

[iii]This chapter is largely adapted from work in preparation: E.J. McShane, P.J. Weddle, H.K. Bergstrom, D.E. Brown, A.M. Colclasure, and B.D. McCloskey. Effect of Lithium Salt Concentration on Anodic Interphasial Chemistry and Implications for Fast Charging. **in prep**.

to the ~5 minutes required to fill a gas tank.[28] Thus, understanding bottlenecks to and generating solutions for fast charging remains a crucial area of research.

Fast charging of LIBs is challenging for many reasons spanning several length scales. At the continuum scale, lithium ions must transport through the separator and the pores of the graphite anode, all the while maintaining sufficient Li^+ concentration throughout the depth of the anode to ensure uniform lithiation of the whole porous electrode.[6;31;61] At the micron scale, lithium must diffuse through the solid graphite host material to uniformly lithiate each particle. At the submicron scale, the interfacial graphite lithiation reaction must occur, but it is affected by not only the kinetics of the lithiation process, but also by desolvation of Li^+ and by the transport of Li^+ through the solid-electrolyte interphase (SEI). A limitation at any step in this process will result in high required overpotentials, which can lead to lithium plating and subsequent precipitous capacity loss.[2]

There have been numerous measurements of bulk electrolyte transport properties and solid state lithium diffusion coefficients in graphite to describe the aforementioned continuum and micron scale effects.[21;30;31;62] However, understanding sub-micron scale effects (such as transport through the SEI) has proven challenging, particularly because a full quantitative description of the SEI composition remains largely elusive.[1] In a similar vein, Li plating behavior on graphite has often been explored qualitatively,[7;63;64] and many methods have been developed for binary detection of plated Li in operando,[9] but few have developed methods to directly quantify plated Li.[2;32] In this work, we develop a quantitative understanding of these submicron SEI and Li plating phenomena through the use of operando differential electrochemical mass spectrometry (DEMS) and ex situ mass spectrometry titration (MST) measurements, as will be described in Sections 4.3.2 and 4.3.3.

Noting that both the electrolyte solvent and the Li^+ counteranion are known to degrade to form the SEI,[55] varying the salt concentration in an electrolyte will ultimately impact the SEI composition. We therefore studied electrolytes with a range of salt concentrations, from 0.35 M $LiPF_6$ to 2.0 M $LiPF_6$, always in a solvent blend of 3:7w ethylene carbonate (EC) to ethyl methyl carbonate (EMC). We quantified two main classes of graphite SEI components formed under these electrolyte compositions: the 'inner-SEI' (predominantly LiF, but also including LiOH and Li_2O) and the 'outer-SEI' (solid carbonates including lithium ethylene dicarbonate (LiEDC) and lithium ethylene monocarbonate (LiEMC)) through a combination of DEMS and MST. As anticipated, we found that varying the electrolyte salt concentration significantly altered the formed graphite SEI composition, with higher salt concentration electrolytes resulting in a more LiF-rich and solid carbonate-poor SEI compared to lower concentration electrolytes. Electrolyte aging was also found to increase the amount of HF in solution, resulting in a thicker inner-SEI. The SEI composition additionally affected fast charge behavior, with the 2.0 M electrolyte showing a delayed onset for Li plating compared to that predicted by a standard electrochemical model. With this in mind, we highlight the need for more advanced electrochemical models with explicit SEI effects. Finally, the higher concentration electrolytes resulted in less dead Li (defined as plated Li and lithiated graphite which are not electrochemically active) and less solid carbonate deposition during prolonged fast charge cycling. Thus, we propose highly concentrated electrolytes as a promising path

towards enabling fast charging LIBs with minimal capacity fade over the course of many fast charge cycles.

4.3 Methods

4.3.1 Lithium-Graphite Coin Cells

CR2032 Li-graphite coin cells (Pred Materials parts) were constructed using 15 mm diameter graphite electrodes (2.84 mAh/cm^2, 91.83 wt% Superior Graphite SLC1506T, 2 wt% Timcal C45 carbon, 6 wt% Kureha 9300 PVDF binder, 0.17 wt% oxalic acid, 9.38 mg/cm2, 38.2% porosity, 70 µm coating thickness) supplied by the Cell Analysis, Modeling, and Prototyping (CAMP) facility at Argonne National Laboratory. A 15 mm diameter Li metal counter electrode (750 µm thickness, from MTI), a 20.6 mm diameter Celgard 2500, and 30 µL of 3:7w EC:EMC with either 0.35 M, 0.70 M, 1.2 M, or 2.0 M $LiPF_6$ concentration electrolyte were also used in each coin cell. A decrimper from Pred Materials was used to decrimp each cell and extract the graphite electrode before titration was performed.

4.3.2 Differential Electrochemical Mass Spectrometry (DEMS)

Differential electrochemical mass spectrometry (DEMS) was performed using a custom built instrument and custom cells that have been described in depth elsewhere.[65] The DEMS cells were assembled using the aforementioned graphite electrodes of 12 mm diameter, a Li metal counter electrode of 11 mm diameter, and a Whatman QMA glass fiber separator of 12.5 mm diameter with 60 µL of electrolyte. Electrolytes of 0.35 M, 0.70 M, 1.2 M, and 2.0 M $LiPF_6$ concentration were cycled with a single C/10 (based on 350 mAh/g reversible graphite capacity) formation cycle with lower and upper cutoff potentials of 0.010 V and 1.5 V. The evolution rates of three gases (H_2, C_2H_4, and CO_2) were measured and quantified by comparison to calibration curves generated using various analyte gas/argon mixtures. Besides H_2, C_2H_4, and CO_2, no other gases were observed in measurable quantities.

4.3.3 Mass Spectrometry Titration (MST)

Mass spectrometry titration (MST) was used to quantify anodic interphasial species after graphite electrodes had been cycled. A detailed description of the technique can be found in Chapter 3. Electrodes from both coin cells and DEMS cells were extracted from cells and titrated. For the 15 mm diameter graphite electrodes extracted from coin cells, 300 µL of dimethyl carbonate (DMC) was used to rinse the electrode three times, each time swirling gently for one minute and discarding the rinse solution. The electrode was then dried in the glovebox antechamber for 15 minutes and stored in an airtight vial prior to titration. The analogous process was used for graphite electrodes extracted from DEMS cells, but

200 (instead of 300) µL DMC was used to rinse the electrode three times to account for the difference in electrode size. The rinsing procedure and solvent selection were used to eliminate the loss of any solid SEI components that formed. Importantly, previous reports have proven that SEI components are almost completely nonreactive with and insoluble in DMC, making it an ideal solvent choice to remove residual electrolyte while keeping the SEI intact.[48]

After proper rinsing, the electrode sample was placed in a titration vessel, the vessel was connected to an in-line mass spectrometer (all the while remaining airfree), and 3.5 M H_2SO_4 was injected into the vessel. The acid reacted with SEI species, including dead Li, solid carbonates, and Li_2C_2, present on the electrode to evolve H_2, CO_2, and C_2H_2 gas, respectively, according to Reactions 3.3.1-3.3.6 shown in Chapter 3.

With appropriate calibration of each gas as described previously,[2] the amount of gas and therefore the amount of each SEI species was quantified. However, three important points should be addressed:

1. While dead lithiated graphite remaining in the electrode after cycling resulted in H_2 evolution upon titration, the amount of dead lithiated graphite (typically ~300 nmol/cm^2) in relation to dead Li metal for any electrode with appreciable plating was negligible. We therefore treat any dead Li above the baseline amount as dead Li metal.

2. We refer to the class of LiEDC, LiEMC, and Li_2CO_3 as 'solid carbonates,' with the caveat that one mole of LiEDC is comprised of two moles of solid carbonates, as there are two carbonate groups that would result in two moles of CO_2 evolved upon exposure to acid.

3. The amount of Li_2C_2 is in general small compared to the amount of dead Li and solid carbonates, and Li_2C_2 is thought to form from the reduction of solid carbonates, either electrochemically or by reaction of solid carbonates with plated Li metal.[2] Further details on Li_2C_2 quantification can be found in Section 4.8.2.

4.3.4 Electrochemical Modeling

A previously developed macrohomogeneous electrochemical half-cell model[30;31;51] was combined with a Li plating/stripping model[52] to predict dead Li amounts during fast charge, as shown in Section 4.6.1. Electrochemical properties of the specific anodes with 1506T Superior graphite active material used in this study have been previously reported in the literature, and all electrolyte transport properties are strong functions of salt concentration.[30;31;51] Polynomial functions for electrolyte diffusivity, ionic conductivity, transference number, and activity coefficient have been previously fitted to transport predictions from the Advanced Electrolyte Model for $LiPF_6$ in 3:7w EC:EMC for salt concentrations between 0 and 4 M.[31;66] The exchange current density for lithium plating within the anode and at the counter lithium electrode were both set to 10 A/m^2, and the lithium plating/stripping

reversibility was set to 70%, all based on previous work.[2] The Celgard 2500 separator was 25 µm thick with 55% porosity and modeled with a tortuosity of 2 based on measurements from Landesfeind et al.[67] A detailed model description and a list of parameters are included in Section 4.8.4. The model did not consider changes to interfacial electrode/electrolyte properties (SEI) from forming half-cells with different electrolyte salt concentrations. The model was developed by collaborators at the National Renewable Energy Laboratory and summarized with their permission in comparison to our experimental results.

4.4 Chemical Origins of Gas Evolution

Figure 4.1a shows the formation cycle voltage profile for a DEMS cell (a Li metal electrode and porous graphite electrode with 1.2 M $LiPF_6$ electrolyte) cycled at C/10. The inset of Figure 4.1a reveals that H_2 begins to evolve slightly before C_2H_4, indicating that H_2 evolution is related to inner-SEI formation (as the products of this H_2 forming reaction will deposit on the graphite electrode first), while C_2H_4 is related to outer-SEI formation. CO_2 primarily evolves later in cycling, likely as a result of a chemical reaction involving LiEDC. We will discuss the evolution of each of these gases sequentially in subsequent sections.

4.4.1 Hydrogen Evolution

Hydrogen evolution can occur from the reduction of H_2O or HF at the lithium metal counter electrode or at the partially lithiated graphite electrode. However, the H_2 evolution peak observed in Figure 4.1a and b is entirely related to processes occurring at the graphite electrode, as no gas evolution occurs when stripping Li metal from the counter electrode.[68] To understand the chemical origin of H_2 during the graphite formation cycle, it is important to consider the effect of electrolyte calendar aging, which affects the speciation of components within the electrolyte. Trace water impurities (which are inevitably present in battery electrolytes) can react with both electrolyte salt and solvent species over the course of weeks to months, and the new species formed in solution change the DEMS gassing behavior.[47;69] For example, water reacts in the presence of $LiPF_6$ to form HF according to Reactions 4.4.1 and 4.4.2.

$$LiPF_6 \longrightarrow LiF + PF_5 \tag{4.4.1}$$

$$PF_5 + H_2O \longrightarrow POF_3 + 2\,HF \tag{4.4.2}$$

The molecular dissociation of $LiPF_6$ (Reaction 4.4.1) is reasonably sluggish in typical battery electrolytes, but the presence of water quickly consumes any PF_5 that forms, driving Reaction 4.4.1 further forward.[70] One study found that even after the intentional addition of 1000 ppm H_2O (typically battery electrolytes contain less than 100 ppm H_2O) to a 1.0 M $LiPF_6$ in 1:1v

EC to diethyl carbonate (DEC) electrolyte, ~65% conversion of $LiPF_6$ to HF occurred only after about one week.[69] This suggests that the calendar age of the electrolyte plays an important role in the speciation of electrolyte components. We also found that gas evolution in DEMS was significantly impacted by the age of the electrolyte, as is shown in Section 4.8.1 and discussed below. However, we note that no distinguishable POF_3 signature was observed (via Reaction 4.4.2) during DEMS experiments, indicating that the aging of electrolytes over the course of a single DEMS experiment (~1 day) was negligible.

The inset of Figure 4.1a shows that H_2 is the first gas to evolve after cycling commences, and Figure 4.1b shows that H_2 evolution primarily occurs in the first ~3 hours of C/10 formation. Interestingly, we found that electrolytes that had been aged longer exhibited more H_2 evolution (see Section 4.8.1). Because the aged electrolyte is expected to have a larger ratio of HF to H_2O (see Reactions 4.4.1 and 4.4.2), this suggests that HF is preferentially reduced over H_2O. We can rationalize this in part due to the larger dielectric constant of HF (~84) compared to H_2O (~78), which implies that HF is more likely to solvate Li^+, and therefore HF will be preferentially reduced as HF-solvated Li^+ migrates to the graphite surface. We therefore propose that H_2 evolution coincides predominantly with LiF deposition on the graphite surface (as illustrated in the inset of Figure 4.1b and shown in Reaction 4.4.3), although some smaller amount of LiOH also likely deposits from the reduction of H_2O (see Reaction 4.4.4). By integrating the total amount of H_2 evolved in Figure 4.1b, we find that ~65 nmol of H_2 is evolved from the 12 mm diameter electrode (3.2 mAh total nominal capacity), corresponding to ~130 nmol of LiF deposited if indeed Reaction 4.4.3 is the dominant mechanism of H_2 evolution.

$$2\,Li^+ + 2\,HF + 2\,e^- \longrightarrow 2\,LiF + H_2 \tag{4.4.3}$$

$$2\,Li^+ + 2\,H_2O + 2\,e^- \longrightarrow 2\,LiOH + H_2 \tag{4.4.4}$$

Additional H_2 could also be evolved to convert LiOH to Li_2O, as shown in Reaction 4.4.5.

$$2\,Li^+ + 2\,LiOH + 2\,e^- \longrightarrow 2\,Li_2O + H_2 \tag{4.4.5}$$

This line of reasoning is consistent with previous measurements of graphite SEI composition, which typically report a LiF-rich inner-SEI with sporadic LiOH and Li_2O.[3;71]

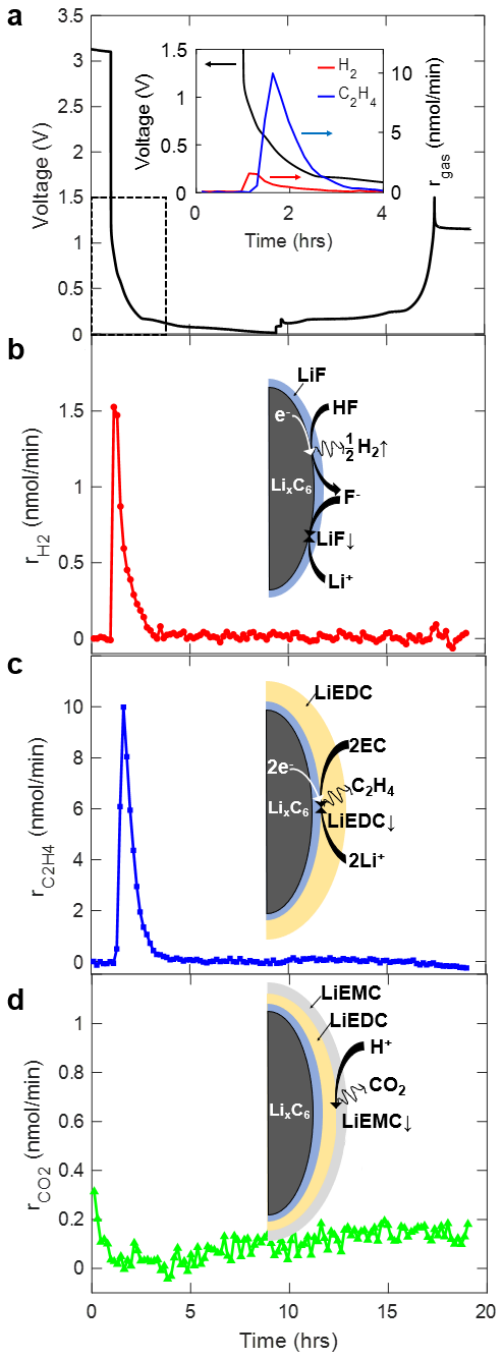

Figure 4.1: DEMS measurements for the formation (first) cycle of a Li-graphite cell with 1.2 M $LiPF_6$ electrolyte. **a.** Voltage profile for one C/10 cycle, with inset showing H_2 (red) and C_2H_4 (blue) gas evolution during first 4 hours. **b.** H_2 gas evolution rate (r_{H2}) with inset showing LiF deposition mechanism (see Reaction 4.4.3). **c.** C_2H_4 gas evolution rate (r_{C2H4}) with inset showing LiEDC deposition mechanism (see Reaction 4.4.6). **d.** CO_2 gas evolution rate (r_{CO2}) with inset showing LiEMC chemical formation mechanism (see Reactions 4.4.11 and 4.4.10).

4.4.2 Ethylene Evolution

Ethylene evolution primarily arises from the reduction of EC to form LiEDC, according to Reaction 4.4.6, although recent studies suggest LiEDC undergoes further reaction once deposited as mentioned in Section 4.4.3.[48] The onset of C_2H_4 evolution occurs slightly after the onset of H_2 evolution, as shown in the inset of Figure 4.1a, and it persists for about 4 hours, as shown in Figure 4.1c. This C_2H_4 evolution coincides with the formation of the outer-SEI, which is rich in alkyl carbonates derived from the originally deposited LiEDC.

$$2\,Li^+ + 2\,(CH_2O)_2CO\ (EC) + 2\,e^- \longrightarrow (CH_2OCO_2Li)_2\ (LiEDC) + C_2H_4 \tag{4.4.6}$$

Reaction 4.4.7 shows another previously proposed mechanism by which C_2H_4 is evolved, where Li_2CO_3 forms from EC reduction instead of LiEDC.[72] However, the abundance of alkyl carbonates in the vast majority of characterized SEI films suggests that Reaction 4.4.6 occurs to a far greater extent than Reaction 4.4.7.[55;71]

$$2\,Li^+ + (CH_2O)_2CO\ (EC) + 2\,e^- \longrightarrow Li_2CO_3 + C_2H_4 \tag{4.4.7}$$

4.4.3 Carbon Dioxide Evolution

Figure 4.1d shows that some CO_2 is evolved during the initial rest period, and after about five hours, a steady rate of CO_2 evolution is again observed. As will be described below, the initial CO_2 evolution likely arises from the hydrolysis of EC, while the steady evolution of CO_2 later in cycling likely arises due to the reaction of LiEDC with H_2O and HF, which is illustrated in the inset of Figure 4.1d. The inset depicts the reaction front beginning from the outermost portion of the LiEDC layer and gradually moving inwards, converting more and more LiEDC to LiEMC. This mechanism will be further justified in Section 4.5.2.

EC can be directly hydrolyzed by water or can react with hydroxide (OH^-) which may be present due to water reduction at the Li metal counter electrode.[47;73;74;75] Both EC reaction pathways evolve CO_2, as shown in Reactions 4.4.8 and 4.4.9.

$$(CH_2O)_2CO\ (EC) + H_2O \longrightarrow CO_2 + (CH_2OH)_2\ (EG) \tag{4.4.8}$$

$$(CH_2O)_2CO\ (EC) + OH^- \longrightarrow CO_2 + HOCH_2CH_2O^-\ (EG^-) \tag{4.4.9}$$

Another source of CO_2 evolution is the reaction of existing graphite SEI components with H_2O and HF.[75] As discussed in Section 4.4.2, a common graphite SEI component formed

under EC-containing electrolytes is LiEDC. This species, despite its frequent mention in the SEI literature for decades,[76;77] was only successfully synthesized in 2019. Previous attempts at synthesizing LiEDC had actually synthesized LiEMC,[78;79;80;81] and this called into question the true chemical composition of the graphite SEI. Wang et al. posited that LiEDC forms initially but is converted to LiEMC via an unknown mechanism.[48] A key finding of our work is that LiEDC is prone to react with both H_2O and HF via the proposed Reactions 4.4.10 and 4.4.11 to form LiEMC and in the process evolve CO_2.

$$(CH_2OCO_2Li)_2 \text{ (LiEDC)} + H_2O \longrightarrow CO_2 + LiOH + HOCH_2CH_2OCO_2Li \text{ (LiEMC)} \tag{4.4.10}$$

$$(CH_2OCO_2Li)_2 \text{ (LiEDC)} + HF \longrightarrow CO_2 + LiF + HOCH_2CH_2OCO_2Li \text{ (LiEMC)} \tag{4.4.11}$$

LiEMC may also undergo an additional protonation with H_2O or HF to form EG and evolve yet another CO_2 as shown in Reactions 4.4.12 and 4.4.13.

$$HOCH_2CH_2OCO_2Li \text{ (LiEMC)} + H_2O \longrightarrow CO_2 + LiOH + (CH_2OH)_2 \text{ (EG)} \tag{4.4.12}$$

$$HOCH_2CH_2OCO_2Li \text{ (LiEMC)} + HF \longrightarrow CO_2 + LiF + (CH_2OH)_2 \text{ (EG)} \tag{4.4.13}$$

However, there remains debate about the exact reaction mechanism involving SEI components and H_2O or HF. Reaction 4.4.14, for example, shows a previously proposed double protonation of LiEDC reaction mechanism which results in Li_2CO_3.[75] Since Li_2CO_3 is typically reported to be either not present at all[82;83;84] or confined to the inner-SEI,[3;85] and the reaction of LiEDC with H_2O or HF would occur starting from the outermost-SEI and proceed inwards (as will be elaborated on in Section 4.4.3), we propose that sequential protonation from LiEDC to LiEMC to EG (as described in Reactions 4.4.10-4.4.13) is more likely.

$$(CH_2OCO_2Li)_2 \text{ (LiEDC)} + H_2O \longrightarrow CO_2 + Li_2CO_3 + (CH_2OH)_2 \text{ (EG)} \tag{4.4.14}$$

It should also be noted that full cells with transition metal oxide cathodes may further exacerbate these effects, as EC can be deprotonated at high oxidative potentials to form H^+, which could lead to further conversion of LiEDC and additional CO_2 evolution.[86;87]

4.5 Effect of Salt Concentration on Initial SEI Formation

4.5.1 Inner-SEI: LiF, LiOH, and Li_2O via H_2 Evolution

As described in Section 4.4.1 (specifically Reaction 4.4.3), we propose that H_2 evolution coincides primarily with LiF deposition, and some H_2 evolution also coincides with LiOH and Li_2O deposition (see Reactions 4.4.4 and 4.4.5). These three components together make up the LiF-rich inner-SEI. We find in Figure 4.2a-d that $LiPF_6$ concentration has a significant impact on the H_2 evolution. From 0.35 M to 1.2 M $LiPF_6$, the H_2 evolution peak increases in height yet remains a consistent duration. In contrast, the H_2 evolution signature for the 2.0 M $LiPF_6$ electrolyte is broader and persists for over five hours. The anomalous gassing behavior for the 2.0 M electrolyte could be caused by the high viscosity of the 2.0 M electrolyte leading to slow wetting of the electrode pores or slow diffusion of H_2 through the electrolyte. Alternatively, the high concentration of Li^+ could alter the distribution of solvated species in solution (e.g., solvent separated ion pairs, contact ion pairs, aggregates, etc.), causing the solvent (in this case, H_2O or HF) surrounding these different species to be reduced over a broad range of potentials.

The total H_2 evolution during cycling for each electrolyte is shown Figure 4.2e, revealing that the total H_2 evolved (and therefore the total thickness of the inner-SEI layer) increases with increasing $LiPF_6$ concentration. LiF was also specifically isolated and quantified for coin cell electrodes via a ^{19}F-NMR method, and the results and method are described in Section 4.8.3. However, the DEMS H_2 results and the LiF amounts measured on coin cell electrodes were difficult to compare due to the effect of remnant $LiPF_6$ in the rinse solution, and quantification of LiF on electrodes extracted from DEMS cells will be the subject of future work.

DEMS was also performed on a cell using the same 1.2 M electrolyte in Figure 4.2c after it had been aged for over three months. As discussed in Section 4.4.1, the extensive aging spurred additional HF formation in the electrolyte, which resulted in an almost fourfold increase in DEMS H_2 evolution over that observed in Figure 4.2c (see Section 4.8.1).

The implications of the inner-SEI thickness on battery operation are also important to consider. A thinner overall SEI may be advantageous for charge transfer, as Li^+ must transport through the SEI layer to ultimately insert into graphite. The inner-SEI layer is generally thought to be compact, while the outer-SEI is thicker and more porous,[4] making the overall SEI thickness governed primarily by the outer-SEI. However, it is unclear exactly how Li^+ transports through the SEI layer. It is likely that the Li^+ remains at least partially

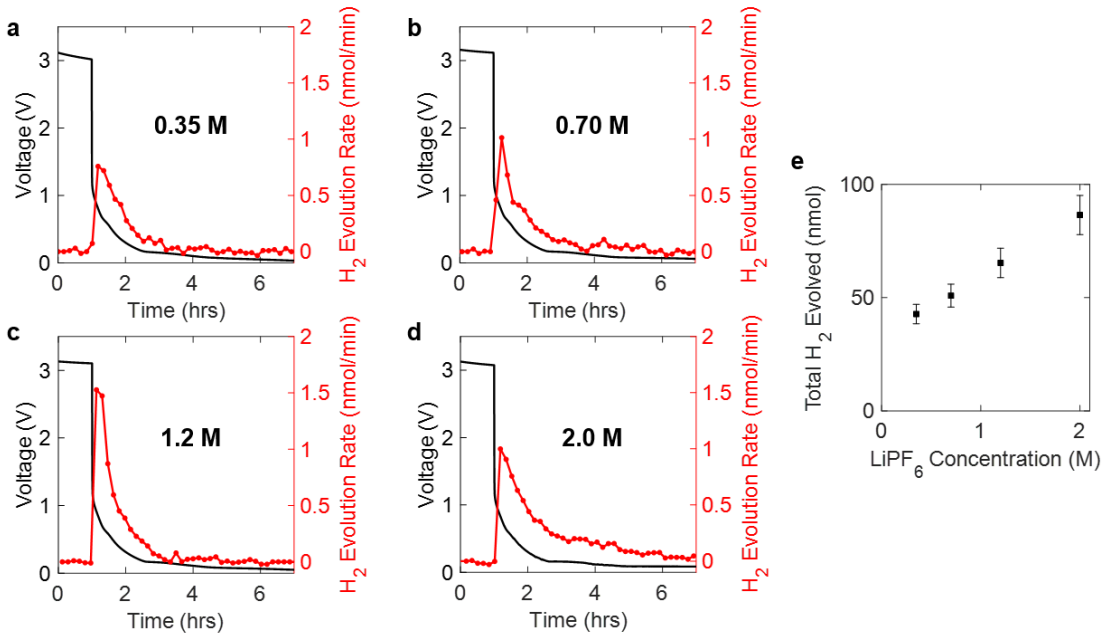

Figure 4.2: DEMS H_2 evolution in Li-graphite half cells cycled at C/10 with **a.** 0.35 M $LiPF_6$, **b.** 0.70 M $LiPF_6$, **c.** 1.2 M $LiPF_6$, and **d.** 2.0 M $LiPF_6$ electrolytes. **e.** Total H_2 evolved as a function of $LiPF_6$ concentration. Measurement error arising from integration of DEMS data is shown as ±10%.

solvated as it enters the outermost portion of the SEI, and it eventually strips all of its solvation shell by the time it reaches the graphite surface. It is possible that the interface between the inner-SEI and outer-SEI is the point at which Li^+ strips the last of its solvation shell, and Li^+ migrates through the inner-SEI layer by hopping between F^-, given that this inner-SEI is compact and likely would not accommodate a bulky solvated Li^+. Depending on which mode of transport is slower (i.e., transport of partially solvated Li^+ through the outer-SEI or Li^+ hopping through the inner-SEI), SEI composition should be tailored accordingly.

4.5.2 Outer-SEI: Solid Carbonates via C_2H_4 Evolution and MST

The outer-SEI is comprised primarily of solid carbonates (such as LiEDC and LiEMC), and its initial formation coincides with C_2H_4 evolution from the reaction of EC to deposit LiEDC (see Reaction 4.4.6). As described in Section 4.4.3, although LiEDC is thought to form initially, LiEDC can be further converted via an undetermined mechanism to LiEMC.[48] In light of this, the conversion of LiEDC to LiEMC and the outer-SEI composition generally warrant further investigation.

We find in our study that $LiPF_6$ concentration plays a pivotal role in the formation of the outer-SEI layer, and we track the formation of LiEDC via the evolution of C_2H_4 in DEMS. Figure 4.3a-d shows the C_2H_4 evolution signatures for all four tested electrolyte compositions. We find that the C_2H_4 evolution peak height gradually decreases with increasing $LiPF_6$ concentration from 0.35 M to 1.2 M, but the peak duration remains similar. For the 2.0 M

electrolyte, the peak is much broader and spans about six hours, which is similar to the H_2 evolution behavior for the 2.0 M electrolyte. This broad peak for the 2.0 M electrolyte may arise due to similar reasons listed in Section 4.5.1 (i.e., electrolyte viscosity or Li^+ solvation effects).

Summing the total C_2H_4 evolved, we find in Figure 4.3e that C_2H_4 evolution monotonically decreases with increasing $LiPF_6$ concentration. This decrease in solid carbonate layer thickness may be attributed in part to the partial passivating effect of a thicker inner-SEI, which may inhibit some solid carbonate deposition for higher concentration electrolytes. However, we find that after the 1.2 M electrolyte used in Figure 4.3c was aged three months, the H_2 evolution increased almost fourfold yet the C_2H_4 evolution remained similar (within ~5%, see Section 4.8.1), indicating the passivating effect of the inner-SEI is minor. Instead, the outer-SEI thickness is likely governed by solvation of Li^+. The ratios of EC to Li^+ in 0.35 M, 0.70 M, 1.2 M, and 2.0 M $LiPF_6$ in 3:7w EC:EMC electrolytes are 10.5, 5.3, 3.1, and 1.8, respectively. Since the inner solvation shell of Li^+ contains ~4 EC when sufficient EC is present,[88] the 1.2 M and especially the 2.0 M electrolyte may contain a significant amount of contact ion pairs and aggregates with lower EC coordination numbers. The abundance of free (i.e., not actively solvating) EC for lower concentration electrolytes could lead to increased EC reduction and a thicker solid carbonate layer. Likewise, for higher concentration electrolytes, the lack of free EC could lead to a thinner solid carbonate layer. Similar logic about solvation and ion aggregation effects has been applied to explain the thin SEIs formed on graphite with superconcentrated (greater than ~3 M) electrolytes.[89]

While C_2H_4 evolution provides a measure of the LiEDC initially deposited, some LiEDC may be converted to other species. To measure the extent of this conversion, MST was used to quantify the total amount of solid carbonate species that remained on each of the electrodes cycled in DEMS. As described in Section 4.3.3, under our definition of solid carbonates, LiEDC is counted as two solid carbonates, as there are two carbonate groups per LiEDC and two CO_2 are evolved from one LiEDC upon titration. LiEMC and Li_2CO_3 are likewise each counted as a single solid carbonate. The total amount of solid carbonates measured via MST for each electrode cycled in DEMS is overlaid with the total C_2H_4 evolved during DEMS in Figure 4.3e, and we find that the total amount of solid carbonates is greater than the amount of C_2H_4 evolved for each electrolyte composition.

By taking the ratio of the CO_2 evolved during MST to the C_2H_4 evolved during DEMS, we can gain a sense for the extent of conversion of LiEDC to other species. This is illustrated in Figure 4.3f, which shows that this ratio is ~1.5 for all electrolyte compositions tested. We would expect a ratio of 2.0 CO_2 (MST) per C_2H_4 (DEMS) if all LiEDC remained intact on the electrode, so the ratio of 1.5 implies that ~25% of the solid carbonates from the initial LiEDC deposition are consumed or converted to some non-carbonate species. A number of mechanisms could lead to this reduction in the amount of solid carbonates. Referring back to Section 4.4.3, the CO_2 evolution during DEMS can be attributed in part to the reaction of LiEDC with H_2O or HF (see Reactions 4.4.10 and 4.4.11). As seen in Section 4.8.5, the CO_2 evolved during DEMS, if entirely attributed to the reaction of H_2O or HF with LiEDC, would imply that ~8% of the LiEDC was converted to LiEMC for all electrolyte

compositions. Section 4.8.1 shows that after the electrolyte is aged about three months, DEMS CO_2 evolution rate increases substantially, likely because the increased amount of HF in solution after aging increases the reaction rate of LiEDC to LiEMC. The CO_2 (MST) to C_2H_4 (DEMS) ratio also decreases to ~0.94 when using the aged electrolyte, indicating that electrolyte aging further promotes the conversion of LiEDC to LiEMC and non-carbonate species. The remainder of the 'missing' solid carbonates from Figure 4.3f may have been converted to other species, such as Li_2C_2, oxalates, or alkoxides (see Section 4.8.6). It is also possible that some C_2H_4 evolution arises from the two-electron reduction of EC to form Li_2CO_3 (see Reaction 4.4.7), which would contribute only one solid carbonate deposited per C_2H_4 evolved compared to two solid carbonates per C_2H_4 for the LiEDC-forming reaction, although it is unlikely that this two-electron reduction of EC is a major contributor to the missing carbonates, as the LiEDC-forming reaction is typically much more prevalent.[55] It is also unlikely that the DMC rinse procedure removes solid carbonates, as the solid carbonate species are insoluble in DMC and do not react with DMC out of solution.[48] In all, the combination of DEMS C_2H_4 and CO_2 evolution suggest that ~8% of LiEDC is converted to LiEMC, and solid carbonate quantification via MST indicates that LiEDC is further converted to other non-carbonate species for a total of ~25% conversion of solid carbonates for all similarly aged electrolyte compositions in Figure 4.3.

The insights gleaned from our measurements can help inform the next generation of the so-called 'mosaic model' of the graphite SEI,[5] which originally posited that the SEI is composed of a LiF and Li_2O inner layer with a semi-carbonate and Li_2CO_3 outer layer. Starting from the outermost layer and working inwards, our measurements indicate that LiEMC is likely the outermost constituent of the SEI, as the reaction of LiEDC to LiEMC is expected to be begin at the SEI-electrolyte interface and proceed inward (as shown in the inset to Figure 4.1d). Moving further inward, we then expect a layer of LiEDC which has not been converted to other species, followed by LiEDC reduction products (such as Li_2C_2, oxalates, and alkoxides), which must be in contact with the reducing graphite surface and are therefore likely intertwined with the inner-SEI. Then, as discussed in Section 4.4.1, the innermost-SEI contains primarily LiF with some LiOH and Li_2O interspersed. Although Li_2CO_3 was hypothesized to be abundant in the original mosaic SEI model, many studies since have found minimal[3;85] or no Li_2CO_3.[82;83;84] Reactions 4.4.14 and 4.4.7 are potential pathways for Li_2CO_3 formation, but they are unlikely to occur to a great extent as discussed earlier. Possible origins of Li_2CO_3 are discussed in Section 4.8.6.

4.6 SEI Evolution with Fast Charge

4.6.1 Single Fast Charge Cycle

With the SEI formed under each electrolyte composition characterized, we then explored how the initial SEI affects fast charge operation and how the SEI changes as a result of fast charge. Generally, a thinner initial SEI is preferential for fast charge, as overpotentials which arise from Li^+ transport through the SEI layer can lead to Li plating and rapid capacity

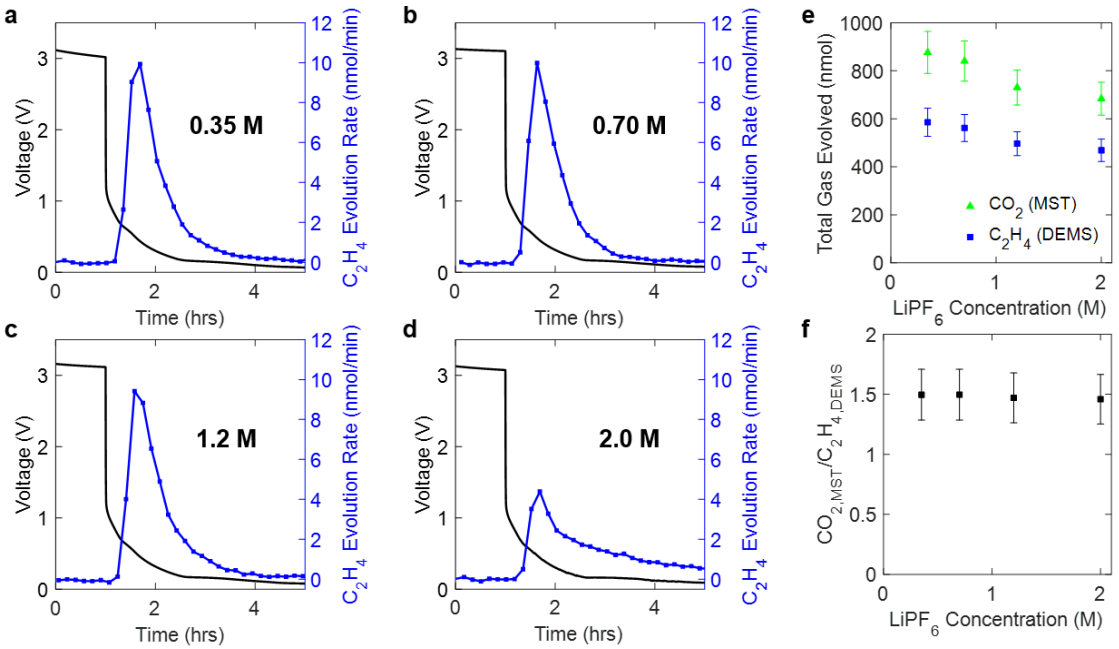

Figure 4.3: DEMS C_2H_4 evolution in Li-graphite half cells cycled at C/10 with **a.** 0.35 M $LiPF_6$, **b.** 0.70 M $LiPF_6$, **c.** 1.2 M $LiPF_6$, and **d.** 2.0 M $LiPF_6$ electrolytes. **e.** Total C_2H_4 evolved from DEMS overlaid with total CO_2 evolved from MST as a function of $LiPF_6$ concentration. Measurement error arising from integration of both DEMS and MST data is shown as $\pm 10\%$. **f.** Ratio of CO_2 evolved from MST to C_2H_4 evolved from DEMS, with error propagated from panel e.

fade. We classify plated Li as yet another SEI component which is intertwined with the LiF, solid carbonates, and other species present in the initial SEI. Once plated, Li can undergo a number of processes:

1. It can be reversibly stripped from the graphite surface upon deintercalation.
2. It can chemically insert into graphite.[7;8]
3. It can become electronically isolated from the graphite, resulting in dead Li.[2]
4. It can react with other SEI components or with electrolyte to form additional SEI species.[2]

While processes 1 and 2 are reversible, processes 3 and 4 are irreversible and directly lead to capacity fade during fast charge cycling. Using MST, we quantify the amount of dead Li and additional SEI formed after fast charge, and we compare the results against Li plating/stripping behavior predicted by an electrochemical model (see Section 4.8.4), using a constant Li stripping efficiency of 70% as determined by previous work.[2]

The onset of Li plating was determined by strategically cycling a series of Li-graphite coin cells with the following steps:

1. Three constant-current C/10 formation cycles with 0.010 V and 1.5 V cutoff potentials and 15-minute open circuit voltage (OCV) rest periods between each charge and discharge.

2. One 4C (based upon a 350 mAh/g reversible capacity) charge (intercalation into graphite) to a given theoretical graphite state of charge (SOC).

3. A 30 minute OCV rest period.

4. One C/10 discharge (deintercalation from graphite) to 1.5 V.

The fast charge followed by a slow discharge ensured that all reversible lithiated graphite was delithiated and all reverislby plated Li was stripped, leaving only dead Li which was measured via MST.

The irreversible capacity of the fast charge cycle (obtained from cycling data) is overlaid with the dead Li measured via MST and the model-predicted dead Li for the 0.35 M, 0.70 M, 1.2 M, and 2.0 M electrolytes in Figure 4.4a-d. It is clear from these data that the majority of capacity loss during the fast charge cycle is due to dead Li formation, but some of the remaining capacity loss can be attributed to a slight increase in solid carbonates above the baseline amount observed after formation cycling, especially for the lower concentration electrolytes (see Section 4.8.7). As mentioned in Section 4.3.3, there is a baseline amount of ~300 nmol/cm^2 dead lithiated graphite present even after formation cycling due to the physical dislodgement of graphite particles from lithiation-induced volumetric changes of the particles during cycling. An increase in the amount of dead Li above this baseline amount is attributed to dead Li metal from fast charging. The model fits the experimental dead Li data well for the 1.2 M electrolyte (as model parameters had been previously developed for this concentration), but generally underpredicts the amount of dead Li at a given SOC for the 0.35 M and 0.70 M electrolyte and overpredicts the amount of dead Li for the 2.0 M electrolyte. This discrepancy between model and experiment can be ascribed to changes in SEI impedance for cells formed with the electrolytes above and below 1.2 M, which the model as formulated does not capture. In Section 4.8.8, the SEI impedance is measured for each electrolyte composition using impedance spectroscopy in a three electrode configuration, revealing that the 0.35 M and 0.70 M electrolyte result in a higher graphite SEI impedance than the 1.2 M electrolyte, and the 2.0 M electrolyte has the lowest graphite SEI impedance of all tested electrolyte compositions. Incorporating these SEI resistances into previously developed models which include a graphite film resistance resulted in counterintuitive predicted Li plating behavior which did not match experimental results (as described in Section 4.8.4). This highlights the need for next-generation models that more accurately and explicitly capture SEI effects as novel electrolyte formulations which impart beneficial SEI properties to enable fast charging are developed.

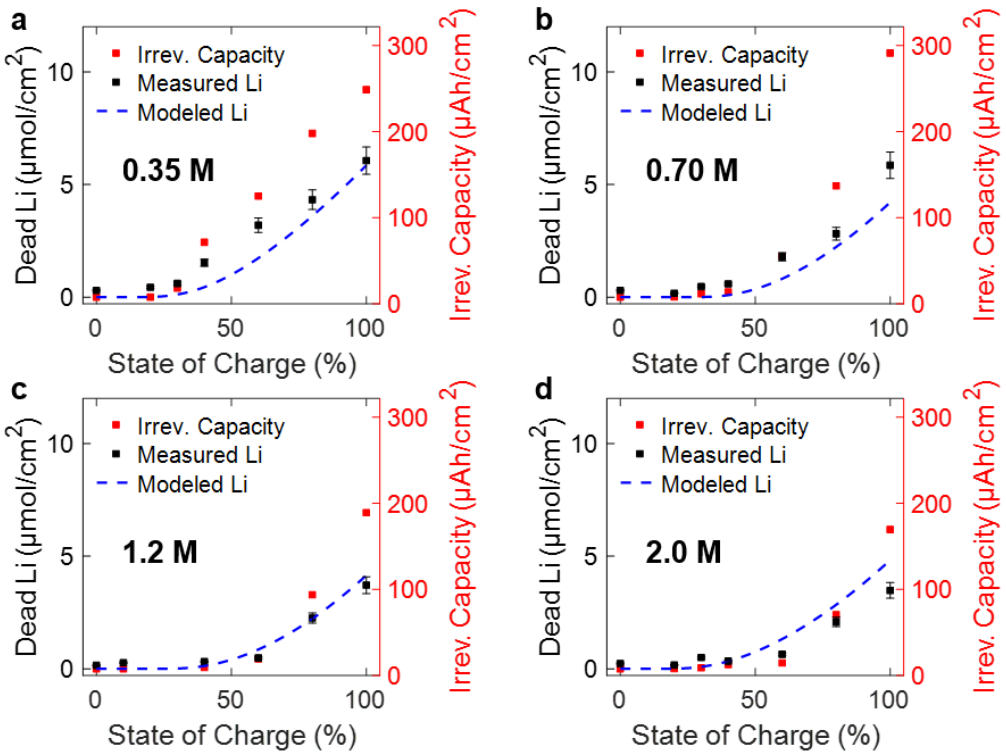

Figure 4.4: Modeled and experimental dead Li measurements for 0.35 M to 2.0 M $LiPF_6$ electrolytes. Experimental irreversible capacity (red markers, right y-axis) measured for a single fast charge cycle to a given SOC overlaid with dead Li measured via MST (black markers, left y-axis) and model predicted dead Li (blue dashed line) for **a.** 0.35 M $LiPF_6$, **b.** 0.70 M $LiPF_6$, **c.** 1.2 M $LiPF_6$, and **d.** 2.0 M $LiPF_6$ electrolytes. Measurement error arising from integration of MST data is shown as ±10%, and irreversible capacity error bars are within the size of the data point (~1 µAh/cm^2). The left and right y-axes are scaled equivalently (i.e., 1 µmol/cm^2 Li = 26.8 µAh/cm^2).

4.6.2 Multiple Fast Charge Cycles

We also measured the amount of dead Li, solid carbonates, and Li_2C_2 (see Section 4.8.2) on graphite electrodes that underwent multiple fast charge cycles. Similar to Section 4.6.1, Li-graphite coin cells were cycled with three C/10 formation cycles followed by a 4C charge to 100% theoretical graphite SOC and a C/10 discharge to 1.5 V. This 4C fast charge cycle was then was then repeated up to a maximum of ten cycles. The amounts of dead Li and solid carbonates quantified for all tested electrolyte compositions are shown in Figure 4.5a and 4.5b, respectively.

We find in Figure 4.5a that the dead Li remaining on the graphite electrode monotonically decreases with increasing electrolyte salt concentration. This trend is fairly well in line with that observed in Figure 4.4a-d for a single fast charge cycle, but the difference in dead Li amounts between electrolyte compositions is exacerbated after prolonged cycling. The reduced amount of dead Li is in part due to the lower SEI impedance for the higher concentration electrolytes as discussed in Section 4.6.1, which leads to less Li plating for the higher concentration electrolytes. Additionally, the larger amount of LiF deposition when using the high concentration electrolytes likely improves the reversibility of Li plating/stripping, as numerous studies of Li plating/stripping on Cu indicate that LiF-depositing additive (such as fluoroethylene carbonate) impart a uniform columnar plated Li morphology and improve plating/stripping reversibility.[32;90]

Beyond the benefit of decreased dead Li formation, high salt concentration electrolytes also reduce the amount of additional solid carbonate deposition during fast charge, which occurs as a result of the reaction of plated Li metal with electrolyte.[2] For small amounts of Li plating, the Li is well encapsulated by the existing SEI and has minimal contact with electrolyte, so minimal additional solid carbonate formation is observed (see Section 4.8.7). However, the accumulation of dead Li over the course of many cycles and the increased impedance of the SEI as dead Li accumulates may result in mossy Li which extends beyond the SEI and contacts the bulk electrolyte, resulting in additional solid carbonate deposition as observed in Figure 4.5b. The benefit of the increased amount of LiF in the SEI for high concentration electrolytes may again play a role, as the expected uniform morphology of plated Li for the higher concentration electrolytes would reduce the plated Li surface area in contact with electrolyte and result in less additional solid carbonate formation.

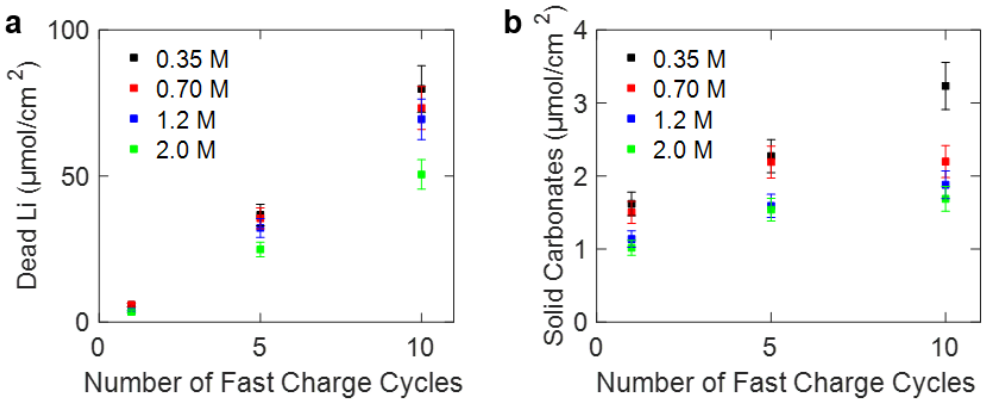

Figure 4.5: Dead Li and solid carbonates quantified during prolonged fast charge cycling for 0.35 M to 2.0 M $LiPF_6$ electrolytes. Quantification of dead Li (**a.**) and solid carbonate (**b.**) graphite SEI species measured via MST on electrodes that have undergone multiple fast charge cycles in 0.35 M, 0.70 M, 1.2 M, and 2.0 M $LiPF_6$ in 3:7w EC:EMC electrolyte. Measurement error arising from integration of MST data is shown as ±10%.

4.7 Conclusions

Using DEMS and MST, we completed a comprehensive, quantitative characterization of graphite SEI formation under electrolytes of varying $LiPF_6$ concentration. Our findings reveal that as $LiPF_6$ concentration increases, a thicker inner-SEI (rich in LiF) and a thinner outer-SEI (rich in alkyl carbonates) is formed. We also find that, although LiEDC is initially deposited, H_2O and HF convert LiEDC to LiEMC, and a host of other reactions convert LiEDC to non-carbonate species. The SEI resistance also plays a pivotal role in fast charge performance, as the thinnest, least resistive SEI formed under the 2.0 M electrolyte resulted in less dead Li than was predicted by an electrochemical model without explicit SEI effects. The benefit of the 2.0 M electrolyte SEI was maintained over the course of multiple fast charge cycles, as electrolytes with higher salt concentrations resulted in a decreased rate of dead Li formation and solid carbonate deposition. This work uncovers the potential of highly concentrated electrolytes as suitable candidates for fast charge applications and suggests that next-generation electrochemical modeling frameworks must appropriately incorporate SEI effects to accurately capture Li plating behavior.

4.8 Supporting Information

4.8.1 Effect of Electrolyte Aging

The electrolytes used in Figures 4.1, 4.2, and 4.3 were each aged for one week before being used in DEMS cells. We also performed DEMS on the same 1.2 M $LiPF_6$ electrolyte used in Figure 4.1 (also used in Figure 4.2c and 4.3c) after it had been aged for three months. The electrolyte container was only opened periodically (about once every three weeks), making

it unlikely that additional water contamination entered the container during storage in the glovebox (which was maintained at less than 2 ppm H_2O). Full DEMS characterization using the 3-month aged electrolyte is shown in Figure 4.6. We note in Figure 4.6a that the voltage profile remains similar after three months, although the lower cutoff potential is reached about two hours earlier. Interestingly, we observe about four times more H_2 evolution (see Figure 4.6b) after three months compared to after one week (~237 nmol versus ~65 nmol H_2), likely because the H_2O within the electrolyte had converted more $LiPF_6$ to HF after three months, resulting in more H_2 evolution as described in Section 4.4.1. The C_2H_4 evolution (see Figure 4.6c), however, remained similar (~505 nmol versus ~496 nmol C_2H_4), indicating that the thicker inner-SEI formed in the 3-month aged electrolyte did not materially impact the outer-SEI thickness (as mentioned in Section 4.5.2). The CO_2 evolution, which plateaued at just under 0.2 nmol/min in the one-week aged electrolyte, plateaued at just over 0.4 nmol/min with the three-month aged electrolyte, and the cumulative CO_2 evolved (excluding the CO_2 evolved during the initial rest period) increased about fourfold (~330 nmol versus ~80 nmol) for the three-month aged electrolyte (see Figure 4.6d), indicating that LiEDC may react more readily with HF than H_2O. The graphite electrode was also extracted from the DEMS cell and titrated, and 474 nmol of solid carbonates were quantified, corresponding to a CO_2 (MST) to C_2H_4 (DEMS) ratio of ~0.94 (compared to ~1.50 for one-week aged), or ~53% consumption of the initially deposited solid carbonates (compared to ~25% for one-week aged). If DEMS CO_2 evolution were ascribed entirely to the conversion of LiEDC to LiEMC, this would imply a ~33% reduction in solid carbonates for the three-month aged electrolyte (compared to ~8% for one-week aged). These results together suggest that the additional HF formed in aged electrolytes results in increased H_2 evolution and increased conversion of LiEDC to LiEMC.

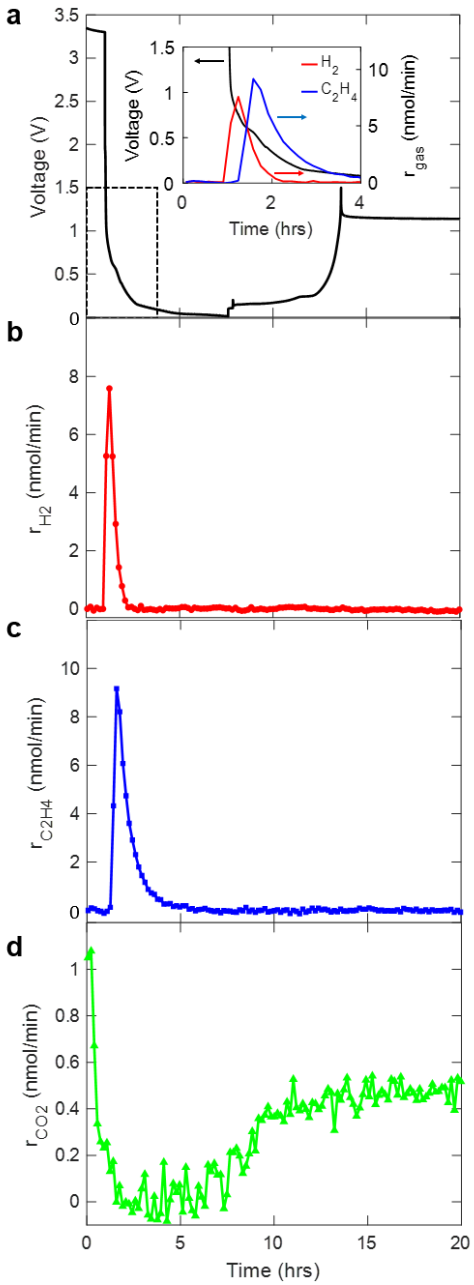

Figure 4.6: DEMS measurements for the formation (first) cycle of a Li-graphite cell with 1.2 M $LiPF_6$ electrolyte from Figure 4.1 after the electrolyte had been aged for three months. **a.** Voltage profile for one C/10 cycle, with inset showing H_2 (red) and C_2H_4 (blue) gas evolution during first 4 hours. **b.** H_2 gas evolution rate (r_{H2}). Cumulative H_2 evolved increased about fourfold compared to Figure 4.1. **c.** C_2H_4 gas evolution rate (r_{C2H4}). Cumulative C_2H_4 evolved remained similar (within ~2%) to Figure 4.1. **d.** CO_2 gas evolution rate (r_{CO2}). Cumulative CO_2 evolved increased about fourfold compared to Figure 4.1.

4.8.2 Li_2C_2 Quantification

Previous studies have indicated that Li_2C_2 is present in the SEI of both graphite[2?] and Li metal,[49] and it can also form via the reduction of Li_2CO_3 (see previously proposed Reaction 4.8.1).[59] The presence of plated Li on graphite has also been correlated to the amount of Li_2C_2 in the SEI, and the amount of Li_2C_2 has been found to increase on graphite electrodes that had rested at OCV longer after fast charge (when ample plated Li was present), suggesting Li_2C_2 forms due to a chemical reaction between plated Li and other SEI components.[2?] A small amount of Li_2C_2 (~10 nmol/cm^2) is also observed after formation cycling,[2] and this initially deposited Li_2C_2 is likely formed via the reduction of LiEDC. The mechanism of conversion from LiEDC to Li_2C_2 is currently unknown, but it likely involves many sequential reduction steps, and the reaction products probably include both oxides and Li_2C_2 (similar to Reaction 4.8.1).

$$Li_2CO_3 + 5\,Li^+ + 5\,e^- \longrightarrow 0.5\,Li_2C_2 + 3\,Li_2O \tag{4.8.1}$$

4.8.2.1 DEMS Cells

As shown in Figure 4.7, the amount of Li_2C_2 measured via MST on the graphite electrodes cycled in DEMS cells (corresponding to Figures 4.1, 4.2, and 4.3) monotonically decreases as a function of $LiPF_6$ concentration. The decrease in Li_2C_2 may arise due to the thicker inner-SEI observed for high concentration electrolytes, which would reduce the available graphite surface area for solid carbonate reduction to occur.

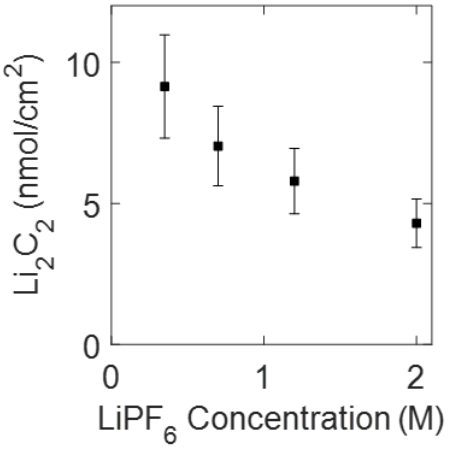

Figure 4.7: Li_2C_2 measured via MST as a function of $LiPF_6$ concentration on electrodes extracted from the DEMS cells corresponding to Figures 4.1, 4.2, and 4.3. Measurement error of ±20% arising from integration and calibration of the C_2H_2 evolution signature upon titration is shown.

4.8.2.2 Coin Cells

Li_2C_2 was also quantified via MST for the coin cell electrodes used in Figure 4.4, and the results are shown in Figure 4.8a-d for the four $LiPF_6$ concentrations studied. There is a baseline amount of ~5 nmol/cm^2 Li_2C_2 at low SOCs, and a clear increase in the amount of Li_2C_2 is observed at 80% SOC for the 0.35 M electrolyte and at 100% SOC for the 0.70 M, 1.2 M, and 2.0 M electrolytes. The additional Li_2C_2 at high SOCs is likely formed via the reaction of plated Li with existing solid carbonate species as described earlier.[2]

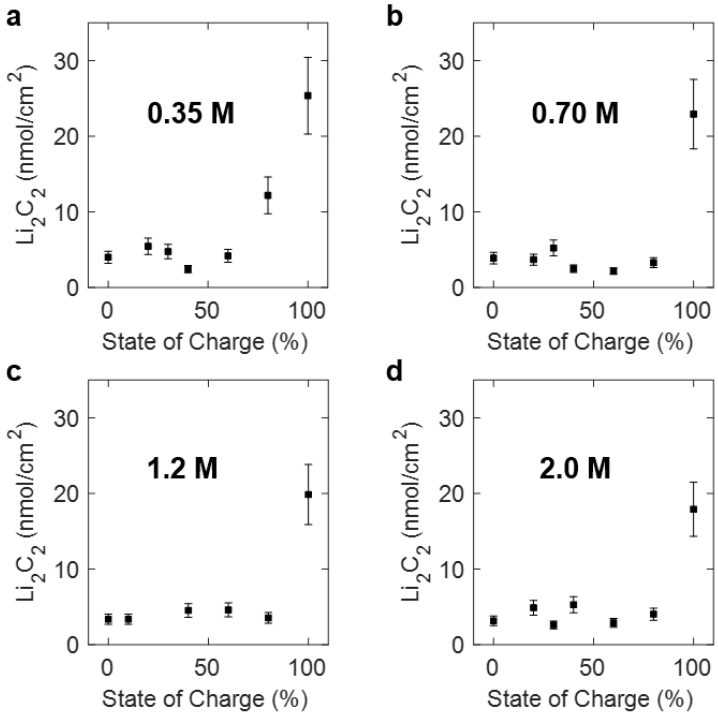

Figure 4.8: Li_2C_2 measured via MST as a function of state of charge on electrodes extracted from the coin cells corresponding to Figure 4.4 for electrolytes of **a.** 0.35 M $LiPF_6$, **b.** 0.70 M $LiPF_6$, **c.** 1.2 M $LiPF_6$, and **d.** 2.0 M $LiPF_6$ in 3:7w EC:EMC. Electrodes underwent formation cycling and were then fast charged (4C rate) to the nominal SOCs provided. Measurement error of ±20% arising from integration and calibration of the C_2H_2 evolution signature upon titration is shown.

Finally, Li_2C_2 was quantified via MST for the coin cell electrodes used in Figure 4.5, and the results are shown in Figure 4.9. Interestingly, the amount of Li_2C_2 quantified after multiple fast charge cycles for each electrolyte composition was very similar. This may be because the plated Li surface area in direct contact with solid carbonate SEI components is fairly consistent among all the electrolyte compositions after many fast charge cycles (as ample Li has plated in all conditions), resulting in a similar amount of Li_2C_2 regardless of electrolyte composition.

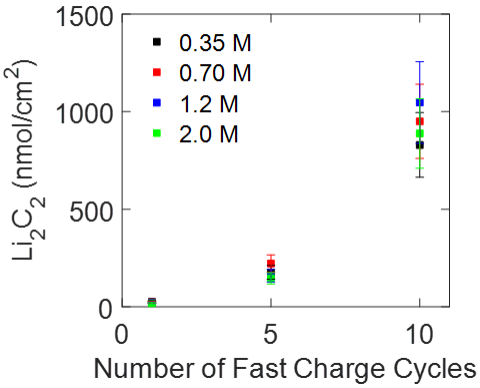

Figure 4.9: Li_2C_2 measured via MST as a function of fast charge cycle number on electrodes extracted from the coin cells corresponding to Figure 4.5 for electrolytes of 0.35 M $LiPF_6$, 0.70 M $LiPF_6$, 1.2 M $LiPF_6$, and 2.0 M $LiPF_6$ in 3:7w EC:EMC. Measurement error of $\pm 20\%$ arising from integration and calibration of the C_2H_2 evolution signature upon titration is shown.

4.8.3 Lithium Fluoride Detection via ^{19}F-NMR

Nuclear Magnetic Resonance Spectroscopy (NMR) was used in an attempt to quantify LiF on extracted electrodes. Due to a few issues discussed herein, we are not confident of the quantitative nature of our NMR results. Nevertheless, we present our attempt in doing so in hope that others may continue to refine the method to improve accuracy and sensitivity. The following procedure was used in order to prepare NMR samples:

1. The cycled graphite electrode was extracted from the decrimped coin cell and place in a vial for rinsing.
2. 1 mL of dimethyl sulfoxide (DMSO) was used to rinse the electrode three times, each time discarding the rinse solution.
3. 1 mL of DMC was used to rinse the electrode, and the rinse solution was discarded.
4. The electrode was dried for 15 minutes in the glovebox antechamber.
5. The electrode was soaked in 2 mL of D_2O. After at least 24 hours of soaking, 750 µL of the solution was sealed in NMR tubes for measurement.

The DMSO rinse (step 2) was designed to both remove electrolyte remaining in the pores of the graphite electrode and remove solid carbonates present in the SEI, which have been shown to be soluble in DMSO.[48] Somewhat surprisingly, we found that LiF is completely insoluble in rigorously anhydrous DMSO, as shown by the NMR spectrum for a control solution of LiF in DMSO-d_6 (see Figure 4.10), which lacked any ^{19}F peaks. We also visually observed that any added LiF would precipitate after allowing control solutions of LiF in DMSO-d_6 to rest for 1 day. This contradicts a previous report of modest solubility (~0.001 mole fraction)

of LiF in DMSO,[91] and we suspect this discrepancy arose due to water contamination in the DMSO of the previous study. The DMC rinse (step 3) was used to displace DMSO in the pores of the graphite with the more volatile DMC prior to vacuum drying.

D_2O was the only readily available deuterated solvent we found that was able to solvate LiF such that we could attempt to quantify F^- via ^{19}F-NMR. Admittedly, this is not the ideal choice of solvent, as any residual $LiPF_6$ could react with D_2O to form additional fluoride (see Reactions 4.4.1 and 4.4.2). The ^{19}F-NMR measurements revealed that three DMSO rinses removed most of the $LiPF_6$, but future iterations of this procedure should consider rinsing more than three times in DMSO to ensure the removal of all $LiPF_6$, particularly at high salt concentrations.

^{19}F NMR spectra were acquired on a Bruker Avance III 219 600 MHz instrument fitted with a 5 mm broadband Prodigy cryo-probe (BBO) and a variable temperature unit maintained at 25 °C. For each solution, pulse lengths were calibrated and T_1 relaxation time constants were measured using inversion recovery experiments. A calibration curve was made by performing ^{19}F NMR measurements on 9 solutions of known concentration of LiF in D_2O ranging from 3 µg/mL to 0.1 mg/mL. 256 scans were determined sufficient to achieve a signal to noise ratio of 200 at 3 µg/mL. For all LiF quantification measurements, ^{19}F spectra were acquired using a constant receiver gain, 256 scans, an acquisition time of 1 second and a recycle delay of at least $5T_1$. Phasing, baseline correction, and integration were performed in MestReNova and integrals were converted into concentration using the calibration curve as previously described.

We performed ^{19}F NMR measurements on graphite electrodes extracted from coin cells that had each undergone one C/10 constant current cycle with 0.010 and 1.5 V cutoff potentials with electrolytes of 0.35 M, 0.70 M, 1.2 M, and 2.0 M $LiPF_6$ concentration. We quantified 1600 nmol, 1950 nmol, 2200 nmol, and 2000 nmol LiF, respectively, on these extracted electrodes. These values are significantly larger than what would be expected given the amount of H_2 evolution typically observed in DEMS. We once again mention that some $LiPF_6$ remained in the D_2O soak solutions, so the measured amount of F^- may be artificially high for all electrolyte compositions due to the hydrolysis of remnant $LiPF_6$ in the D_2O soak solutions. We believe future iterations of this procedure could provide a reliable method of LiF quantification on graphite electrodes, but more thorough rinsing in DMSO prior to D_2O soaking will be necessary.

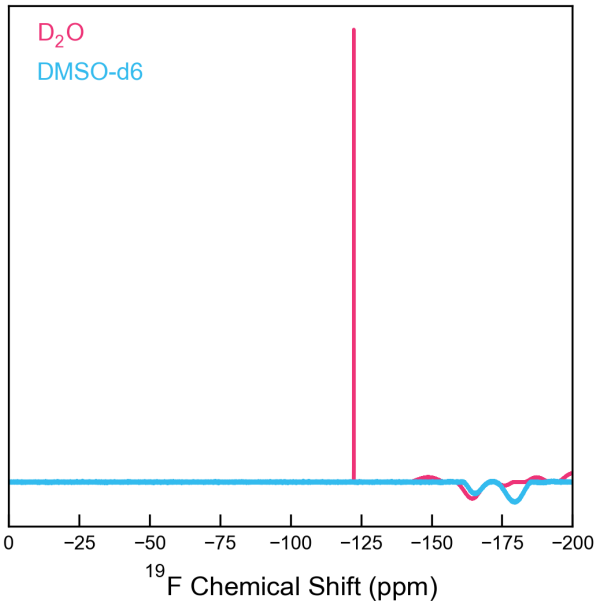

Figure 4.10: ^{19}F NMR sprectra for 0.1mg/mL LiF in D_2O (pink) and DMSO-d_6 (blue). No peaks can be distinguished in the DMSO-d6 spectrum, indicating the LiF is not soluble in DMSO within the sub 1 µg/mL detection limit of the spectrometer. Broad peaks in the -140 to -200 ppm range are due to fluoropolymer parts in the cryoprobe.

4.8.4 Electrochemical Modeling

A detailed description of the lithium plating sub-model within the graphite anode can be found Chapter 3, and key parameters are shown in Table 4.1. Based on MST and electrochemical signatures, the reversibility of lithium plating/stripping on graphite was found to be approximately 70%.[2] The lithium sub-model was added to the classic Newman model for a graphite half-cell, which has been summarized extensively in the literature. The solid-state diffusion coefficient for lithium in graphite was approximated using the formulation proposed by Yang et al., with diffusion slowing with intercalation.[92] Electrolyte properties were taken from previous Gen 2 electrolyte (1.2 M $LiPF_6$ in 3:7w EC:EMC) fits evaluated at 30 °C and can be found in Table 4.2.[31]

An initial attempt to model the different SEI properties of various electrolyte compositions was made by adding a simple film resistance (similar to reference [93]) and adjusting the nominal exchange current density for each based on the PEIS-measured charge transfer resistance. However, this did not improve model predictions compared to what is shown in Figure 4.4 for a global Butler-Volmer reaction with no film resistance. Often for electrode models with an SEI resistance, the SEI resistance can actually delay the model-predicted onset of lithium plating, which seems counterintuitive. Part of the challenge is understanding where lithium plates within the SEI: at the graphite/SEI interface, SEI/electrolyte interface, or throughout the entire film. Moving forward, the electric potential and chemical composition within the

SEI may need to be resolved to more accurately model lithium plating/stripping and capture effects of changing electrolyte composition.

Table 4.1: Electrochemical model parameter inputs for half-cell model. Concentrations for electrolyte C_e and intercalated lithium C_s are evaluated in kmol/m^3.

Property	Graphite Electrode	Separator	Lithium
Thickness (µm)	70	25	N/A
Porosity (%)	35.4	55	N/A
Particle Radius, r_p (µm)	4	N/A	N/A
Bruggeman Exponent	2.2	2.0	N/A
Exchange current density, i_0 (A/m^2)	$0.3(C_e)^{0.5}(C_s)^{0.5}(C_s - C_s^{max})^{0.5}$	N/A	100
Solid-state Diffusion Coefficient, D_s (m^2/s)	$3x10^{-14}(1.5 - C_s/C_s^{max})^{2.5}$	N/A	N/A
Maximum Intercalated Lithium Concentration, C_s^{max} (kmol/m^3)	28.0	N/A	N/A

Table 4.2: Electrolyte transport properties for Gen 2 electrolyte at 30 °C. Concentrations for electrolyte C_e are evaluated in kmol/m^3.

Electrolyte Property	Expression
Ionic conductivity, K (S/m)	$\frac{C_e}{10}(4.9464 - 1.8143C_e + 0.07968C_e^2 + 0.01947C_e^3)^2$
Diffusion Coefficient, D_s (m^2/s)	$0.0001\times10^{(-4.8321 - \frac{21.063}{T - 62.147 - 12.195C_e} - 0.3852C_e)}$
Transference Number, t_{Li+}^o	$-0.002395C_e^4 + 0.024476C_e^3 - 0.077134C_e^2 + 0.074373C_e + 0.43031$
Activity Coefficient, $1 + \frac{dlnf_{+-}}{dlnC_e}$	$0.5556 + 1.85997C_e - 0.4917C_e^2 + 1.0474C_e^3 - 0.1376\ C_e^4$

4.8.5 DEMS CO_2 Evolution

The CO_2 evolution measured with DEMS for the cells corresponding to Figures 4.2 and 4.3 are shown in Figure 4.11a-d. As discussed in Section 4.4.3, the CO_2 evolution which commences after about 5-10 hours likely coincides with the conversion of LiEDC to LiEMC. The total CO_2 evolved from DEMS (ignoring the CO_2 evolved during the initial rest period, which is likely related to hydrolysis of EC) for the 0.35 M, 0.70 M, 1.2 M, and 2.0 M electrolytes are 119, 90, 80, and 100 nmol, respectively, as shown in Figure 4.11e. If all of the CO_2 evolution is ascribed to LiEDC to LiEMC conversion, this brings us closer to accounting for all of the 'missing carbonates' discussed in Section 4.5.2. Combining the CO_2 evolved from MST with CO_2 evolved from DEMS, we find the adjusted ratio of CO_2 (DEMS + MST) to C_2H_4 (DEMS) falls in the range of 1.63-1.69 for all electrolyte compositions, as shown in Figure 4.11e. Still, the ratio of 2.0 expected for purely LiEDC formation is not reached. The remainder of the originally deposited solid carbonates from LiEDC are likely converted to other non-carbonate species such as lithium oxalate, as mentioned in Section 4.8.6.

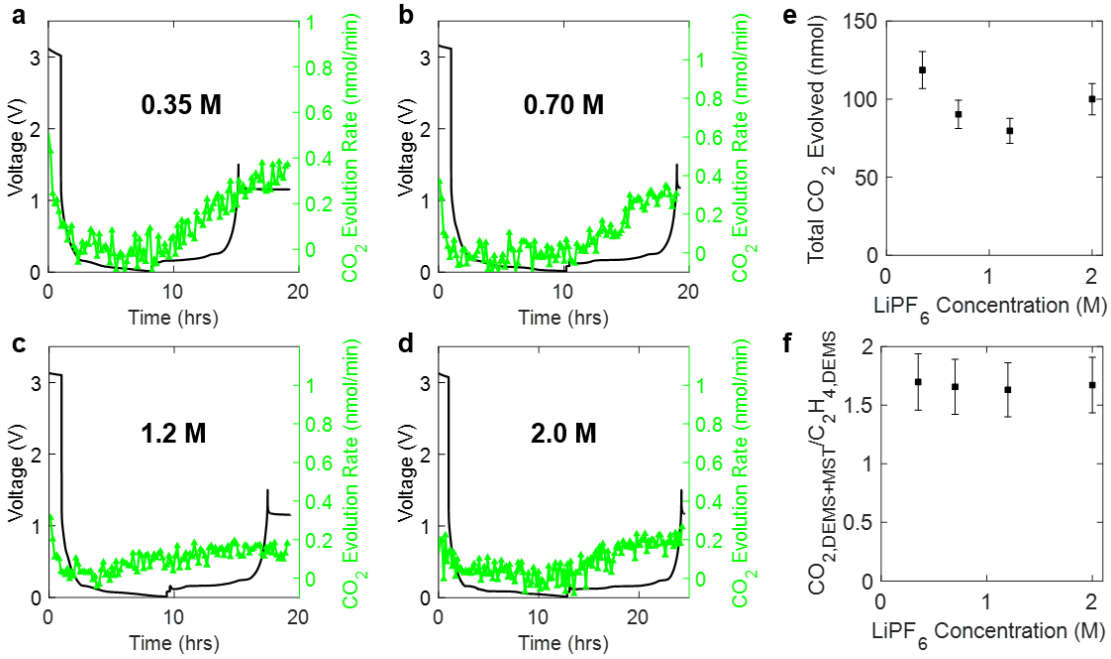

Figure 4.11: DEMS CO_2 evolution in Li-graphite half cells cycled at C/10 (corresponding to Figures 4.2 and 4.3) with **a.** 0.35 M $LiPF_6$, **b.** 0.70 M $LiPF_6$, **c.** 1.2 M $LiPF_6$, and **d.** 2.0 M $LiPF_6$ electrolytes. **e.** Total CO_2 evolved from DEMS excluding the CO_2 evolved during the initial rest period. Measurement error arising from integration of DEMS data is shown as ±10%. **f.** Ratio of CO_2 evolved from DEMS and MST combined to C_2H_4 evolved from DEMS, with error propagated from panel e.

4.8.6 Additional Possible Carbonate Consumption and Formation Reactions

Given the reported detection of oxalates, alkoxides, and other species in the graphite SEI literature along with the discussion of 'missing carbonates' in Section 4.5.2, possible mechanisms that consume solid carbonates and produce non-carbonates warrant discussion.[2;54;56;94] As mentioned in Section 4.8.2, some small fraction of LiEDC may undergo sequential reduction steps to form Li_2C_2 via an unknown mechanism. A more consistently reported constituent of the graphite SEI is lithium oxalate ($(COOLi)_2$), which likely forms via EC reduction as shown in Reaction 4.8.2.[94] Lithium oxalate is likely a substantial portion of the missing carbonates that cannot be accounted for by the conversion of LiEDC to LiEMC (which coincides with CO_2 in DEMS).

$$(CH_2OCO_2Li)_2\ (\text{LiEDC}) + 2\,Li^+ + 2\,e^- \longrightarrow (COOLi)_2 + (CH_2OLi)_2 \tag{4.8.2}$$

A somewhat nebulous source of solid carbonates is Li_2CO_3. It remains unclear whether Li_2CO_3 is formed via the reaction of existing solid carbonates (e.g., Reaction 4.4.14) or if it is formed via other mechanisms (e.g., Reaction 4.4.7). There are many conflicting

reports in the literature about the presence of Li_2CO_3 in the graphite SEI. Some report Li_2CO_3 as a minor SEI component in the inner-SEI,[3;85] while others report no Li_2CO_3 at all.[82;83;84] Perhaps the most probable pathway for the formation of Li_2CO_3 is via reaction of Li_2O with CO_2 (see Reaction 4.8.3), which may be present in the cell headspace from the reactions outlined in Section 4.4.3. This would explain the high variability in Li_2CO_3 detection among different researchers who may use cells with different headspace volumes or electrolytes that have been aged different amounts (which would affect the amount of CO_2 evolved as described in Section 4.8.1). A similar Li_2O-to-Li_2CO_3 mechanism occurs with nickel manganese cobalt oxide cathode materials, which form a surface Li_2CO_3 layer when exposed to a CO_2 atmosphere.[46]

$$Li_2O + CO_2 \longrightarrow Li_2CO_3 \tag{4.8.3}$$

4.8.7 Solid Carbonate Formation on Single Fast Charge Cycled Electrodes

The amount of solid carbonates measured via MST for electrodes extracted from coin cells that underwent a single fast charge cycle (corresponding to Figure 4.4) are shown in Figure 4.12a-d. We find that the amount of solid carbonates remains approximately constant within a single fast charge cycle to a given SOC for a given electrolyte composition, indicating that the relatively small amount of plated Li present after a single fast charge remains well encapsulated by the SEI and is not prone to react with electrolyte to form additional solid carbonates. The lone possible exceptions are the electrodes fast charged in 0.35 M and 0.70 M electrolytes to high SOC, which show a slight increase in the amount of solid carbonates above the baseline amount measured after formation cycling.

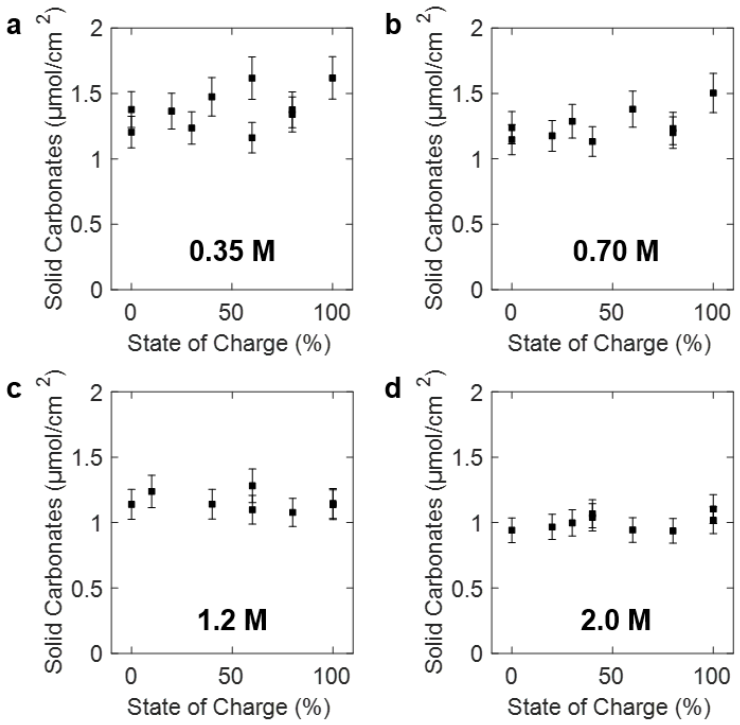

Figure 4.12: Solid carbonates quantified via MST for electrodes that underwent a single fast charge cycle to a given SOC (corresponding to Figure 4.4) for **a.** 0.35 M $LiPF_6$, **b.** 0.70 M $LiPF_6$, **c.** 1.2 M $LiPF_6$, and **d.** 2.0 M $LiPF_6$ electrolytes. Measurement error arising from integration of MST data is shown as ±10%.

4.8.8 Impedance Spectroscopy and Distribution of Relaxation Times

Potentiostatic electrochemical impedance spectroscopy (PEIS) was performed at OCV after charging in 10% graphite SOC increments using 3-electrode cells with a graphite working electrode, a NMC532 counter electrode, and a gold-lithium alloy wire reference electrode. The distribution of relaxation times (DRT) was used to isolate the graphite SEI and charge transfer resistances from the impedance data for each of the tested electrolyte compositions (0.35 M, 0.70 M, 1.2 M, and 2.0 M $LiPF_6$).

The 3-electrode cell was charged at C/10 to the specific graphite SOC, allowed to rest for 3 hours, and then PEIS was performed at open-circuit voltage. Each scan had a 5 mV amplitude and the frequency was swept from 100 kHz to 100 mHz. Following the methodology first laid out by Schichlein et al., the DRT is solved for this impedance data to extract out time constants of different processes contributing to the graphite impedance.[95] The DRT allows for the separation of processes with similar time constants, which otherwise cannot be resolved using traditional impedance analysis methods (e.g., equivalent circuit models). The resistances related to Li^+ movement through the graphite SEI and to the electron charge transfer reaction are readily extracted from the DRT spectra. Illig et al. have previously shown the utility of this analysis for deconvoluting processes on graphite

electrodes.[96]

The resultant SEI resistances for all electrolyte compositions are shown in Figure 4.13a. We note that the 2.0 M electrolyte had the lowest SEI resistance, owing to its thinnest solid carbonate layer. However, there is not a clear monotonic trend of decreasing SEI resistance with increasing salt concentration, as the 0.70 M electrolyte actually had the highest SEI resistance. This may be because the thicker inner-SEI layer for the 0.70 M electrolyte compared to the 0.35 M electrolyte caused the overall SEI resistance of the 0.70 M electrolyte to be slightly larger despite the reduced solid carbonate layer thickness compared to the 0.35 M electrolyte.

As shown in Figure 4.13b, the charge transfer resistances for each tested electrolyte composition are fairly uniform. However, the 0.35 M and 0.70 M electrolytes do exhibit larger charge transfer resistances at low states of charge than the higher concentration electrolytes. At high states of charge, a non-monotonic trend in R_{CT} with concentration is observed, with the lowest resistance at 1.2 M and the highest at 0.35 M.

We also note that there is a subtle discontinuity in the 0.70 M resistance data. The SEI resistance shows a step decrease at 70% SOC, and the charge transfer resistance shows a corresponding step increase at 70% SOC, shown in Figure 4.13c. The fitting procedure attributes some of the SEI resistance to the charge transfer process. This is not physically accurate but rather a mathematical artefact. Given that the data for the other three concentrations remains relatively constant, this discontinuity is likely caused by a fitting error wherein the time constants of the SEI and charge transfer processes are close enough to make deconvolution difficult. The approximately constant values for both the SEI and charge transfer resistances below 70% SOC are likely the more physically accurate resistance values.

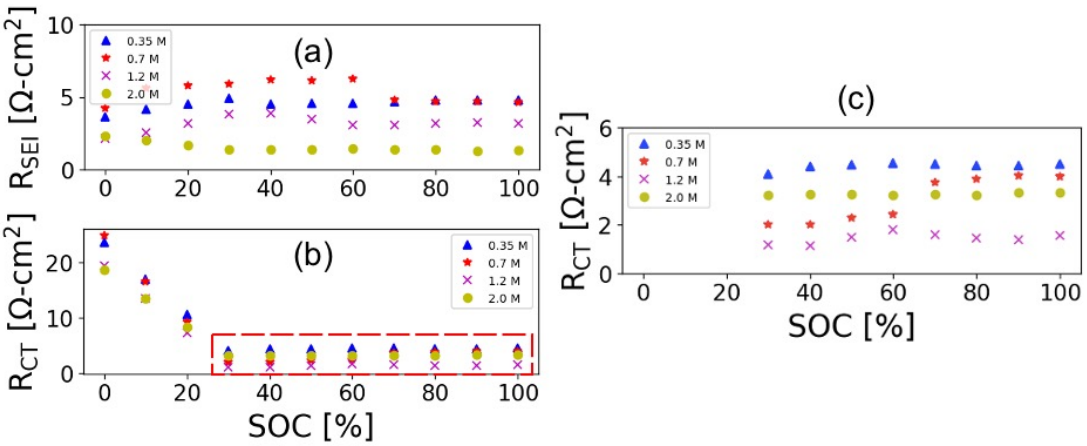

Figure 4.13: Extracted resistance values from PEIS data processed with the DRT from graphite-NMC-gold-lithium-alloy three electrode cells. **a.** Graphite SEI resistance (R_{SEI}) as a function of graphite SOC for each electrolyte composition. **b.** Graphite charge transfer resistance (R_{CT}) as a function of graphite SOC for each electrolyte composition. **c.** Graphite charge transfer resistance from panel b expanded in the high SOC, low R_{CT} region.

Chapter 5

Conclusion

This dissertation quantitatively explored how electrolyte transport properties and SEI composition shape the behavior of LIBs during fast charge.

In Chapter 2, we explored the inherent tradeoffs between t_+ and conductivity and, in doing so, uncovered the benefit of high t_+ electrolytes for fast charge and high energy density applications. The modeling work also provided useful targets for electrolyte properties required to avoid Li plating and to meet or exceed the charge performance offered by the traditional Gen 2 electrolyte.

In Chapter 3, we demonstrated a new, highly precise technique for quantitatively probing plated Li and SEI species, including solid carbonates and Li_2C_2, on graphite. We found that plated Li accounts for the majority of the capacity loss during fast charge, and some additional capacity is lost during extended cycling due to additional solid carbonate and Li_2C_2 formation. We also partnered with a modeling collaborator to extract useful quantities, including the Li plating exchange current density and Li stripping efficiency, by combining modeling and experimental data.

In Chapter 4, we added DEMS as an operando characterization method to complement the ex situ MST measurements. We studied the impact of electrolyte salt concentration on the formed graphite SEI and tied the SEI composition back to fast charge performance. This work once again employed the help of modeling collaborators, and we uncovered that, even with electrolyte transport properties fully specified as a function of concentration, discrepancy between model and experiment remained due to SEI impedance effects. The work uncovered the beneficial SEI properties imparted by high concentration electrolytes and revealed that new modeling frameworks with explicit SEI effects should be developed to accurately predict plating behavior.

Going forward, there are many mysteries still to solve in the fast charge and SEI space. Electrolyte additives such as vinylene carbonate and fluoroethylene carbonate impart remarkable

SEI stability, yet the mechanism of their decomposition to form an interfacial layer is still not well understood. Techniques outlined in this dissertation could be instrumental in determining the mechanisms by which these additives are reduced, and the insights should help inform future additive engineering.

As a final note: the mosaic SEI model proposed by Peled was well ahead of its time when it was introduced in 1997, and many of the key elements of the model have proven to be correct.[5] But, almost 25 years later, many questions still remain. What is very clear is that the SEI plays an integral role in determining the rate at which LIBs can be charged and discharged, and even the slightest instability of the SEI during cycling can ruin the dream of 99.999% coulombic efficiency that we strive for to enable so many LIB use cases. Targeted studies should be completed to quantify individual SEI species and pinpoint exactly how each SEI constituent is formed.

Bibliography

[1] K. Xu, *Chemical Reviews* **2014**, *114*, 23 11503.

[2] E. J. McShane, A. M. Colclasure, D. E. Brown, Z. M. Konz, K. Smith, B. D. McCloskey, *ACS Energy Letters* **2020**, *5*, 6 2045.

[3] P. Niehoff, S. Passerini, M. Winter, *Langmuir* **2013**, *29*, 19 5806.

[4] W. Huang, P. M. Attia, H. Wang, S. E. Renfrew, N. Jin, S. Das, Z. Zhang, D. T. Boyle, Y. Li, M. Z. Bazant, et al., *Nano Letters* **2019**, *19*, 8 5140.

[5] E. Peled, D. Golodnitsky, G. Ardel, *Journal of the Electrochemical Society* **1997**, *144*, 8 L208.

[6] K. M. Diederichsen, E. J. McShane, B. D. McCloskey, *ACS Energy Letters* **2017**, *2*, 11 2563.

[7] C. Uhlmann, J. Illig, M. Ender, R. Schuster, E. Ivers-Tiffée, *Journal of Power Sources* **2015**, *279* 428.

[8] Z. M. Konz, E. J. McShane, B. D. McCloskey, *ACS Energy Letters* **2020**, *5*, 6 1750.

[9] P. P. Paul, E. J. McShane, A. M. Colclasure, N. Balsara, D. E. Brown, C. Cao, B.-R. Chen, P. R. Chinnam, Y. Cui, E. J. Dufek, et al., *Advanced Energy Materials* **2021**, *11*, 17 2100372.

[10] M. Watanabe, M. Rikukawa, K. Sanui, N. Ogata, *Journal of Applied Physics* **1985**, *58*, 2 736.

[11] Y. Kato, S. Hori, T. Saito, K. Suzuki, M. Hirayama, A. Mitsui, M. Yonemura, H. Iba, R. Kanno, *Nature Energy* **2016**, *1*, 4 1.

[12] R. Bouchet, S. Maria, R. Meziane, A. Aboulaich, L. Lienafa, J.-P. Bonnet, T. N. Phan, D. Bertin, D. Gigmes, D. Devaux, et al., *Nature Materials* **2013**, *12*, 5 452.

[13] I. Villaluenga, S. Inceoglu, X. Jiang, X. C. Chen, M. Chintapalli, D. R. Wang, D. Devaux, N. P. Balsara, *Macromolecules* **2017**, *50*, 5 1998.

[14] K. M. Diederichsen, K. D. Fong, R. C. Terrell, K. A. Persson, B. D. McCloskey, *Macromolecules* **2018**, *51*, 21 8761.

[15] Z. Yu, L. A. Curtiss, R. E. Winans, Y. Zhang, T. Li, L. Cheng, *The Journal of Physical Chemistry Letters* **2020**, *11*, 4 1276.

[16] T. Abe, M. Ohtsuka, F. Sagane, Y. Iriyama, Z. Ogumi, *Journal of the Electrochemical Society* **2004**, *151*, 11 A1950.

[17] M. Doyle, T. F. Fuller, J. Newman, *Electrochimica Acta* **1994**, *39*, 13 2073.

[18] J. Newman, K. E. Thomas-Alyea, *Electrochemical Systems*, John Wiley & Sons, **2012**.

[19] M. Tang, P. Albertus, J. Newman, *Journal of the Electrochemical Society* **2009**, *156*, 5 A390.

[20] V. Srinivasan, J. Newman, *Journal of the Electrochemical Society* **2004**, *151*, 10 A1530.

[21] L. O. Valøen, J. N. Reimers, *Journal of the Electrochemical Society* **2005**, *152*, 5 A882.

[22] M. Thomas, P. Bruce, J. Goodenough, *Solid State Ionics* **1985**, *17*, 1 13.

[23] K. Persson, V. A. Sethuraman, L. J. Hardwick, Y. Hinuma, Y. S. Meng, A. Van Der Ven, V. Srinivasan, R. Kostecki, G. Ceder, *The Journal of Physical Chemistry Letters* **2010**, *1*, 8 1176.

[24] M. Park, X. Zhang, M. Chung, G. B. Less, A. M. Sastry, *Journal of Power Sources* **2010**, *195*, 24 7904.

[25] K. Kumaresan, G. Sikha, R. E. White, *Journal of the Electrochemical Society* **2007**, *155*, 2 A164.

[26] M. D. Levi, D. Aurbach, *Journal of Electroanalytical Chemistry* **1997**, *421*, 1-2 79.

[27] B. Suthar, P. W. Northrop, D. Rife, V. R. Subramanian, *Journal of the Electrochemical Society* **2015**, *162*, 9 A1708.

[28] S. Ahmed, I. Bloom, A. N. Jansen, T. Tanim, E. J. Dufek, A. Pesaran, A. Burnham, R. B. Carlson, F. Dias, K. Hardy, et al., *Journal of Power Sources* **2017**, *367* 250.

[29] Y. Liu, Y. Zhu, Y. Cui, *Nature Energy* **2019**, *4*, 7 540.

[30] A. M. Colclasure, A. R. Dunlop, S. E. Trask, B. J. Polzin, A. N. Jansen, K. Smith, *Journal of the Electrochemical Society* **2019**, *166*, 8 A1412.

[31] A. M. Colclasure, T. R. Tanim, A. N. Jansen, S. E. Trask, A. R. Dunlop, B. J. Polzin, I. Bloom, D. Robertson, L. Flores, M. Evans, et al., *Electrochimica Acta* **2020**, *337* 135854.

[32] C. Fang, J. Li, M. Zhang, Y. Zhang, F. Yang, J. Z. Lee, M.-H. Lee, J. Alvarado, M. A. Schroeder, Y. Yang, et al., *Nature* **2019**, *572*, 7770 511.

[33] Z. Shu, R. McMillan, J. Murray, *Journal of the Electrochemical Society* **1993**, *140*, 4 922.

[34] D. Lu, Y. Shao, T. Lozano, W. D. Bennett, G. L. Graff, B. Polzin, J. Zhang, M. H. Engelhard, N. T. Saenz, W. A. Henderson, et al., *Advanced Energy Materials* **2015**, *5*, 3 1400993.

[35] C. Shen, G. Hu, L.-Z. Cheong, S. Huang, J.-G. Zhang, D. Wang, *Small Methods* **2018**, *2*, 2 1700298.

[36] .

[37] V. Zinth, C. von Lüders, M. Hofmann, J. Hattendorff, I. Buchberger, S. Erhard, J. Rebelo-Kornmeier, A. Jossen, R. Gilles, *Journal of Power Sources* **2014**, *271* 152.

[38] L. Downie, L. Krause, J. Burns, L. Jensen, V. Chevrier, J. Dahn, *Journal of the Electrochemical Society* **2013**, *160*, 4 A588.

[39] M. Petzl, M. A. Danzer, *Journal of Power Sources* **2014**, *254* 80.

[40] T. Waldmann, B.-I. Hogg, M. Wohlfahrt-Mehrens, *Journal of Power Sources* **2018**, *384* 107.

[41] Q. Yuan, F. Zhao, W. Wang, Y. Zhao, Z. Liang, D. Yan, *Electrochimica Acta* **2015**, *178* 682.

[42] M. Petzl, M. Kasper, M. A. Danzer, *Journal of Power Sources* **2015**, *275* 799.

[43] J. Wandt, P. Jakes, J. Granwehr, R.-A. Eichel, H. A. Gasteiger, *Materials Today* **2018**, *21*, 3 231.

[44] B. D. McCloskey, A. Valery, A. C. Luntz, S. R. Gowda, G. M. Wallraff, J. M. Garcia, T. Mori, L. E. Krupp, *The Journal of Physical Chemistry Letters* **2013**, *4*, 17 2989.

[45] M. M. Ottakam Thotiyl, S. A. Freunberger, Z. Peng, P. G. Bruce, *Journal of the American Chemical Society* **2013**, *135*, 1 494.

[46] S. E. Renfrew, B. D. McCloskey, *Journal of the American Chemical Society* **2017**, *139*, 49 17853.

[47] M. Metzger, B. Strehle, S. Solchenbach, H. A. Gasteiger, *Journal of the Electrochemical Society* **2016**, *163*, 7 A1219.

[48] L. Wang, A. Menakath, F. Han, Y. Wang, P. Y. Zavalij, K. J. Gaskell, O. Borodin, D. Iuga, S. P. Brown, C. Wang, et al., *Nature Chemistry* **2019**, *11*, 9 789.

[49] R. Schmitz, R. A. Mueller, R. W. Schmitz, C. Schreiner, M. Kunze, A. Lex-Balducci, S. Passerini, M. Winter, *Journal of Power Sources* **2013**, *233* 110.

[50] M.-T. Fonseca Rodrigues, V. A. Maroni, D. J. Gosztola, K. P. Yao, K. Kalaga, I. A. Shkrob, D. P. Abraham, *ACS Applied Energy Materials* **2018**, *2*, 1 873.

[51] F. L. Usseglio-Viretta, A. Colclasure, A. N. Mistry, K. P. Y. Claver, F. Pouraghajan, D. P. Finegan, T. M. Heenan, D. Abraham, P. P. Mukherjee, D. Wheeler, et al., *Journal of the Electrochemical Society* **2018**, *165*, 14 A3403.

[52] D. Ren, K. Smith, D. Guo, X. Han, X. Feng, L. Lu, M. Ouyang, J. Li, *Journal of the Electrochemical Society* **2018**, *165*, 10 A2167.

[53] S. Bhattacharya, A. R. Riahi, A. T. Alpas, *Scripta Materialia* **2011**, *64*, 2 165.

[54] S. J. An, J. Li, C. Daniel, D. Mohanty, S. Nagpure, D. L. Wood III, *Carbon* **2016**, *105* 52.

[55] T. Liu, L. Lin, X. Bi, L. Tian, K. Yang, J. Liu, M. Li, Z. Chen, J. Lu, K. Amine, et al., *Nature Nanotechnology* **2019**, *14*, 1 50.

[56] A. Augustsson, M. Herstedt, J.-H. Guo, K. Edström, G. Zhuang, P. Ross Jr, J.-E. Rubensson, J. Nordgren, *Physical Chemistry Chemical Physics* **2004**, *6*, 16 4185.

[57] P. Arora, M. Doyle, R. E. White, *Journal of the Electrochemical Society* **1999**, *146*, 10 3543.

[58] T. R. Tanim, M. G. Shirk, R. L. Bewley, E. J. Dufek, B. Y. Liaw, *Journal of Power Sources* **2018**, *381* 56.

[59] N. Tian, C. Hua, Z. Wang, L. Chen, *Journal of Materials Chemistry A* **2015**, *3*, 27 14173.

[60] S. E. Renfrew, B. D. McCloskey, *ACS Applied Energy Materials* **2019**, *2*, 5 3762.

[61] D. P. Finegan, A. Quinn, D. S. Wragg, A. M. Colclasure, X. Lu, C. Tan, T. M. Heenan, R. Jervis, D. J. Brett, S. Das, et al., *Energy & Environmental Science* **2020**, *13*, 8 2570.

[62] H. K. Bergstrom, K. D. Fong, B. D. McCloskey, *Journal of the Electrochemical Society* **2021**.

[63] T. R. Tanim, E. J. Dufek, C. C. Dickerson, S. M. Wood, *Journal of the Electrochemical Society* **2019**, *166*, 12 A2689.

[64] U. R. Koleti, T. Q. Dinh, J. Marco, *Journal of Power Sources* **2020**, *451* 227798.

[65] S. Renfrew, Ph.D. thesis, UC Berkeley, **2019**.

[66] E. Logan, E. M. Tonita, K. Gering, J. Dahn, *Journal of Electrochemical Society* **2018**, *165*, 14 A3350.

[67] J. Landesfeind, J. Hattendorff, A. Ehrl, W. A. Wall, H. A. Gasteiger, *Journal of Electrochemical Society* **2016**, *163*, 7 A1373.

[68] B. D. McCloskey, D. S. Bethune, R. M. Shelby, G. Girishkumar, A. C. Luntz, *The Journal of Physical Chemistry Letters* **2011**, *2*, 10 1161.

[69] M. Stich, M. Gottlinger, M. Kurniawan, U. Schmidt, A. Bund, *The Journal of Physical Chemistry C* **2018**, *122*, 16 8836.

[70] K. Tasaki, K. Kanda, S. Nakamura, M. Ue, *Journal of the Electrochemical Society* **2003**, *150*, 12 A1628.

[71] V. R. Rikka, S. R. Sahu, A. Chatterjee, P. Satyam, R. Prakash, M. R. Rao, R. Gopalan, G. Sundararajan, *The Journal of Physical Chemistry C* **2018**, *122*, 50 28717.

[72] Y. Wang, S. Nakamura, M. Ue, P. B. Balbuena, *Journal of the American Chemical Society* **2001**, *123*, 47 11708.

[73] R. Bernhard, M. Metzger, H. A. Gasteiger, *Journal of the Electrochemical Society* **2015**, *162*, 10 A1984.

[74] P. G. Kitz, M. J. Lacey, P. Novák, E. J. Berg, *Journal of Power Sources* **2020**, *477* 228567.

[75] P. G. Kitz, P. Novák, E. J. Berg, *ACS Applied Materials & Interfaces* **2020**, *12*, 13 15934.

[76] D. Aurbach, Y. Gofer, M. Ben-Zion, P. Aped, *Journal of Electroanalytical Chemistry* **1992**, *339*, 1-2 451.

[77] G. V. Zhuang, K. Xu, H. Yang, T. R. Jow, P. N. Ross, *The Journal of Physical Chemistry B* **2005**, *109*, 37 17567.

[78] D. Aurbach, M. Daroux, P. Faguy, E. Yeager, *Journal of the Electrochemical Society* **1987**, *134*, 7 1611.

[79] L. Gireaud, S. Grugeon, S. Laruelle, S. Pilard, J.-M. Tarascon, *Journal of the Electrochemical Society* **2005**, *152*, 5 A850.

[80] K. Xu, G. V. Zhuang, J. L. Allen, U. Lee, S. S. Zhang, P. N. Ross Jr, T. R. Jow, *The Journal of Physical Chemistry B* **2006**, *110*, 15 7708.

[81] D. M. Seo, D. Chalasani, B. S. Parimalam, R. Kadam, M. Nie, B. L. Lucht, *ECS Electrochemistry Letters* **2014**, *3*, 9 A91.

[82] D. Aurbach, B. Markovsky, A. Rodkin, M. Cojocaru, E. Levi, H.-J. Kim, *Electrochimica Acta* **2002**, *47*, 12 1899.

[83] G. V. Zhuang, P. N. Ross Jr, *Electrochemical and Solid State Letters* **2003**, *6*, 7 A136.

[84] M. Nie, D. Chalasani, D. P. Abraham, Y. Chen, A. Bose, B. L. Lucht, *The Journal of Physical Chemistry C* **2013**, *117*, 3 1257.

[85] A. M. Andersson, A. Henningson, H. Siegbahn, U. Jansson, K. Edström, *Journal of Power Sources* **2003**, *119* 522.

[86] Y. Yu, P. Karayaylali, Y. Katayama, L. Giordano, M. Gauthier, F. Maglia, R. Jung, I. Lund, Y. Shao-Horn, *The Journal of Physical Chemistry C* **2018**, *122*, 48 27368.

[87] T. M. Østergaard, L. Giordano, I. E. Castelli, F. Maglia, B. K. Antonopoulos, Y. Shao-Horn, J. Rossmeisl, *The Journal of Physical Chemistry C* **2018**, *122*, 19 10442.

[88] N. Kumar, J. M. Seminario, *The Journal of Physical Chemistry C* **2016**, *120*, 30 16322.

[89] J. Zheng, J. A. Lochala, A. Kwok, Z. D. Deng, J. Xiao, *Advanced Science* **2017**, *4*, 8 1700032.

[90] X.-Q. Zhang, X.-B. Cheng, X. Chen, C. Yan, Q. Zhang, *Advanced Functional Materials* **2017**, *27*, 10 1605989.

[91] N. Xin, Y. Sun, M. He, C. J. Radke, J. M. Prausnitz, *Fluid Phase Equilibria* **2018**, *461* 1.

[92] X.-G. Yang, C.-Y. Wang, *Journal of Power Sources* **2018**, *402* 489.

[93] X.-G. Yang, Y. Leng, G. Zhang, S. Ge, C.-Y. Wang, *Journal of Power Sources* **2017**, *360* 28.

[94] L. Zhao, I. Watanabe, T. Doi, S. Okada, J.-i. Yamaki, *Journal of Power Sources* **2006**, *161*, 2 1275.

[95] H. Schichlein, A. C. Müller, M. Voigts, A. Krügel, E. Ivers-Tiffée, *Journal of Applied Electrochemistry* **2002**, *32*, 8 875.

[96] J. Illig, M. Ender, A. Weber, E. Ivers-Tiffée, *Journal of Power Sources* **2015**, *282* 335.